Controls on depositional processes on the Australian Northwest Shelf: the Oligocene to recent carbonate succession analyzed on 2D/3D seismic reflection and borehole data

Von der Fakultät für Georessourcen und Materialtechnik
der Rheinisch-Westfälischen Technischen Hochschule Aachen

zur Erlangung des akademischen Grades eines
Doktors der Naturwissenschaften

genehmigte Dissertation
vorgelegt von M.Sc.

Johannes Frederik Belde

aus Köln

Berichter: AOR PD Dr. rer. nat. Stefan Back
PD Dr. rer. nat. Gösta Hoffmann
AOR PD Dr. rer. nat. Sven Sindern

Tag der mündlichen Prüfung: 21. April 2017
Diese Dissertation ist auf den Internetseiten der Hochschulbibliothek online verfügbar

Contents

Executive Summary

The three individual studies presented in this thesis focus on the controls of depositional processes on the Australian Northwest Shelf (NWS), an ocean facing tropical carbonate ramp. Main study areas are the Browse and Northern Carnarvon Basins. The core of each analysis is an interpretation of 2D and/or 3D seismic-reflection data, supported - where available - by borehole data. A total of 47,577 km 2D and 15,400 km^2 3D seismic-reflection data in addition to over 50 industrial wells were available for analysis. The resulting seismic- and well-based interpretations are discussed against a background of sedimentological and oceanographic data of the respective study area, allowing comprehensive analyses of the controls on depositional processes and environmental changes over time.

In the Browse Basin, numerous carbonate platforms are preserved in the subsurface. New insights are provided by several 2D and 3D seismic-reflection surveys calibrated by well data into the lateral extent and morphology of successive platform and reef sequences, including the internal architecture and, where drilled, their lithology and age. The oldest carbonate build-ups imaged are of Oligocene age (34.03 – 27.8 Ma) and may be interpreted to represent either a reef-rimmed platform or a giant bryozoan reef-mound complex. No further build-ups can be observed between this period and the late Burdigalian, when continuous tropical reef growth in the area began. The various reef-rimmed carbonate platforms consecutively coalesced, forming an extensive barrier reef as the shelf-margin prograded further towards the north-west. In the period between the mid-Langhian to early Tortonian, an elongate (along-margin) barrier reef system formed in the Browse Basin, extending for over 500 km throughout the available data. This system most likely continued to the southwest extending across the Roebuck into the Northern Carnarvon Basin. Following the early Tortonian, reefs can be observed to form as less

connected, smaller build-ups on top or landward of the major middle Miocene barrier-reef system in the south of the study area, whereas reef fronts in the north during this time tend to be positioned further seaward. Around the Miocene-Pliocene boundary, most of the observed carbonate build-ups appear to have drowned.

The development of relatively stationary, thick aggrading platforms in the northern Browse Basin is interpreted as a reaction to high rates of subsidence, contrasted by the generally thinner reef-rimmed platforms observed in the southern Browse Basin where rates of subsidence are lower. As a consequence, eustatic changes in the south had a larger impact on the local carbonate platforms, forcing more frequent migration and resulting in thinner, more widespread platforms. The tropical reef-rimmed carbonate platforms of the late Burdigalian to early Tortonian nevertheless display, despite these general differences in lateral distribution and architecture, a remarkable resemblance along the approximately 500 km imaged on the available data. The observed termination of reef-growth in the study area occurring around 6 Ma coincides with and may be caused by the onset of current-driven drift sedimentation, possibly a consequence of changing oceanographic conditions through the tectonic closure of the SE Asian Gateway during the collision of northern Australia with the Banda Arc.

To further investigate the impact of the local current regime on the depositional environment of the NWS, the 3D geometry of sedimentary features recorded on the modern sea floor and the shallow subsurface of the northern Browse Basin were analysed on an extensive (>12,500 km^2) industrial 3D seismic-reflection survey. Large scale seismic-morphological features observed on the modern seafloor include submarine terrace escarpments, fault-scarps, incised channels and restricted areas of seismic distortion interpreted as mass wasting deposits. Extensive fields of sediment waves with heights of up to 10 m occur in water depths below 250 m, generally located at the foot of submerged terraces, along the scarps of modern faults and along the shelf break, while NW-SE-oriented furrows and ridges occupy the more planar regions of the outer shelf. Both types of bedforms require flow velocities between 0.3 and 1.5 m/s to form, which may be induced by oceanic currents, gravity currents or internal waves. For the region under study, the most likely source of bottom currents of this magnitude are internal waves, an interpretation that is reached through a discussion of oceanographic background data and modelling results. Besides the documentation of 3D seismic-geomorphological features on the mod-

ern sea floor, similar bedforms could also be mapped in the subsurface down to depths of 500 ms two-way-time, demonstrating the potential for the preservation of such bedforms in the sedimentary record and indicating a comparatively constant local current regime. Continuing the investigation of the influence exerted by the local current regime on the depositional environment, especially in respect to the impact of internal waves, the modern seafloor in the Northern Carnarvon Basin (imaged on 49,717 km^2 of 3D seismic-reflection data) was also analyzed for large scale sedimentary bedforms. The site was chosen to complement the previous study due to the availability of comprehensive geophysical, sedimentary and oceanographic data. In water depths between 55-130 m, where internal waves, tides and storms may induce currents on the seafloor, two fields of large scale sediment waves were observed. The first is located on a comparatively narrow section of shelf northwest of the Montebello Islands and most likely formed as a result of increased bottom currents induced by tidal flows diverted around the islands. The second is located within a local seafloor depression containing poorly sorted sediments, north of the Serruier and Bessieres Islands. The observed sediment waves could have either formed from the coarser sediment fraction that was reworked by cyclone-induced bottom currents into sand waves, or alternatively from the finer sediment fraction that was shaped by less energetic along-slope oriented currents into mudwaves within the topographic depression. The local carbonate sediments are partially composed of ooids and peloids, grains that formed in shallow water during the initial stages of the post glacial sea-level rise. Today these stranded grains are no longer in equilibrium with the depositional environment and the bedforms in which they are incorporated. The observation indicates that for fossil examples from comparable high-energy ramp systems, the possibility that grains and bedforms may be out of equilibrium should always be taken in account when interpreting the palaeo-depositional environment.

Zusammenfassung

Die drei dieser Dissertation zugrunde liegenden Studien widmen sich den Ablagerungsprozessen auf dem australischen Nordwestschelf, einer dem Indischen Ozean zugewandten tropischen Karbonatrampe. Die Hauptarbeitsgebiete sind das Browse- und das nördliche Carnarvon Becken. Der Kern jeder dieser Studien besteht dabei aus der Interpretation von 2D/3D reflektionsseismischen Datensätzen in Kombination mit Bohrlochdaten. Eine Datenbank aus insgesamt 47.577 km 2D und 15.400 km^2 3D Reflektionsseismik, ergänzt durch Daten von über 50 industriellen Bohrungen, stand hierfür zur Verfügung. Die erarbeiteten Interpretationen werden anschließend im Kontext von regionalen sedimentologischen und ozeanographischen Daten diskutiert, um die lokalen Ablagerungsprozesse und deren Entwicklung zu analysieren.

Im Untergrund des Browse Beckens sind zahlreiche Oligozäne bis subrezente Karbonatplattformen erhalten. Die Kombination mehrer, durch Bohrlochdaten kalibrierter 2D und 3D reflektionsseismischen Datensätze ermöglicht neue Einblicke in die laterale Ausdehnung und Morphologie der aufeinander folgenden Plattformen und Riffsequenzen, sowie deren interner Architektur und, wo erbohrt, deren Lithologie und Alter. Die ältesten abgebildeten Karbonatplattformen stammen aus dem Oligozän (34,03 – 27,8 Ma) und können entweder als Barriereriff-Systeme oder, alternativ, auch als ausgedehnte Bryozoen-Bioherme interpretiert werden. Keine weiteren Riffsysteme lassen sich erkennen, bis im Burdigalium ein kontinuierliches tropisches Riffwachstum in der Region einsetzte. Die verschiedenen riffumsäumten Karbonatplattformen verbanden sich zunehmend und formten ein kontinuierliches Barriereriff, während der Schelfrand sich weiter nordwestlich verlagerte. Zwischen dem mittleren Langhium und frühen Tortonium erstreckte sich im Browse Becken ein Barriereriff, welches sich innerhalb der verfügbaren Daten über 500 km verfolgen lässt und sich höchstwahrscheinlich weiter

südwestlich im Roebuck- und nördlichen Carnarvon Becken fortsetzt. Nach dem frühen Tortonium lässt sich im Süden des Arbeitsgebiets beobachten, wie sich oberhalb und landwärts des Barriereriffs kleinere, unzusammenhängende riffumsäumte Karbonatplattformen bildeten, wohingegen im Norden das Riffwachstum sich unverändert weiter seewärts verschob. Die meisten der beobachteten Karbonatplattformen scheinen um die Miozän-Pliozän Grenze ertrunken zu sein.

Die Entwicklung relativ stationärer, mächtiger aggradierender Karbonatplattformen im nördlichen Browse Becken wird als Reaktion auf hohe Subsidenzraten interpretiert, die vergleichsweise dünneren Karbonatplattformen im südlichen Browse Becken entsprechend als Reaktion auf geringere Subsidenzraten. Eustatische Meeresspiegelschwankungen hatten hier einen größeren Einfluss, wodurch die häufiger notwendige Migration die Entwicklung kleinerer und dünnerer Karbonatplattformen erzwang. Die tropischen riffumsäumten Karbonatplattformen des späten Burdigalium bis frühen Tortonium weisen trotz diesen Unterschieden in lateraler Verteilung und Architektur dennoch große Ähnlichkeiten entlang der im Datensatz abgebildeten 500 km auf. Das in der Studie beobachtete Ende des Riffwachstums um 6 Ma fällt mit dem Einsetzen von Drift-Sedimentation zusammen, möglicherweise als Konsequenz sich wandelnder ozeanischer Bedingungen, ausgelöst durch die tektonische Schließung der Verbindung zwischen dem Pazifischen und Indischen Ozean während der Kollision von Nordaustralien mit dem Bandabogen.

Um die Auswirkungen des lokalen Strömungsregimes auf das Ablagerungsmilieu weiter zu untersuchen, wurde die 3D Geometrie von sedimentären Strukturen auf dem modernen Meeresboden sowie im oberflächennahen Untergrund des nördlichen Browse Beckens anhand eines umfassenden (>12.500 km^2) industriellen 3D reflektionsseismischen Datensatzes analysiert. Seismisch-morphologische Großstrukturen auf dem modernen Meeresboden sind Terrassen, durch Störungen verursachte Geländestufen, in den Schelfrand eingeschnittene Rinnen sowie Regionen, die durch unregelmäßige Topographie, als Folge von Massenbewegungen gekennzeichnet sind. In Wassertiefen unterhalb von 250 m liegen großflächige Sedimentwellenfelder mit Scheitelhöhen von bis zu 10 m zumeist am Fuß der Terrassen, entlang der durch Störungen verursachten Geländestufen und entlang des Schelfrandes. Plane Flächen des äußeren Schelfs sind hingegen oft von NW-SO ausgerichteten Furchen und Kämmen gezeichnet. Beide

Arten von Sedimentstrukturen benötigen zur Entstehung Fließgeschwindigkeiten von ungefähr 0,3 bis 1,5 $\frac{m}{s}$, die durch Meeresströmungen, Dichteströme oder interne Wellen erzeugt werden könnten. Innerhalb des Arbeitsgebiets erscheinen interne Wellen als wahrscheinlichste Ursache für bodennahe Strömungen dieser Größenordnung, eine Interpretation, die aus ozeanischen Hintergrunddaten und Modellen abgeleitet wurde. Neben der Dokumentation von 3D seismisch-morphologischen Strukturen auf dem modernen Meersboden wurden vergleichbare Strukturen auch in Tiefen von bis zu 500 ms two-way-time darunter beobachtet, was gleichzeitig die Möglichkeit zur Erhaltung solcher Strukturen im Untergrund sowie ein vergleichsweise konstantes lokales Strömungsmilieu andeutet.

Um die Untersuchung der Auswirkungen des lokalen Strömungsregimes auf das Ablagerungsmilieu - vor allem in Hinsicht auf interne Wellen - fortzusetzen, wurden auch sedimentäre Großstrukturen auf dem modernen Meeresboden des nördlichen Carnarvon Beckens analysiert. Dieses Arbeitsgebiet erstreckt sich über 49.717 km^2 und ist durch umfassende geophysikalische (Seismik & Bohrungen), sedimentäre sowie ozeanographische Daten erfasst. In Tiefen von 55-130 m, in denen bodennahe Strömungen durch internen Wellen, Gezeiten und Stürme erzeugt werden können, liegen in diesem Arbeitsgebiet zwei Sedimentwellenfelder. Das erste Feld liegt in einem vergleichsweise schmalen Bereich des Schelfs, nordwestlich der Montebello-Inseln, wo es höchstwahrscheinlich aufgrund von durch die Inseln abgelenkten Gezeiten zu stärkeren bodennahen Strömungen kommt. Das zweite Feld liegt in einer flachen Vertiefung des Meeresbodens die schlecht sortierte Sedimente enthält und sich nördlich der Serruier und Bessieres Inseln befindet. Die dort beobachteten Sedimentwellen können entweder aus gröberem Sediment bestehen, geformt unter dem Einfluss eines Zyklons, oder alternativ aus feinerem Sediment innerhalb der Vertiefung, die hier eingebracht würden durch weniger energetische, entlang des Schelfs orientierte Strömungen. Die lokalen Karbonatpartikel setzen sich zum teil aus Ooiden und Peloiden zusammen, welche sich höchstwahrscheinlich während den Anfängen des post-glazialen Meeresspiegelanstiegs in flachem Wasser bildeten. Heute stehen diese reliktisch vorhandenen Partikel nicht mehr im Einklang mit dem Ablagerungsmilieu und somit auch nicht mit den Sedimentstrukturen, deren Bestandteil sie sind. Diese Möglichkeit, dass Sedimentstrukturen und ihre Bestandteile nicht im Gleichgewicht zueinander stehen, sollte bei der Inter-

pretation von Paläo-Ablagerungsmilieus in fossilen Beispielen von Karbonatrampen in vergleichbar hochenergetischen Strömungssystemen immer Beachtung finden.

Chapter 1

General Introduction

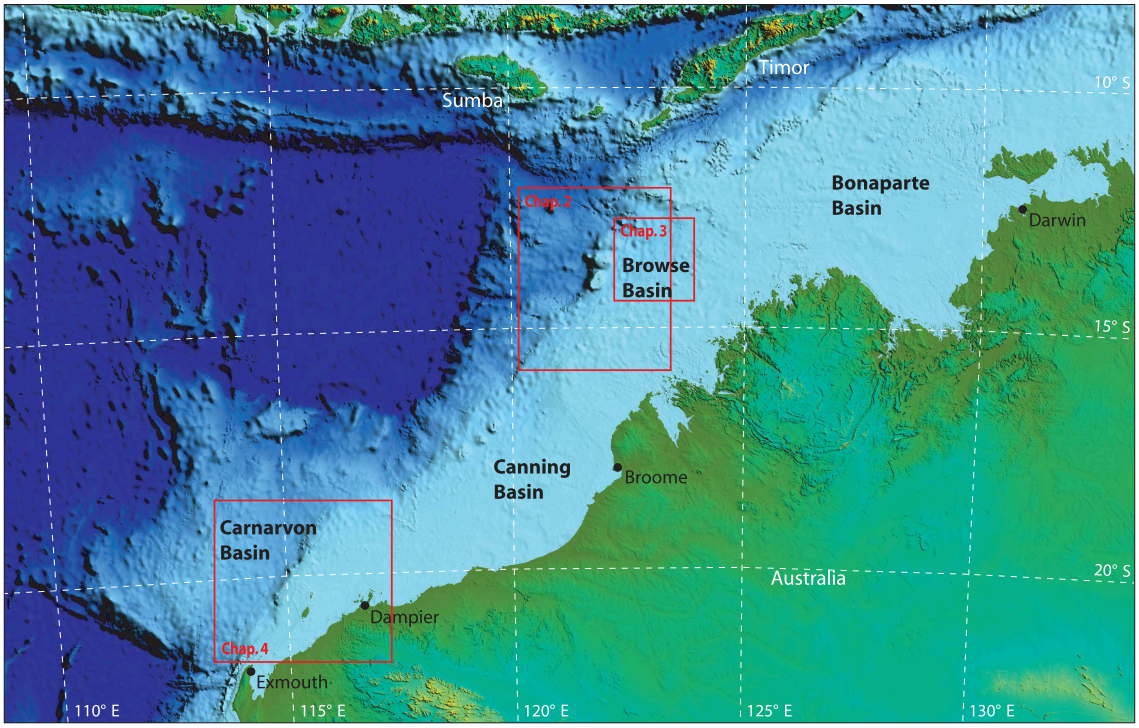

Figure 1.1: *Map of the Australian Northwest Shelf. The study areas of the three individual studies presented in this thesis are indicated by red boxes.*

The Australian Northwest Shelf (NWS) is an ocean facing tropical carbonate ramp which can be subdivided into the Bonaparte, Browse, offshore Canning and Carnarvon Basins (Fig. 1.1). The three individual studies presented in this thesis focus on the Browse and Northern Carnarvon Basins where, owed in large part to an avid interest by the hydro-

carbon industry in the basins, significant amounts of geophysical, sedimentological and oceanographic data were collected over the years. The approach of each study presented in this thesis began with the interpretation of 2D and/or 3D seismic reflection data, the results of which were then corroborated by incorporating sedimentological and oceanographic data of the respective study area. In this way, changes in the depositional environment of the NWS and analyses of the processes that control these changes are illustrated in the following chapters.

The study "Seismic Stratigraphy and Chronostratigraphy of Oligocene and Miocene reef-rimmed Carbonate Platforms in the Browse Basin, Australian Northwest Shelf" of chapter 2 focuses on the development of reef-rimmed carbonate platforms in the Browse Basin (Fig. 1.1) against a background of changing palaeo-environmental conditions. On the NWS buried Neogene reef-rimmed carbonate platforms have been previously mapped and analysed at several locations along the shelf between 20° and 11° S. In the very north-east, on the Ashmore Platform work was performed by Gorter et al. (2002) and Bernardel (2005), in the central Browse Basin by Power (2008), Bachtel et al. (2011) and Rosleff-Soerensen et al. (2012, 2016), in the Barcoo and Rowley sub-basins by Ryan et al. (2009) and Rosleff-Soerensen et al. (2016), and in the Northern Carnarvon Basin by Romine and Durrant (1996), Romine et al. (1997) and Cathro et al. (2003). These studies reveal an impressive belt of reef-rimmed carbonate platforms that has a combined length of over 1600 km, comparable in size to the modern Australian Great Barrier Reef (Ryan et al. 2009).
In this study, 2D and 3D seismic-reflection data complemented with age information from exploration wells was used to analyze carbonate platforms inside the Browse Basin, filling a gap between the Barcoo and Caswell sub-basins in the general interpretation of this reef belt. The focus lies on the documentation and interpretation of the main Miocene barrier-reef system and the establishment of similarities and differences in reef development with respect to the individual location. Through the considerable extent of this system responses to important palaeo-environmental and tectonic changes, such as the northward drift of the Australian plate during the Paleogene and Neogene (7-8 $\frac{cm}{a}$ at present day; Kreemer et al. 2000) and accompanying shifts in climate and ocean temperatures (Frakes et al. 1994; Frakes 1999; McGowran et al. 2004), can be discussed. Other regional and global factors controlling reef growth, migration and decay that are dis-

cussed include basin subsidence, eustasy and ocean currents, in addition to more local setting-specific controls such as antecedent topography and local tectonics. Changes in the depositional environment of the NWS visible in the data are also examined. These include the switch from chiefly non-tropical carbonate deposition during the Paleogene to conditions allowing the development of tropical, reef-rimmed carbonate platforms during the Neogene (Apthorpe 1988; Reuning et al. 2009; Rosleff-Soerensen et al. 2012) to the onset of current-driven drift sedimentation around 6 Ma, coinciding with the end of widespread reef development in the area.

In the study "Three-dimensional seismic analysis of sediment waves and related geomorphological features on a carbonate shelf exposed to large amplitude internal waves, Browse Basin region, Australia", presented in chapter 3, large scale sedimentary bedforms visible on the modern seafloor on top of the drift sediments were documented and analysed on 3D seismic reflection data of the Browse Basin (Fig. 1.1), as indicators characterizing the modern current regime in the area. Due to the high water depths involved, the effect of internal waves and tides on the local depositional environment was of particular interest. The role of internal waves in submarine sediment transport and accumulation has recently begun to receive increasing attention (Pomar et al. 2012; Shanmugam 2013a; Pomar et al. 2013). Internal waves are gravity waves that oscillate along the interface between two fluid layers of different density. Provided that the waters on a continental shelf or slope are well stratified, internal waves may be generated through the interaction of barotropic tides with the local bathymetry. The NWS is characterized by rapid bathymetric changes, a year-round stratification of the water column and strong tidal activity, a combination of factors that supports the generation of internal waves (e.g. Van Gastel et al. 2009). The occurrence of internal waves and tides on the NWS is well documented (e.g. Baines 1981; Holloway 1983a, 1984, 1987) and forms the basis of increasingly detailed computer models (e.g. Holloway 2001; Rayson et al. 2011, 2012). Field measurements in the direct vicinity of the study area also show the presence of internal solitary waves (solitons) with heights of up to 60 m (Wolanski and Deleersnijder 1998; Van der Boon 2011). Passing solitons may locally induce an intense increase in near-bottom current speeds, which in the past have proved disruptive to offshore activities such as oil and gas exploration and drilling (e.g. Kurup et al. 2011). Due to the ubiquity

and high amplitudes of internal waves in the region, the NWS is ideal for analysing and discussing the influence of internal waves on the development of large-scale sedimentary structures and sea-bed morphology.

In this study the modern seafloor and shallow subsurface imaged on an extensive (>12,500 km^2) seismic-reflection dataset of the northern Browse Basin were analysed. The observed geomorphological and sedimentological features were documented and compared with similar features along the NWS. These include marine terraces (Jones 1973), sediment waves (e.g. Jones 1971, 1973; James et al. 2004; Jones et al. 2009), furrows, mass-transport complexes and channels in a canyon head. This allowed a discussion of the relationship between the individual geomorphological features and the oceanographic environment. Since all sediment waves analysed in this study occurred in water depths greater than 250 m, the influence of surface waves is most likely negligible, shifting the focus of the interpretation in respect to their origin towards shelfal and deepwater bottom currents. A further aim of this study was to analyse the shallow sub-surface on the seismic-reflection data to evaluate the potential for preservation of such bedforms in the geological record.

The study "Sediment waves imaged on seismic reflection data from the high-energy carbonate ramp of the Northern Carnarvon Basin, North West Shelf Australia" presented in chapter 4 aimed to gain a broader perspective of the modern current regime and further insight into the role of internal waves and tides on the NWS. It followed the same approach as the previous study of chapter 3, using large scale bedforms visible on 3D seismic reflection data as indicators for local sediment mobilization. For submarine installations sediment movement on such a scale can be hazardous, potentially threatening the stability of underwater drilling platforms and moorings or increasing the risk of pipelines developing free-spans.

For this study the Northern Carnarvon Basin (Fig. 1.1) was chosen due to the comprehensive 3D seismic reflection, grain-size and oceanographic data available for analysis. Using this extensive data, the most likely mechanisms involved in the development of the sediment waves observed on the seismic-reflection data were discussed. 3D seismic-reflection data was favoured over for example multibeam sonar images in this study, as it has the great advantage of allowing the investigation of a much larger study area while

still providing sufficient resolution to image large-scale bedforms. Based on the observed bedform dimensions and crest orientations, in combination with local grain size distributions (Jenkins 2000), the current velocity and direction necessary for their development could be estimated (Stow et al. 2009). The water depths of the bedforms also help to further constrain which oceanic processes may potentially mobilize sediment at the respective site, allowing a correlation to local current measurements (e.g. James et al. 2004; Van Gastel et al. 2009; Van Gastel 2010) and computer models (e.g. Harris et al. 2000; Condie and Andrewartha 2008; Van Gastel et al. 2009; Van Gastel 2010). The results were compared to the interpretations of similar bedforms along the NWS and the northern Australian west coast by other authors (Jones 1973; James et al. 2004; Jones et al. 2009; Nichol and Brooke 2011; Belde et al. 2015).

A comprehensive summary of the conclusions reached on the different topics is given in chapter 5 and an outlook on further research possibilities in chapter 6. Peer-reviewed publications and conference contributions associated with the research presented in this thesis are listed below:

Manuscripts published in peer-reviewed journals:

Belde, J., S. Back, and L. Reuning (2015). Three-dimensional seismic analysis of sediment waves and related geomorphological features on a carbonate shelf exposed to large amplitude internal waves, Browse Basin region, Australia. Sedimentology 62, 87–109. doi: 10.1111/sed.12141.

Belde, J., L. Reuning, and S. Back (2017). Bottom currents and sediment waves on a shallow carbonate shelf, Northern Carnarvon Basin, Australia. Journal of Continental Shelf Research 138, 142-153. doi: 10.1016/j.csr.2017.03.007.

Belde, J., S. Back, J. Bourget, and L. Reuning (2017). Oligocene and Miocene Carbonate Platform Development in the Browse Basin, Australian Northwest Shelf. Journal of Sedimentary Research 87(8), 795-816. doi: 10.2110/jsr.2017.44.

Conference contributions:

Belde, J., S. Back, and L. Reuning (2013). 3D seismic geomorphology of sediment-wave fields and ridge-and-furrow systems on a carbonate shelf influenced by large amplitude internal waves. 30th IAS Meeting of Sedimentology, 2-5 September 2013, Manchester, UK.

Belde, J., S. Back, and L. Reuning (2013). Sediment-wave fields on a shelf influenced by large amplitude internal waves, Browse Basin region, Australia. Joint Meeting DMG, GV & Sediment, 16-19 September 2013, Tübingen, Germany.

Back, S., J. Engmann, K. Soika, J. Belde, F. Strozyk, and L. Reuning (2014). Detection, visualization and analysis of buried hiatal surfaces. SDGG 85, p. 187.

Belde, J., S. Back, and L. Reuning (2014). Neogene to recent reef development in the Barcoo and Caswell sub-basins, Browse Basin, Australian Northwest Shelf. SDGG 85, p. 36.

Reuning, L., J. Belde, and S. Back (2015). Seismic Geomorphology of the Pliocene to Recent Carbonate System of the Carnarvon Basin, Northwest-Shelf of Australia. 15th Bathurst Meeting, 13-16th July 2015, Bathurst, UK.

Ridder, M., S. Back, J. Belde, and L. Reuning (2015). 2D Seismic-Reflection Analysis and 3D Reconstruction of the Development of Cenozoic Carbonate Systems along the Lynher-Lombardina Structure, Browse Basin, Northwest Australia. GeoBerlin 2015, 4-7 October, Berlin, Germany.

Chapter 2

Seismic Stratigraphy and Chronostratigraphy of Oligocene and Miocene reef-rimmed Carbonate Platforms in the Browse Basin, Australian Northwest Shelf

The contents of this chapter are an early draft of the manuscript. A revised version was published in August 2017 with the title "Oligocene and Miocene Carbonate Platform Development in the Browse Basin, Australian Northwest Shelf" in the Journal of Sedimentary Research Volume 87(8), pages 795-816, by J. Belde[1], S. Back[1], J. Bourget[2] and L. Reuning[1].

[1]*EMR Geological Institute, RWTH Aachen University, Wüllnerstr. 2, 52062 Aachen, Germany*
[2]*Centre for Energy Geoscience, School of Earth and Environment, The University of Western Australia, 35 Stirling Highway, Crawley 6009 WA, Australia*

2.1 Abstract

Numerous carbonate platforms are preserved in the subsurface of the Browse Basin, Australian Northwest Shelf (NWS), as documented across multiple 2D and 3D reflection seismic datasets calibrated by wells. These data provide new insights on the lateral extent and morphology of successive platforms and reef sequences, their internal architecture and, where drilled, their lithology and age. The oldest carbonate build-ups can be interpreted either as a reef-rimmed platform or a giant bryozoan reef-mound complex of Oligocene age (34.03 - 27.8 Ma). Following this period no reef development could

be observed in the study area until the late Burdigalian, when continuous tropical reef growth began. The numerous reef-rimmed carbonate platforms progressively coalesced into an extensive barrier reef as the shelf margin prograded to the north-west. Between the mid-Langhian to early Tortonian, the Browse Basin contained an elongate (along-margin) barrier reef system, which can be mapped from northeast to southwest over approximately 500 km within the studied data. Further to the southwest, this barrier reef likely extended beyond the study area across the Roebuck Basin into the Northern Carnarvon Basin. After the early Tortonian, reefs developed on top or landward of this major middle Miocene barrier-reef system forming less connected, smaller carbonate build-ups in the south of the study area, while in the north reef fronts are generally positioned further seaward during this period. Most of the observed carbonate build-ups drowned around the Miocene-Pliocene boundary. High rates of subsidence in the northern Browse Basin are interpreted to have promoted the development of thick, aggrading platforms relatively fixed in place. The reef-rimmed platforms in the south, where subsidence rates were lower, are generally thinner. Carbonate systems there may have experienced eustatic changes more severely, forcing frequent system migration resulting in thinner, more widespread platforms. Beside these differences in lateral distribution and architecture of the tropical reef-rimmed carbonate platforms, the carbonate build-ups that formed between the late Burdigalian to early Tortonian nevertheless show a remarkable resemblance along the approximately 500 km of shelf under study. Reef development in the study area declined around 6 Ma, coinciding with and possibly as a consequence of current-driven drift sedimentation, which might be related to changing oceanographic conditions in the course of the tectonic closure of the SE Asian Gateway during the collision of northern Australia with the Banda Arc.

2.2 Introduction

Buried Neogene reef-rimmed carbonate platforms along the Australian Northwest Shelf (NWS) (Fig. 2.1) have been previously mapped and analysed across a wide region between 20° S and 11° S. In the very northeast, work on the Ashmore Platform was performed by Gorter et al. (2002) and Bernardel (2005), in the central Browse Basin by

Power (2008), Bachtel et al. (2011) and Rosleff-Soerensen et al. (2012, 2016), in the Barcoo and Rowley sub-basins by Ryan et al. (2009) and Rosleff-Soerensen et al. (2016), and in the Northern Carnarvon Basin by Romine and Durrant (1996), Romine et al. (1997) and Cathro et al. (2003) (Fig. 2.1). With a combined length of over 1600 km, this impressive belt of reef-rimmed carbonate platforms is similar in extent to the modern Australian Great Barrier Reef (Ryan et al. 2009).

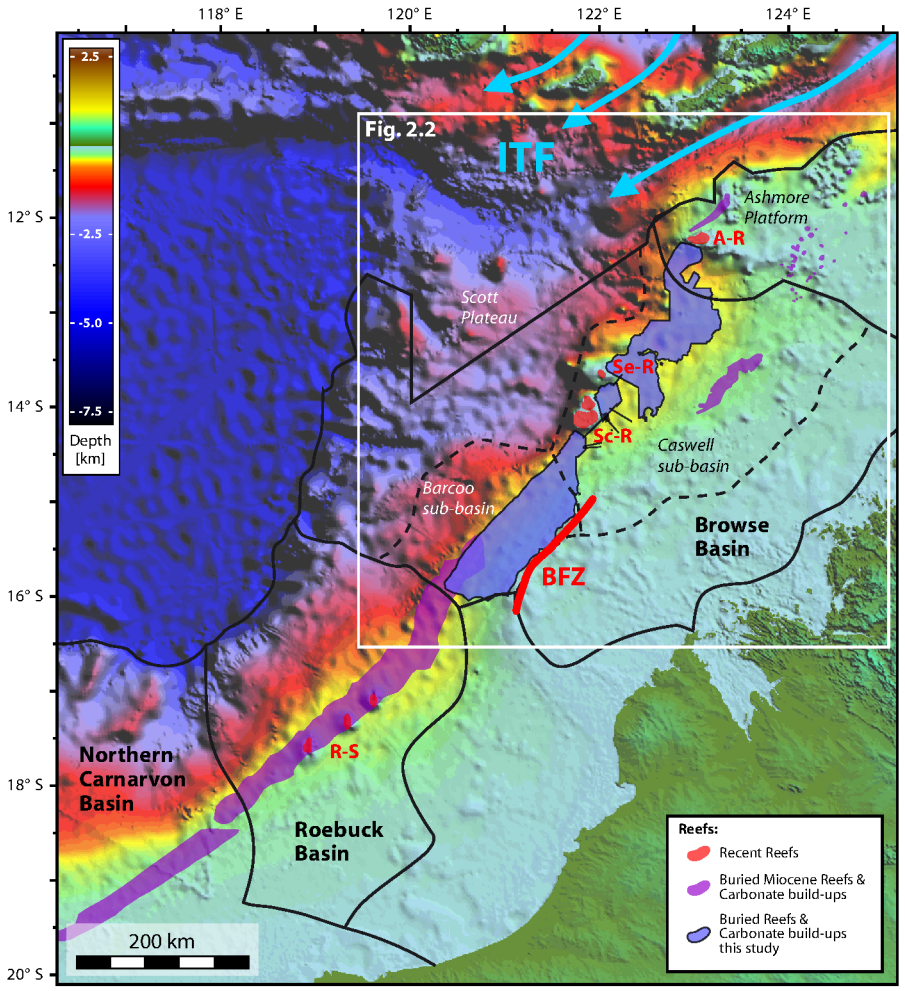

Figure 2.1: *Map of the study area on the Australian NWS based on a GEBCO one-minute-resolution bathymetry grid with superimposed locations of modern and palaeo-reefs. Modern reefs are indicated in red (A-R = Ashmore Reef, Se-R = Seringapatam Reef, Sc-R = Scott Reef, R-S = Rowley Shoals), a cumulative plot of the palaeo-reefs mapped in this study in blue and previously documented palaeo-reefs by other authors (Romine and Durrant 1996; Romine et al. 1997; Gorter et al. 2002; Cathro et al. 2003; Bernardel 2005; Power 2008; Ryan et al. 2009; Bachtel et al. 2011; Rosleff-Soerensen et al. 2012, 2016) in purple. The Indonesian Throughflow (ITF) is indicated by light blue arrows (after Gordon 2005). The Barcoo Fault Zone (BFZ) is indicated by a bold red line. Basin boundaries after Ryan et al. (2009).*

In this study, carbonate platforms of the Browse Basin are analyzed on 2D and 3D seismic-reflection data complemented with age information from exploration wells. Most prominent reef development took place between approximately 15.1 to 9.83 Ma, as evidenced by a platform belt with a width of up to 80 km that can be traced for 500 km within the data. The considerable extent of this system enables an analysis of the dynamic reef development in a period marked by important palaeo-environmental and tectonic changes. For example, the northward drift of the Australian plate during the Paleogene and Neogene (7-8 $\frac{cm}{a}$ at present day; Kreemer et al. 2000) was accompanied by changes in climate and ocean temperatures (Frakes et al. 1994; Frakes 1999; McGowran et al. 2004). The sedimentary record of this period shows that Cenozoic sedimentation of the NWS changed from dominating non-tropical carbonate deposition during the Paleogene to the development of tropical, reef-rimmed carbonate platforms in the Neogene (Apthorpe 1988; Reuning et al. 2009; Rosleff-Soerensen et al. 2012). The tectonic setting of the North West Shelf changed considerably during the Miocene, as the northern margin of Australia collided with Papua New Guinea and the Banda Arc (Keep and Haig 2010; Hall 2011). This resulted in major fault reactivation in the northern Browse and Bonaparte basins (Harrowfield et al. 2003; Bourget et al. 2012; Saqab and Bourget 2015a). The approach of this study to analyse the development of carbonate platforms in the Browse Basin against a background of changing palaeo-environmental conditions is based on 1) the documentation, description and interpretation of the main Miocene barrier-reef system in detail on 2D and 3D seismic-reflection data, focusing on similarities and differences in reef development with respect to the individual location; 2) the interpretation of the development of reef-rimmed platforms through time, focusing on a delineation of time dependent controlling factors for reef development; and 3) the establishment of a robust chronostratigraphic framework based on Sr-isotope and biostratigraphic analyses of borehole data that enables a direct comparison of contemporaneous carbonate platform development across the entire Browse Basin.

The documentation and discussion of the similarities and differences of reef-rimmed carbonate platforms across the ca. 100,000 km^2 study area supports an estimation of the relative contribution of regional and global controls on reef growth, migration and decay, including basin subsidence, eustasy and ocean currents, as opposed to the influence of

more local, setting-specific controls such as antecedent topography or local tectonics. The results of the seismic and well-based subsurface analysis presented allow a discussion of the importance of these local controls versus the regional and global controlling parameters; as a side aspect, this study also closes gaps in the yet incomplete interpretation of buried carbonate platforms between the Barcoo and Caswell sub-basins of the southern Browse Basin.

2.3 Geological Setting

The Browse Basin is located on the northwestern margin of Australia (Fig. 2.1) occupying approximately 140,000 km^2 of the present-day continental shelf (AGSO Browse Basin Project Team 1997). The Browse Basin is a pond-like sedimentary depocentre bound to the west by the Scott Plateau and to the east by the Leveque Shelf and northern Canning Basin (Fig. 2.1; Struckmeyer et al. 1998). Its main depocentres are the Caswell and Barcoo sub-basins (Fig. 2.1) which are separated by a major structural zone, the north to north-east oriented Brecknock and Buffon trends, formed during a phase of inversion in the Late Triassic (Struckmeyer et al. 1998). The structural architecture of the Browse Basin originated in the Jurassic, associated with the breakup of Greater India from Western Australia (Veevers and Cotterill 1978; Müller et al. 1998). The final phases of rifting in the Middle Jurassic and Early Cretaceous generated SW-NE-oriented structural trends (Etheridge and O'Brien 1994; Struckmeyer et al. 1998). Accompanying the northward drift of the Australian plate, sedimentation on the NWS transitioned from siliciclastic to carbonate-dominated in the Cenozoic (Apthorpe 1988).

During the Eocene and the middle Oligocene, subsidence outpaced shelf progradation, leading to increased water depths in the central basin (Stephenson and Cadman 1994). Along the shelf-slope transition, a highly progradational succession of partially argillaceous carbonates was deposited, forming a major unrimmed non-tropical carbonate ramp (Apthorpe 1988; Reuning et al. 2009; Rosleff-Soerensen et al. 2012). In the middle Oligocene, sediment bypass and possibly erosion occurred locally as a result of a major decrease in sea level (Stephenson and Cadman 1994). From the late Oligocene onwards,

subsidence rates accelerated as a consequence of the collision between the Australian and Eurasian plates (Kennard et al. 2004). Rapid subsidence along the NWS since the late Miocene could alternatively also be related to dynamic topography, resulting from convective downwelling in the mantle (DiCaprio et al. 2010; Heine et al. 2010; Czarnota et al. 2013).

Since the Miocene, the continental shelf was generally under open marine conditions, with the exception of a prominent exposure event in the middle Miocene (Rosleff-Soerensen et al. 2012) and short exposure times during glacial maxima in the Pleistocene (Stephenson and Cadman 1994). By the early middle Miocene, an extensive tropical reef-rimmed carbonate platform had developed in the Browse Basin (Rosleff-Soerensen et al. 2012), forming part of a nearly unbroken reef belt extending along the Miocene continental shelf margin of north-western Australia (Ryan et al. 2009). Most of the present day reefs of the Browse Basin and adjacent areas (Rowley Shoals, Scott Reef, Seringapatam Reef, Ashmore Reef) grew on this extensive foundation of palaeo-reefs and carbonate build-ups (Ryan et al. 2009). Much of the present-day structural architecture of the Browse Basin results from the Miocene to recent tectonic evolution of the region, dominated by the collision of the Australian Plate with the Banda Arc (Keep and Haig 2010; Bourget et al. 2012, 2014; Saqab and Bourget 2015b). Plate migration is still active and modern convergence rates are estimated to be 7-8 $\frac{cm}{a}$ (Kreemer et al. 2000). Neotectonic elements of the Browse Basin are primarily E-W to NE-SW trending faults of Miocene to Recent age, which are interpreted to have developed mainly through the reactivation of basement structures by forebulge flexure mechanisms (Keep et al. 2007; Keep and Harrowfield 2008; Langhi et al. 2011; Saqab and Bourget 2015b).

In the Barcoo sub-basin of the southern Browse Basin (Fig. 2.1), local strike-slip kinematics as a far-field consequence of the Australia-Banda Arc collision have been interpreted as the main cause for late Neogene structural inversion and faulting (Keep et al. 2007; Rosleff-Soerensen et al. 2016). The Barcoo Fault Zone (Fig. 2.1) is a broad strike-slip zone, approximately 180 km long and 2-20 km wide with an NE-SW orientation, located along the eastern boundary of the Barcoo sub-basin. The fault zone displays highly variable deformation styles along its length, probably due to the formation of restraining and releasing bends in a dextral strike-slip tectonic regime (Keep et al. 2000). All of the south-

ern carbonate platforms presented in this study are located immediately northwest of the Barcoo Fault Zone.

The large-scale tectonic development of SE Asia must be further regarded as an important factor influencing carbonate platform development by potentially affecting the palaeo-oceanographic circulation on the Australian NWS. The SE Asian Gateway, which connects the Pacific and Indian oceans, has considerably narrowed due to the northward moving Australian plate and the development of SE Asian volcanic arcs (Cane and Molnar 2001; Hall 2009), ultimately reducing the Indonesian Throughflow to its current throughput between 2.5 and 4 Ma (Gourlan et al. 2008). Driven by a steric height gradient, the Indonesian Throughflow transports warmer water towards the Australian NWS (CSIRO 2004; Kuhnt et al. 2004; Baker et al. 2008; Gallagher et al. 2009), where it contributes to the generation of the Leeuwin current (Vranes et al. 2002; Baker et al. 2008). The Leeuwin current flows in southern direction down the west coast of Australia in defiance of the dominant wind direction (Godfrey and Ridgway 1985), controlling the present-day reef distribution along this coast (Gallagher et al. 2014). With respect to Miocene reef development in the study area, a possible tectonically triggered late Miocene-Pliocene interruption of the Indonesian Throughflow (Kennett et al. 1985; Srinivasan and Sinha 1998; Moss et al. 2004; Gallagher et al. 2009) was previously interpreted as a potential contributing factor to the demise of the palaeo-reef systems in the Brecknock area (Rosleff-Soerensen et al. 2012; for location see Fig. 2.1).

2.4 Data

This study is based on a combination of 2D and 3D seismic-reflection surveys that provide an almost complete coverage of the Browse Basin between 11° to 16° S (Fig. 2.2). This area includes the Barcoo and Caswell sub-basins, the Ashmore Platform and parts of the Scott Plateau (Fig. 2.1). Initial seismic stratigraphic analyses (i.e. the mapping of seismic sequences, bounding surfaces and carbonate platform facies) were conducted primarily on 2D seismic-reflection data. 3D seismic-reflection data were subsequently incorporated to allow for more detailed investigations of the internal architecture of

carbonate-platform facies zones. The 2D seismic data mainly consists of the "Browse-98 Ashmore-Cartier 2D Speculative seismic survey" (hereafter referred to as BR98) that has a combined line length of almost 24,000 km. Additional 2D seismic coverage of the Barcoo sub-basin is provided by the "Plumhead" 2D survey (1,779 km line length). The 3D seismic-reflection data consists of the "North Browse TQ3D" seismic survey that covers over 12,000 km^2 of the central Browse Basin, the "Torosa 3D" survey (720 km^2) northeast of Scott Reef and the "Brecknock 3D" (845 km^2), "Brecknock South 3D" (285 km^2) and "Snarf 3D" (1,271 km^2) surveys southwest of Scott Reef. The Inline and Crossline spacings of the 3D surveys vary between 14.06-25 m and 12.5-14.06 m respectively. The "Firetail" 2D survey (931 km line length) was also included in this study to further improve the integration of the various 2D and 3D seismic surveys. Most of the seismic-reflection data used in this study are zero-phased in "European polarity", with a downward increase in acoustic impedance corresponding to a seismic trough. An exception is the Northern Browse 3D survey, which is zero-phased in SEG standard polarity or ("American polarity"), in which a downward increase in acoustic impedance corresponds to a seismic peak. In all figures, seismic amplitudes are uniformly displayed in blue when positive and orange when negative.

Geophysical logs of five wells (Barcoo-1, Brecknock-1, Maginnis-1, North Scott Reef-1, South Galapagos-1) provided ground-truthing (Fig. 2.3) of seismic data and subsurface lithology-predictions by wireline-log interpretation. Age information was provided by biostratigraphy data of sidewall-cores and ditch-cuttings documented in the well-completion reports, complemented by Sr-ages published by Rosleff-Soerensen et al. (2016) and newly measured samples. The biostratigraphy data is based almost entirely on samples taken from sidewall cores, with two exceptions (Nr. 17 in Barcoo-1 and Nr. 21 in North Scott Reef-1) and was converted into absolute ages using the Gradstein et al. (2012) timescale. In addition to the datums used by Rosleff-Soerensen et al. (2016, 2012) from the Barcoo-1 and Brecknock-1 wells, this study also incorporates data from the North Scott Reef-1 well (Table 2.1). The list was also expanded by the last occurrence of *Turborotalia cerroazulensis* documented in these three wells to extend the stratigraphic framework to the Rupelian. Additional age information was provided by four Sr-ages measured on sidewall cores from the Brecknock-1 well published by Rosleff-Soerensen et al. (2016),

supplemented by three new measurements (Nr. 18-20, Table 2.1). For these three bulk samples Sr-isotope composition was measured from sidewall cores by Thermal Ionization Mass Spectrometry (TIMS, TRITON, ThermoFisher Scientific) at the GEOMAR in Kiel (Germany). The internal precision of repeated analysis of the standard NIST SRM 987 was 5 ppm (2 SE). All $^{87}Sr/^{86}Sr$ were normalized to a value of 0.710248 for NIST SRM 987 and converted to absolute ages using the preliminary LOWESS Table 5 (pers. com. McArthur May 2015; McArthur et al. 2012). The uncertainty of the absolute age is less than $\pm$0.6 Ma in all cases using the calculation outlined in McArthur et al. (2012). Care was taken to avoid analysing non-carbonate material in the bulk sample, since potential siliciclastic contamination could result in elevated $^{87}Sr/^{86}Sr$ ratios and therefore an underestimation of the true age. Dissolving two aliquots of each sample with acids of different concentration resulted in $^{87}Sr/^{86}Sr$ values within an uncertainty of $\pm$0.6 Ma, indicating no significant contamination from the siliciclastic fraction. Nevertheless, based on the uncertainty inherent to bulk sample analysis we conservatively assigned an error estimate of $\pm$1.0 Ma to our Sr-ages. In both instances where biostratigraphic and Sr-age information are taken from the same sidewall core (Nr. 7 & 8, 17 & 18 in Brecknock-1; Table 2.1) the age-differences lie well within this margin.

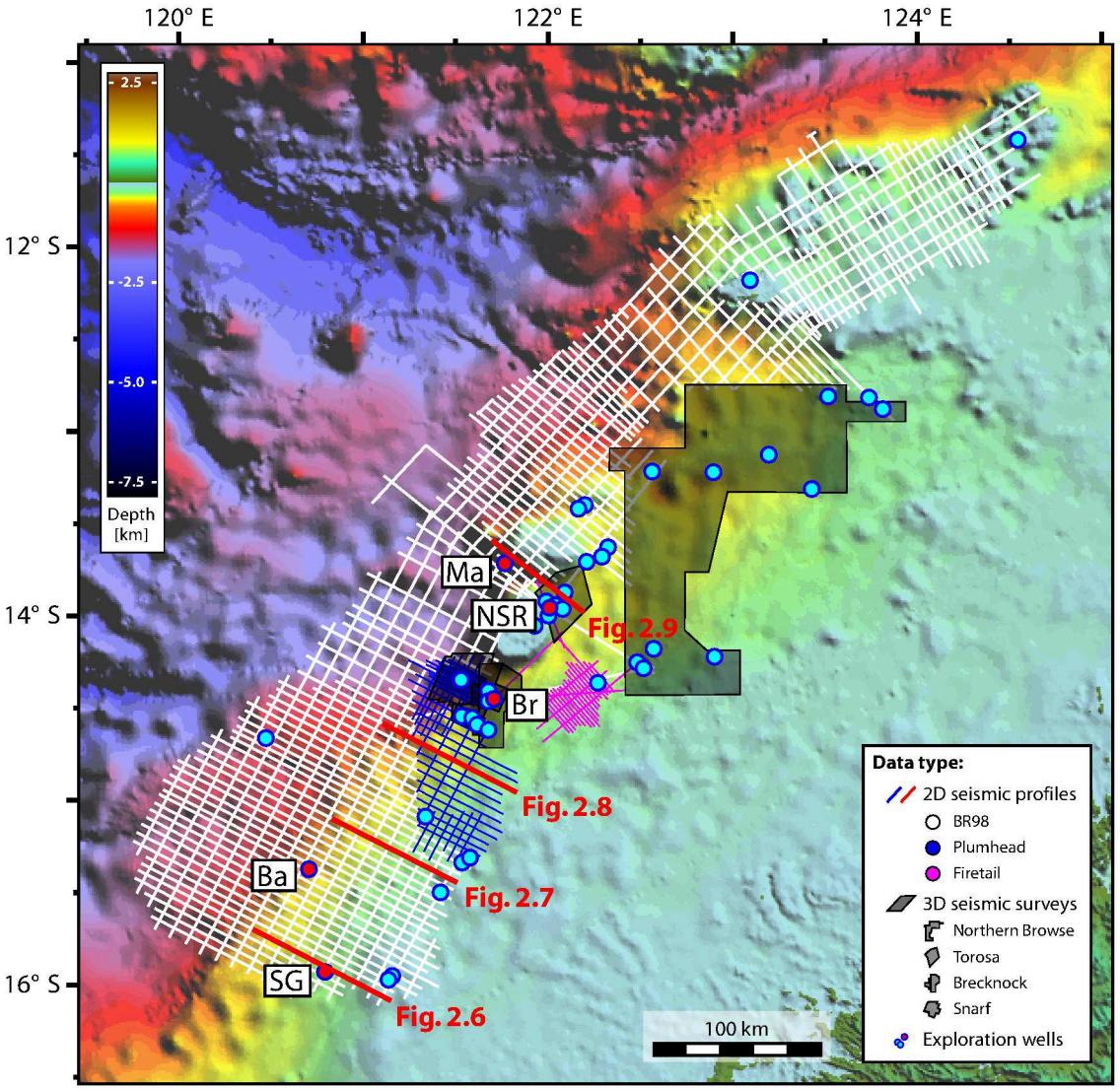

Figure 2.2: *Overview of the reflection seismic survey and well data used in this study plotted on a GEBCO one-minute-resolution bathymetry grid. The well sites of Barcoo-1 (Ba), Brecknock-1 (Br), Maginnis-1 (Ma), North Scott Reef-1 (NSR) and South Galapagos-1 (SG) are highlighted in red. The locations of the seismic sections BR98-005 (Fig. 2.6), BR98-021 (Fig. 2.7), BR98-034/P98-034 (Fig. 2.8) and BR98-096/Torosa (Fig. 2.9) are indicated by red lines.*

Table 2.1: Stratigraphic data for wells Barcoo-1, Brecknock-1 and North Scott Reef-1 (NSR-1). All samples were taken from sidewall cores with the exception of Nr. 17 in Barcoo-1 and Nr. 21 in NSR-1 which were taken from ditch cuttings. All datums are given in mbRT/mbKB. For stratigraphic events the datum has been averaged over the interval in which the event is present. For Nr. 11 both interval boundaries were plotted on the data (Fig. 2.9). FO: first occurrence, LO: last occurrence, X: change in coiling direction.

Nr.	Age datum / Stratigraphic event	Age [Ma]	Datum present [mbRT]						Comments / Error margins
			Barcoo-1		Brecknock-1		NSR-1		
1	X *Pulleniatina* sinis.-random.	4.08					802.5	± 12.5	
2	LO *Globoturborotalita nephentes*	4.37			937.0	min. age	867.5	± 7.5	*Globigerina nephentes*
3	FO *Globorotalia tumida*	5.57					912.5	± 7.5	Astronomically tuned from South Atlantic ODP sites 925 & 926
4	LO *Globorotalia lenguaensis*	6.14					942.5	± 7.5	Pacific calibration
5	FO *Pulleniatina primalis*	6.60					957.5	± 7.5	
6	Sr-age	9.6			1150.0				Age uncertainty ±1 Ma
7	Sr-age	10.3			1194.0				Age uncertainty ±1 Ma
8	FO *Neogloboquadrina acostaensis*	9.83			1234.5				*Globigerina acostaensis*, South Atlantic calibration
reference horizon H5									
9	Sr-age	11.1			1275.0				Age uncertainty ±1 Ma
10	Sr-age	11.8			1338.0	± 2.5			Age uncertainty ±1 Ma
11	*Flosculinella bontangensis*	14.24-15.1					1600-1960		Upper part of M6; LF8 according to Leg 194; in conflict with *Amphistegina bikiniensis* reported from the same depth interval but attributed to M1/O7 equivalent in Leg 194
12	LO *Praeorbulina sicana*	14.53	1450.0	± 10.0					*Globigerinoides sicanus*
reference horizon H4									
13	FO *Orbulina suturalis*	15.10	1687.5	± 17.5					
reference horizon H3									
14	FO *Praeorbulina sicana*	16.38	2222.5	± 2.5					*Globigerinoides sicanus*
15	*Lepidocyclina (Eulepidina) badjirraensis*	17.54			1909.5	± 9.5	2298.0	± 4.0	Brecknock-1: Chaproniere et al. (1996), core report assumed LO in the late Aquitanian; NSR-1: instead of late Aquitanian assumed in core report; equivalent to range in N6, uppermost part of M3
16	LO *Globoquadrina binaiensis*	19.09	2222.5	± 2.5					
reference horizon H2									Closely coincides with Nr.17
17	LO *'Paragloborotalia' kugleri*	21.12	2272.5	± 7.5	1949.0	± 30.0			*Globorotalia (Turborotalia) mendacis*
18	Sr-age	20.4			1979.0				Age uncertainty ±1 Ma
19	Sr-age	22.3			2033.0				Age uncertainty ±1 Ma
20	Sr-age	27.8			2200.0				Age uncertainty ±1 Ma
reference horizon H1									
21	LO *Turborotalia cerroazulensis*	34.03			2457.5	± 52.5	2710-2725		This is a minimum age since the interval above is nearly completely benthic

2.5 Seismic Interpretation

2.5.1 Horizon framework

The interval of interest for this study is the upper part of the Cenozoic sedimentary record. The interpretation of the Base Tertiary and Base Pliocene horizons in the south of the study area corresponds to the seismic and well interpretations of Rosleff-Soerensen et al. (2016). The Base Tertiary horizon defined in the northern study area is based on a correlation to biostratigraphic data from the Maginnis-1 well completion report (Fig. 2.2). In the Oligocene and Miocene part of the succession (Figs. 2.3 & 2.4), five reference horizons (H1-H5) were mapped on prominent positive seismic reflectors of high lateral continuity marked by stratal terminations above or below, or significant changes in seismic facies. The wells Barcoo-1, Brecknock-1 and North Scott Reef-1 were initially tied to the reflection seismic using velocity check-shot data. This time/depth-relationship was then further calibrated by synthetic seismograms (Fig. 2.3) calculated from the sonic- and density-logs of the respective wells using a seismic wavelet extracted from the reflection seismic data closest to the borehole over the relevant depth interval. For well North Scott Reef-1 no sonic and density data were available above 2300 mbRT, but a good correlation exists below this point. In the case of Brecknock-1 a constant density of 2.368 $\frac{g}{cm^3}$ was assumed between the seafloor and 2083 mbRT, an interval lacking density data. The seismic-well ties constrained the ages of the reference horizons (Table 2.1) to intervals between 34.03 and 27.8 Ma (H1), around 21.12 Ma (H2), between 16.38 and 15.1 Ma (H3), 15.1 and 14.53 Ma (H4) and 11.1 and 9.83 Ma (H5).

Due to a landward retreat of the shelf-slope transition south of Scott Reef (Fig. 2.1) the reflection continuity between the southern and northern study area is partly low and only horizons H4 and H5 could be unambiguously traced from well Brecknock-1 into the northern study area. To nevertheless allow a quantitative description of the seismic facies in the north and a comparison with the observations made in the south, three alternative horizons (a-c) were defined. Limited horizon continuity in the deeper part of the target interval was compensated by the integration of biostratigraphic age information from the well North Scott Reef-1 (Figs. 2.3 & 2.4, Table 2.1).

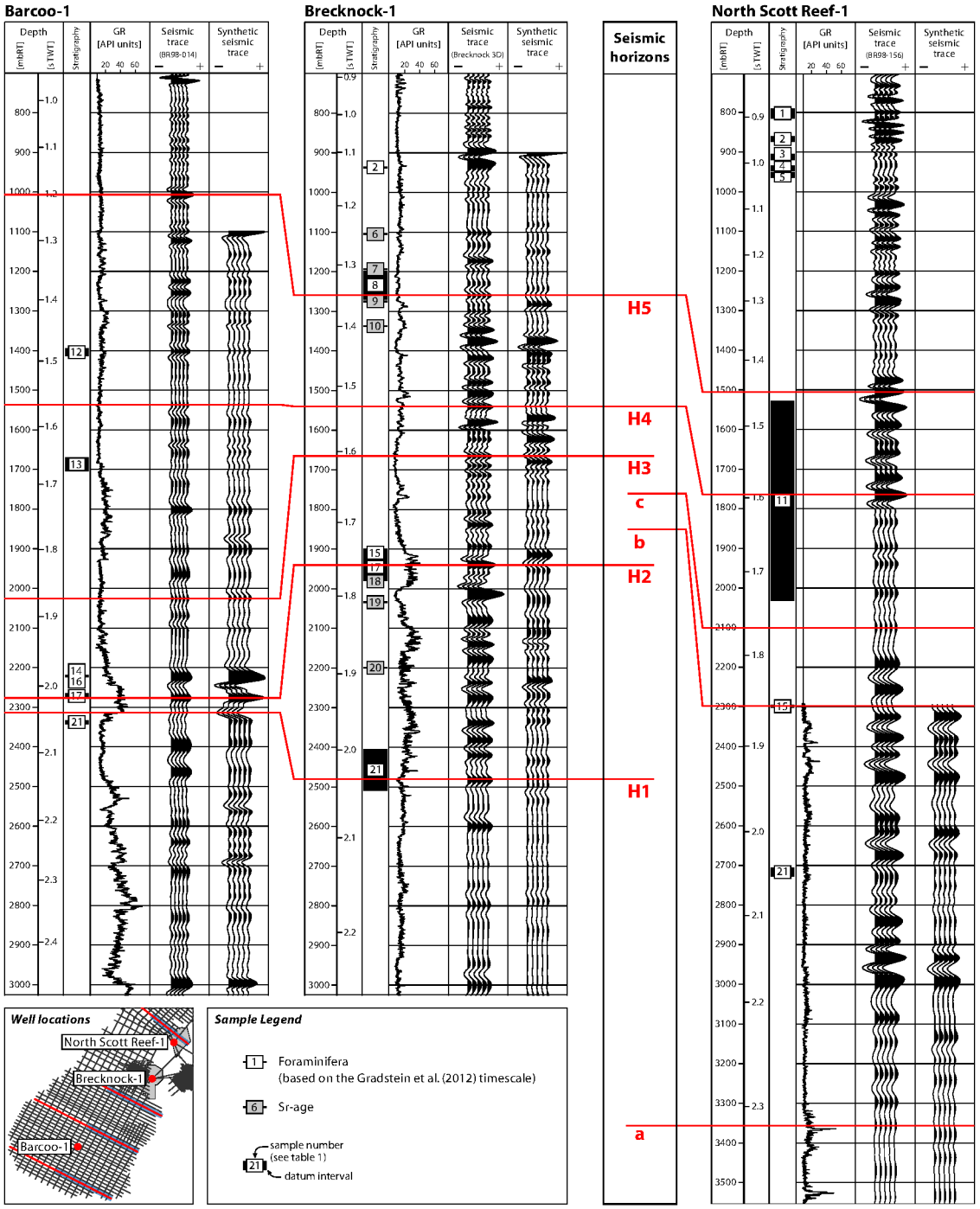

Figure 2.3: *Seismic to well tie and correlation panel for wells Barcoo-1, Brecknock-1 and North Scott Reef-1. The initial time/depth model based on vertical seismic profiles (VSP) was refined through a correlation with synthetic seismic profiles generated from sonic and density welllog data combined with a seismic wavelet extracted along the path of the respective borehole. For well North Scott Reef-1 no sonic and density logs were available above 2300 mbRT. Besides the reference horizons used in this study (solid red lines), the horizons defined by Rosleff-Soerensen et al. (2016) (dashed blue lines) are also shown for well Brecknock-1. For stratigraphic ages refer to figure 2.4 and table 2.1.*

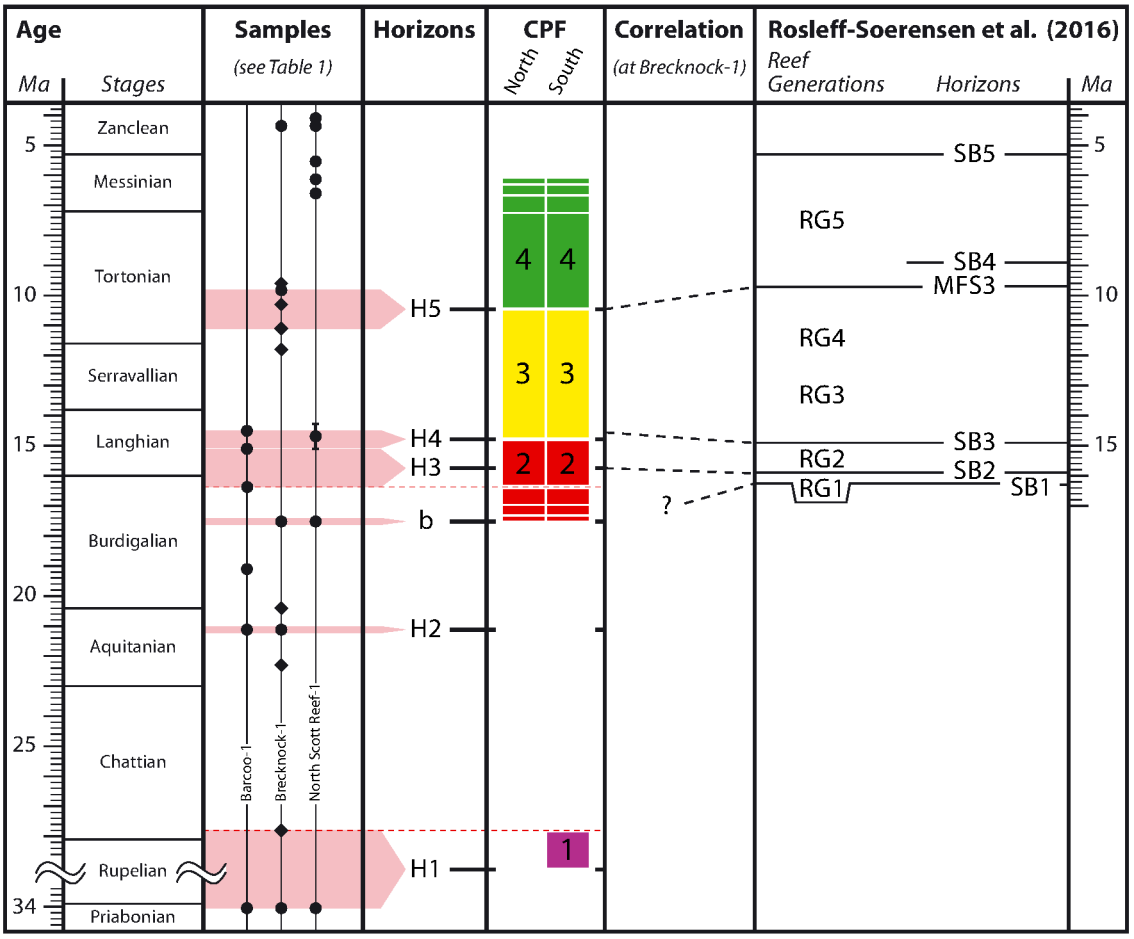

Figure 2.4: *Overview of the stratigraphic ages used in this study to constrain the interpreted reference horizons and carbonate platform facies intervals at the wells Barcoo-1, Brecknock-1 and North Scott Reef-1. Stratigraphic events are marked by dots and Sr-ages by diamonds. The panel on the right shows a correlation to the horizons and reef generations interpreted by Rosleff-Soerensen et al. (2016) in the Barcoo sub-basin.*

2.5.2 Seismic discontinuity zones

The 2D and 3D seismic-reflection data exhibit numerous zones of comparatively disrupted, medium- to high-amplitude reflections that stand out from the surrounding subparallel to parallel seismic-reflection packages (Fig. 2.5). At the seaward terminations of these seismic discontinuity zones velocity pull-ups are often visible, recording differences in acoustic impedance at the transition to the surrounding sediment. The observed seismic discontinuity zones extend over areas between a few tens and up to several hundreds of square kilometres in size, and are characterised in map view by circular or ellipsoidal shapes (Fig. 2.5A), extensive elongate discontinuity belts (Fig. 2.5B), or by complex inter-

nal associations of circular and ellipsoidal shapes and linear discontinuity features (Fig. 2.5C). In 3D vertical display and on 2D seismic-reflection data the discontinuity zones commonly show a bucket-shaped morphology flanked at the edges by steep foresets (Fig. 2.5A) and generally wavy tops (e.g. Fig. 2.5C). In the study area, the seismic discontinuity zones were drilled by well North Scott Reef-1. Well completion reports document cuttings and sidewall cores to show the presence of bioclastic and recrystallized limestones in wells Brecknock-1 and North Scott Reef-1 (Rosleff-Soerensen et al. 2012, 2016) and corals in well North Scott Reef-1. Seismic attribute data (Fig. 2.5) reveal isolated platforms (Fig. 2.5A) and barrier-reef geomorphologies (Fig. 2.5B, C). In the very south of the study area well South Galapagos-1 penetrated 3 seismic discontinuity zones (Fig. 2.6), but borehole sampling only commenced below, at depths greater than 1903 mbRT. In the following, all of the seismic facies interpreted to document carbonate platforms are stratigraphically grouped, with seismic carbonate-platform facies interpreted between the horizons "H1" and "H2" referenced as CPF-1, those between "H2" and "H4" as CPF-2, those between "H4" and "H5" as CPF-3 and those above "H5" as CPF-4. In respect to the study of Rosleff-Soerensen et al. (2016) CPF-2 corresponds to their reef generations RG1 and RG2, CPF-3 to their RG3 and RG4 and CPF-4 to their RG5.

The 2D and 3D seismic-reflection data exhibit numerous zones of comparatively disrupted, medium- to high-amplitude reflections that stand out from the surrounding subparallel to parallel seismic-reflection packages (Fig. 2.5). At the seaward terminations of these seismic discontinuity zones velocity pull-ups are often visible, recording differences in acoustic impedance at the transition to the surrounding sediment. The observed seismic discontinuity zones extend over areas between a few tens and up to several hundreds of square kilometres in size, and are characterised in map view by circular or ellipsoidal shapes (Fig. 2.5A), extensive elongate discontinuity belts (Fig. 2.5B), or by complex internal associations of circular and ellipsoidal shapes and linear discontinuity features (Fig. 2.5C). In 3D vertical display and on 2D seismic-reflection data the discontinuity zones commonly show a bucket-shaped morphology flanked at the edges by steep foresets (Fig. 2.5A) and generally wavy tops (e.g. Fig. 2.5C). In the study area, the seismic discontinuity zones were drilled by well North Scott Reef-1. Well completion reports document cuttings and sidewall cores to show the presence of bioclastic and recrystallized lime-

stones in wells Brecknock-1 and North Scott Reef-1 (Rosleff-Soerensen et al. 2012, 2016) and corals in well North Scott Reef-1. Seismic attribute data (Fig. 2.5) reveal isolated platforms (Fig. 2.5A) and barrier-reef geomorphologies (Fig. 2.5B, C). In the very south of the study area well South Galapagos-1 penetrated 3 seismic discontinuity zones (Fig. 6), but borehole sampling only commenced below, at depths greater than 1903 mbRT. In the following, all of the seismic facies interpreted to document carbonate platforms are stratigraphically grouped, with seismic carbonate-platform facies interpreted between the horizons "H1" and "H2" referenced as CPF-1, those between "H2" and "H4" as CPF-2, those between "H4" and "H5" as CPF-3 and those above "H5" as CPF-4. In respect to the study of Rosleff-Soerensen et al. (2016) CPF-2 corresponds to their reef generations RG1 and RG2, CPF-3 to their RG3 and RG4 and CPF-4 to their RG5.

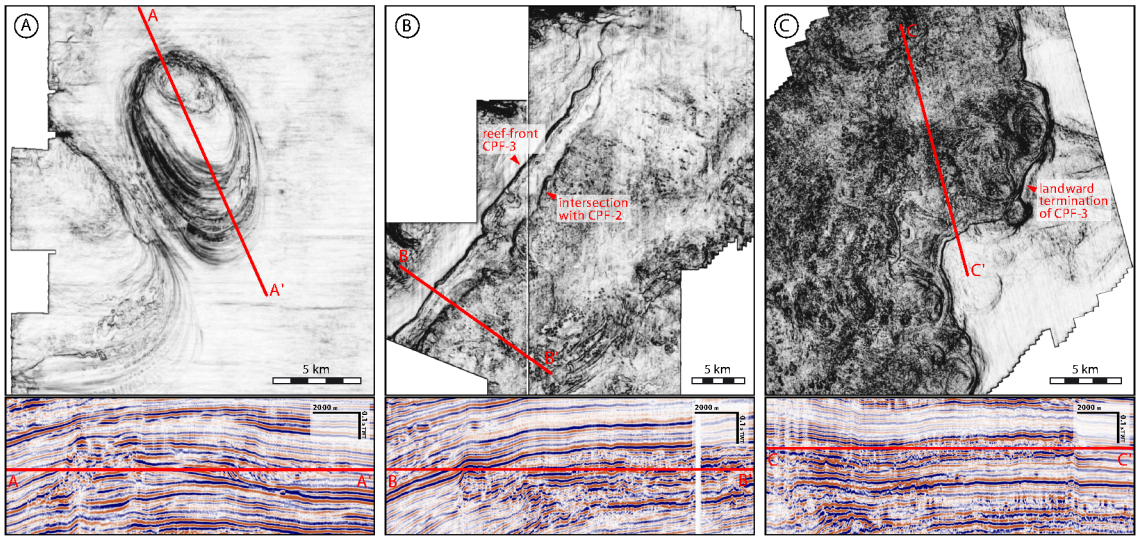

Figure 2.5: *Examples of carbonate platform facies mapped in this study are shown on variance timeslices and vertical reflectivity sections. (A) Isolated carbonate platform associated with CPF-4 in the Northern Browse 3D seismic survey. (B) Front of the barrier reef associated with CPF-3 in the Brecknock and Brecknock South 3D seismic surveys. (C) Landward termination of the barrier reef associated with CPF-3 in the Snarf 3D seismic survey. Internal reflection signatures on both, timeslice and vertical data suggest many smaller reef bodies that coalesced into a continuous barrier reef.*

2.5.3 Seismic interpretation

To illustrate the variability in carbonate platform development and distribution across 500 km of the Australian NWS, four representative dip seismic sections spaced between 63 and 120 km were used (Figs. 2.6-2.9). Three WNW-ESE oriented 2D seismic sections were chosen south and one NW-SE oriented 2D/3D composite seismic section north of the modern Scott Reef region (Fig. 2.2).

On all seismic sections, the interval between the Base Tertiary and horizon H1 (auxiliary horizon a on Fig. 2.9) is characterized on the landward side by subparallel, high amplitude and low frequency reflectors that increase basinwards in dip, grading into sigmoidal clinoforms of variable thickness with semi-continuous (Fig. 2.6), continuous (Figs. 2.7 & 2.8) or partly chaotic (Fig. 2.9) internal reflections. Reflection frequencies in the interval are lower on the landward side in comparison to those in the seaward parts. The interval has a maximum thickness of ca. 360 ms TWT.

Between horizons H1 and H2 (auxiliary horizons a and b on Fig. 2.9), sub-parallel to chaotic reflectors with variable amplitudes grade seawards into medium- (Figs. 2.6 & 2.7) to high-angle (Figs. 2.8 & 2.9), convex upward clinoforms with continuous (Figs. 2.6 & 2.7), semi-continuous (Fig. 2.8) or partly disrupted (Fig. 2.9) internal reflections of medium amplitude. From the southern (Fig. 2.6) up to the north-central (Fig. 2.8) part of the study area, a thin veneer ($\sim$ 100 ms TWT) of high amplitude facies CPF-1 occurs along the western flank of the Barcoo Fault Zone continuing northward as an up to 17 km wide belt of ca. 220 km length into the Brecknock area (Fig. 2.10A). Figures 2.6 to 2.8 show the occurrence of CPF-1 on the seaward slope of the Lynher-Lombardina anticline in the south of the study area. Further north in the Brecknock area (Fig. 2.10B to D) there is no indication of a distinct slope associated with the flat-based facies zone. At this location, CPF-1 is in places associated with seaward-dipping reflection foresets (Fig. 2.10C) and intercalated areas of high reflection continuity (Fig. 2.10D). CPF-1 is not observed in the north of the study area.

The interval between horizons H2 and H3 (auxiliary horizons b and c on Fig. 2.9) is characterized by a highly variable thickness (up to 580 ms TWT) and variable seismic reflector

configurations. In the southern (Fig. 2.6), south-central (Fig. 2.7) and north-central (Fig. 2.8) parts of the study area, basal high-continuity and high-amplitude seismic reflectors onlap onto horizon H2. Above, vast parts of the study area are characterized by CPF-2 extending margin parallel for ca. 360 km with a variable width of 14 to 80 km (Fig. 2.11A). 3D seismic imaging of the seismic carbonate platform facies documents an elongate seaward boundary for CPF-2 that can be interpreted as a barrier reef. On the landward side, this discontinuity zone is accompanied by various circular structures, several kilometres in diameter, which are interpreted as isolated reef-rimmed platforms (Fig. 2.11B). In the north of the study area (Fig. 2.9), the interval between auxiliary horizons b and c is characterised by parallel, continuous, high-amplitude reflectors that terminate in prograding clinoforms; the base of the massive, seismically partly discontinuous CPF-2 can be interpreted immediately below auxiliary horizon c (Fig. 2.9). Amplitudes are medium to high within CPF-2, and the reflector frequency is low.

Between horizons H3 (auxiliary horizon c on Fig. 2.9) and H4, subparallel to parallel reflectors of medium amplitudes characterize the landward part of the study area, grading seaward into the extensive seismic carbonate platform facies interpreted as the younger, seaward continuation of CPF-2 (Figs. 2.6-2.9, 2.11). The seismic amplitudes are generally medium to low, except for high amplitudes in the central seismic carbonate platform facies and clinoform topsets seaward of CPF-2. Seismic reflectors between horizons H4 and H5 are generally of medium amplitude and subparallel in the landward part of the study area, grading seaward into discontinuous reflectors of carbonate platform facies (CPF-3). On the basinward side of the section, CPF-3 is laterally interbedded with subparallel to parallel reflectors. The seaward boundary of CPF-3 coincides with an increase in reflector dip. Figure 2.12A depicts the lateral distribution of CPF-3, which is the most seaward of the studied reefs in the south of the study area, extending over at least 500 km in SE-NW direction. CPF-3 has the form of a barrier reef in the south with a width of 25-38 km that decreases to less than 18 km in the Torosa area, further north of which individual circular reef-rimmed carbonate platforms begin to appear. Figure 2.12B illustrates the 3D seismic signature of CPF-3 in the northern Browse region documenting an elongate reef barrier on the seaward side of the system, sheltering on its landward side a possible lagoonal area with numerous patch reefs.

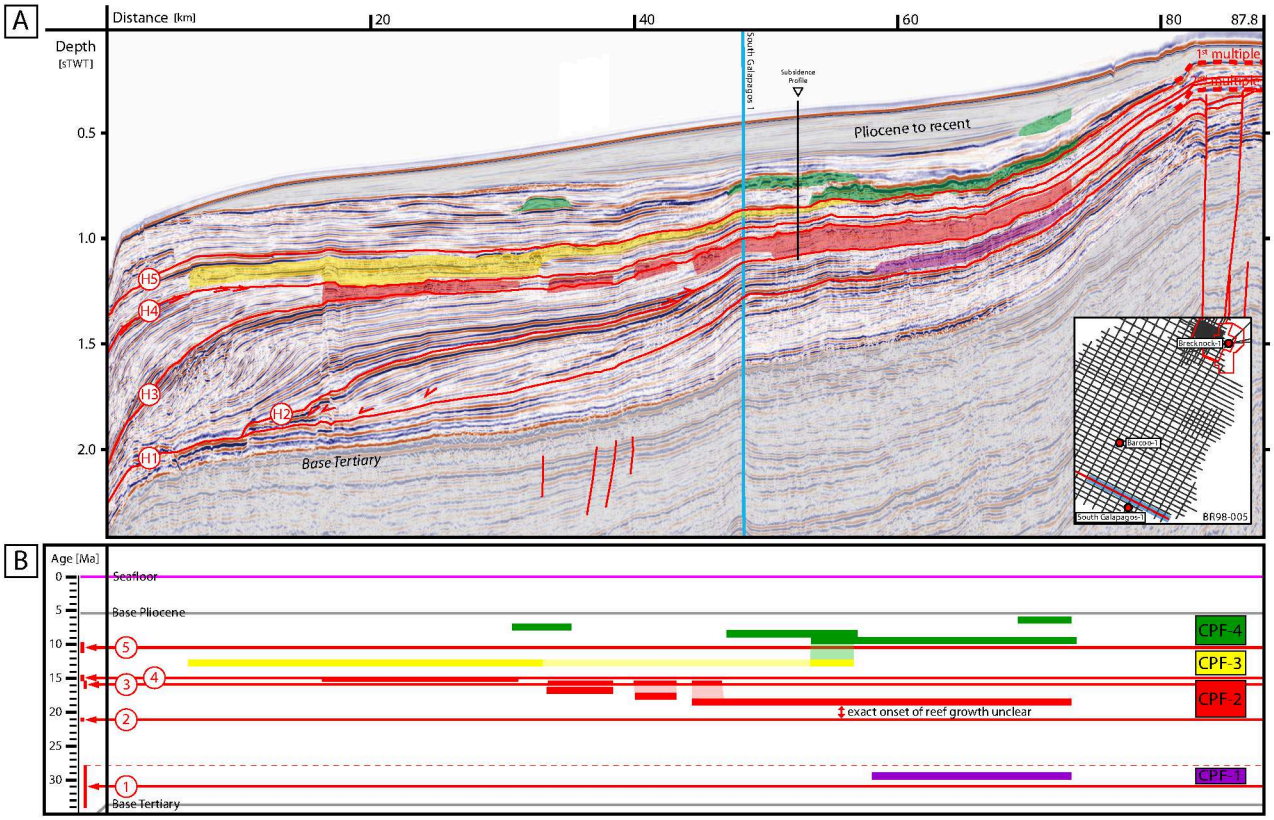

Figure 2.6: *Seismic-reflection section of line BR98-005 (A) located in the south of the study area (see inset), showing the mapped carbonate platform facies intervals (CPF-1: purple, CPF-2: red, CPF-3: yellow, CPF-4: green). Reference horizons are indicated as continuous red lines and seismic multiples in dashed bold red lines. The position of the subsidence profile shown in figure 2.11A is indicated by a black line. Near vertical seismic discontinuities extending downward from the seaward edge of CPF-2 and CPF-3 are interpreted as seismic artefacts, resulting from a strong relative contrast in sonic velocity between the material of the discontinuity zones and the surrounding sediments. The chronostratigraphic plot (B) below the seismic section emphasizes progradation and retrogradation within the mapped carbonate platform facies; approximate ages of the reference horizons are constrained by biostratigraphic data of well Barcoo-1, except for the age of H5 which is derived through horizon correlation from Sr-ages of well Brecknock-1 and microfossil data of well North Scott Reef-1 (Table 2.1).*

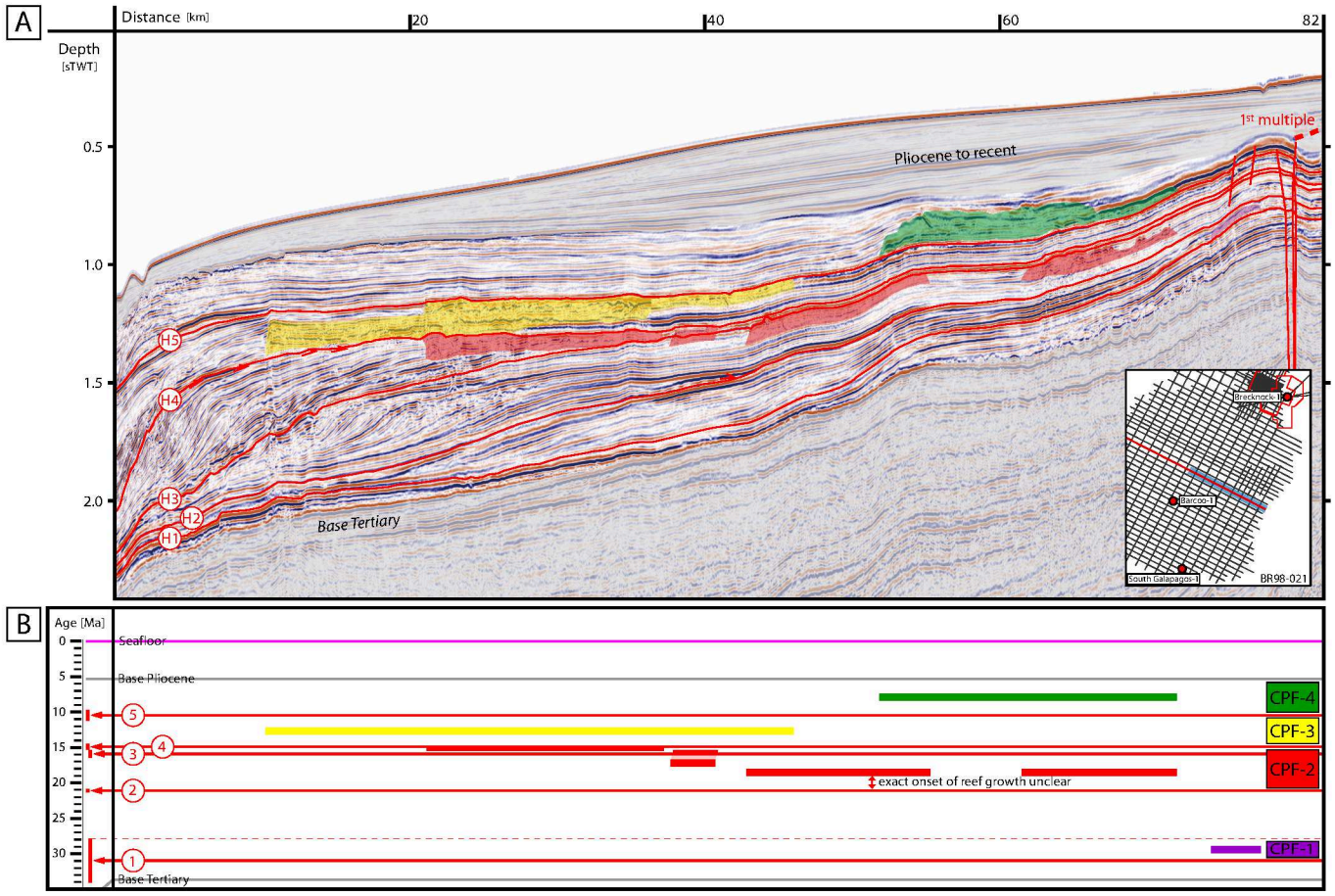

Figure 2.7: *Seismic-reflection section of line BR98-021 (A) located in the south of the study area (see inset), showing the mapped carbonate platform facies intervals. Reference horizons are indicated as continuous red lines and seismic multiples in dashed bold red lines. Near vertical seismic discontinuities extending downward from the seaward edge of CPF-3 are interpreted as seismic artefacts. The chronostratigraphic plot (B) below the seismic section emphasizes progradation and retrogradation within the mapped carbonate platform facies; approximate ages of the reference horizons are constrained by biostratigraphic data of well Barcoo-1, except for the age of H5 which is derived through horizon correlation from Sr-ages of well Brecknock-1 and microfossil data of well North Scott Reef-1 (Table 2.1).*

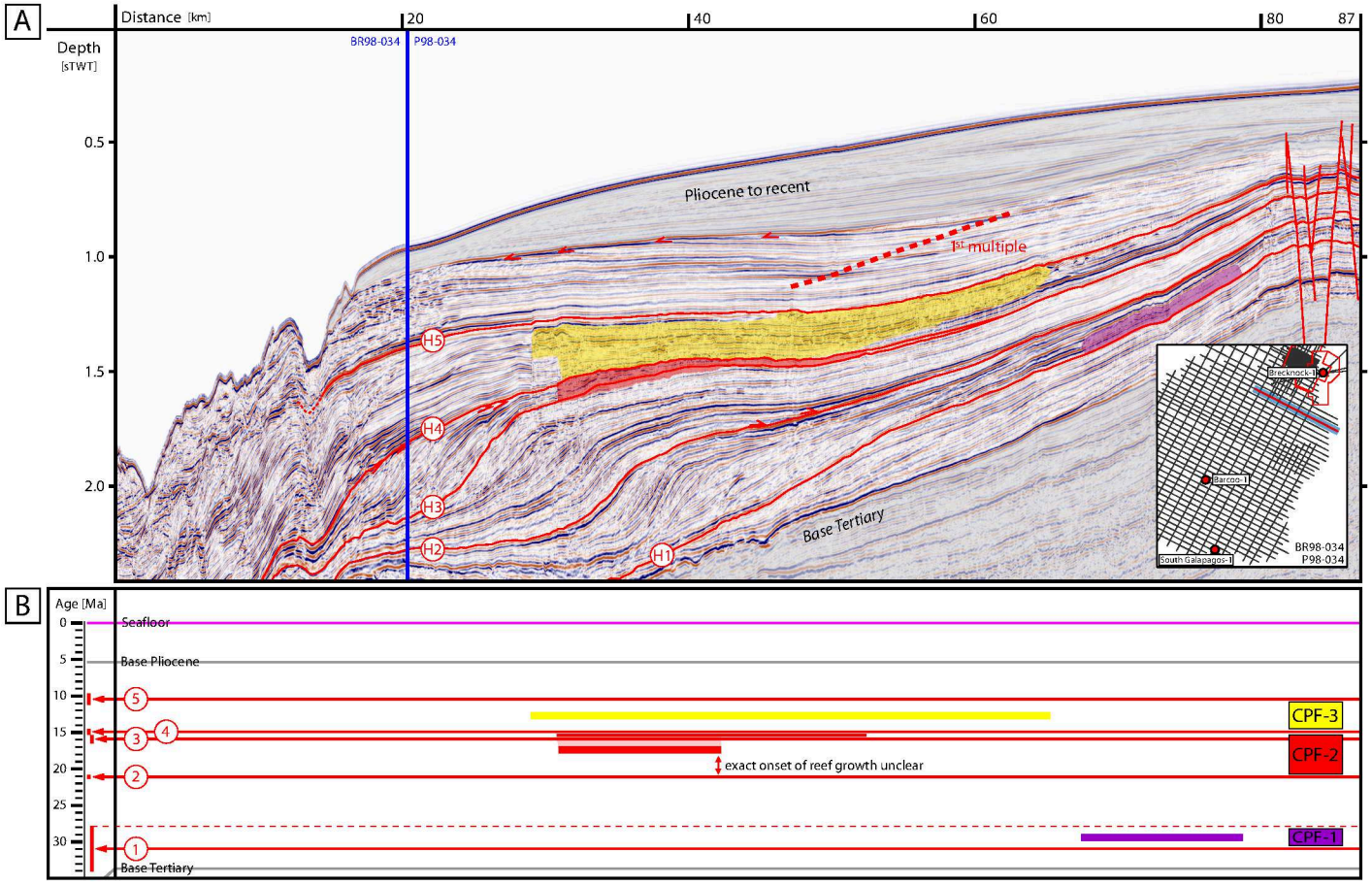

Figure 2.8: *Seismic-reflection section of line BR98-034 (A) located in the south of the study area (see inset), showing the mapped carbonate platform facies intervals. Reference horizons are indicated as continuous red lines and seismic multiples in dashed bold red lines. Near vertical seismic discontinuities extending downward from the seaward edge of CPF-3 are interpreted as seismic artefacts. The chronostratigraphic plot (B) below the seismic section emphasizes progradation and retrogradation within the mapped carbonate platform facies; stratigraphic age approximations for the seismic horizons are provided by microfossil data and Sr-age dates from well Barcoo-1, Brecknock-1 and North Scott Reef-1 (Table 2.1).*

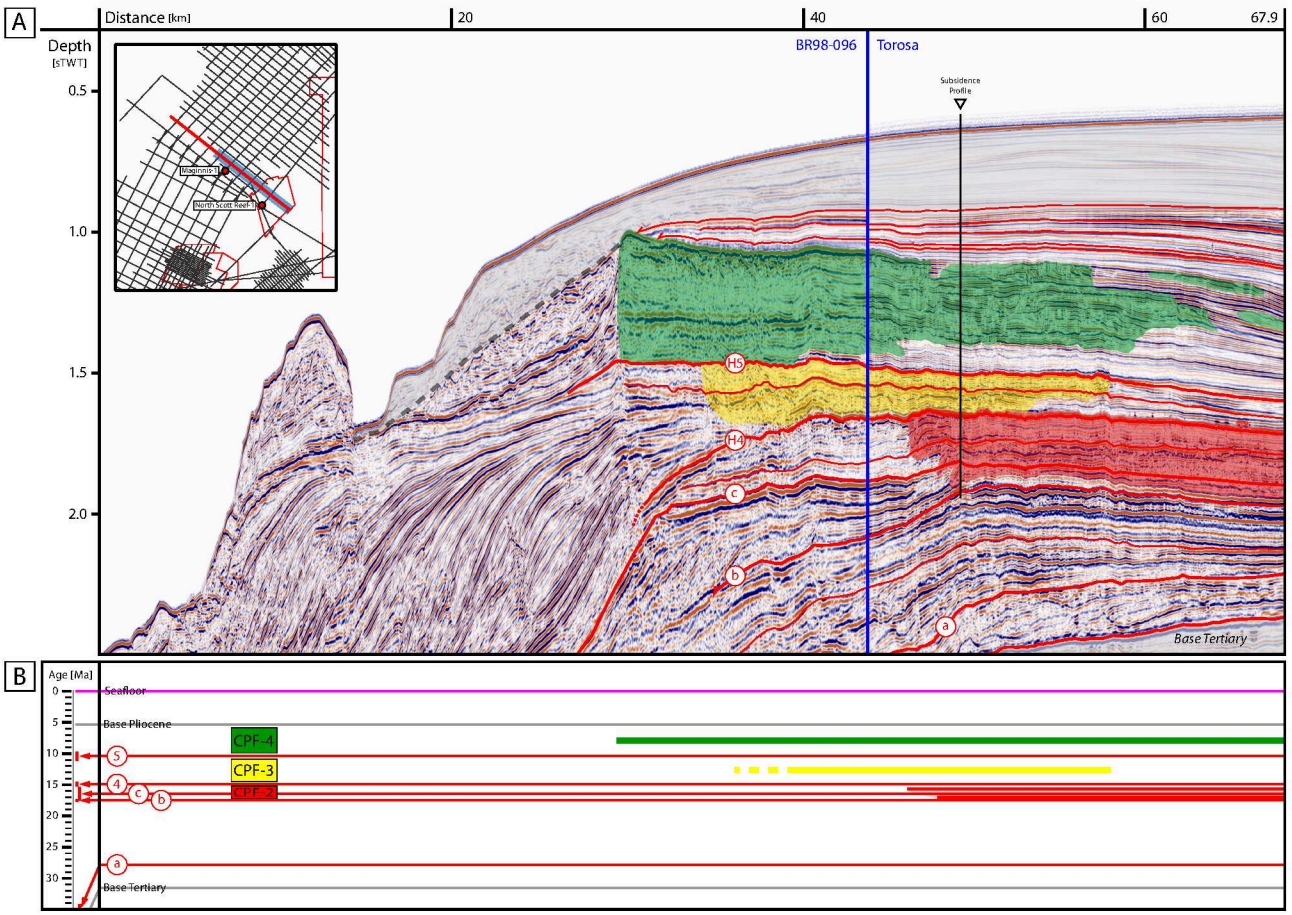

Figure 2.9: *Composite seismic-reflection section of the line BR98-096 and an arbitrary line across the Torosa 3D seismic survey (A) in the north of the study area (see inset), showing the mapped carbonate platform facies. Reference horizons are indicated as continuous red lines. The position of the subsidence profile visualized in figure 2.11B is indicated by a black line. Near vertical seismic discontinuities extending downward from the seaward edge of CPF-4 are interpreted as seismic artefacts. The chronostratigraphic plot (B) below the seismic section emphasizes progradation and aggradation within the mapped carbonate platform facies. Stratigraphic age approximations for the seismic horizons are provided by wells North Scott Reef-1 (Table 2.1) and Maginnis-1.*

Between horizon H5 and the Miocene-Pliocene boundary, seismic reflections are generally of medium amplitudes, subparallel to parallel and semi-continuous with the exception of areas characterized by seismic carbonate platform facies (CPF-4). In the very south of the study area high-amplitude, mounded, laterally restricted zones of seismic carbonate platform facies can be identified (Figs. 2.6 & 2.7), whereas no seismic carbonate platform facies is visible within this interval in the north central study area (Figs. 2.8 & 2.12C). In the very north of the study area CPF-4 occurs in massive, laterally restricted structures of low internal reflectivity representing an escarpment margin (Fig. 2.9). 3D variance data of the northern Browse area documents the presence of ellipsoidal, landward prograding isolated platforms in this interval (Fig. 2.12D).

2.5.4 Geomorphology, distribution and chronostratigraphy of the carbonate platform facies

Carbonate platform facies 1 (CPF-1)

CPF-1 has a comparatively indistinct seismic-geomorphological signature in comparison to the other carbonate platform facies intervals and is only imaged on lines in the south of the BR98 2D survey and on the eastern edge of the Brecknock 3D seismic-reflection survey. The top of CPF-1 increases in depth towards the north (Fig. 2.10A). The discontinuity facies forms an up to 100 ms TWT thick belt of 220 km length with a width of up to 17 km, which is in places intermittent but has an overall form resembling an elongate barrier of fringing reef (Fig. 2.10A).

Carbonate platform facies 2 (CPF-2)

CPF-2 was mapped in the south of the BR98 2D survey, throughout the Brecknock and Brecknock South 3D surveys, across one Firetail 2D seismic line into the Torosa 3D seismic survey, and back further north onto the BR98 2D seismic survey (Fig. 2.11A). The top of CPF-2 increases towards the north, its front increasing in depth from 1.22 s TWT in the south to 1.67 s TWT in the north. CPF-2 displays the morphological form of an elongate platform bound on its seaward side by an intermittent barrier reef. The carbonate platform extends for ca. 360 km across the study area from south to north. In the southern

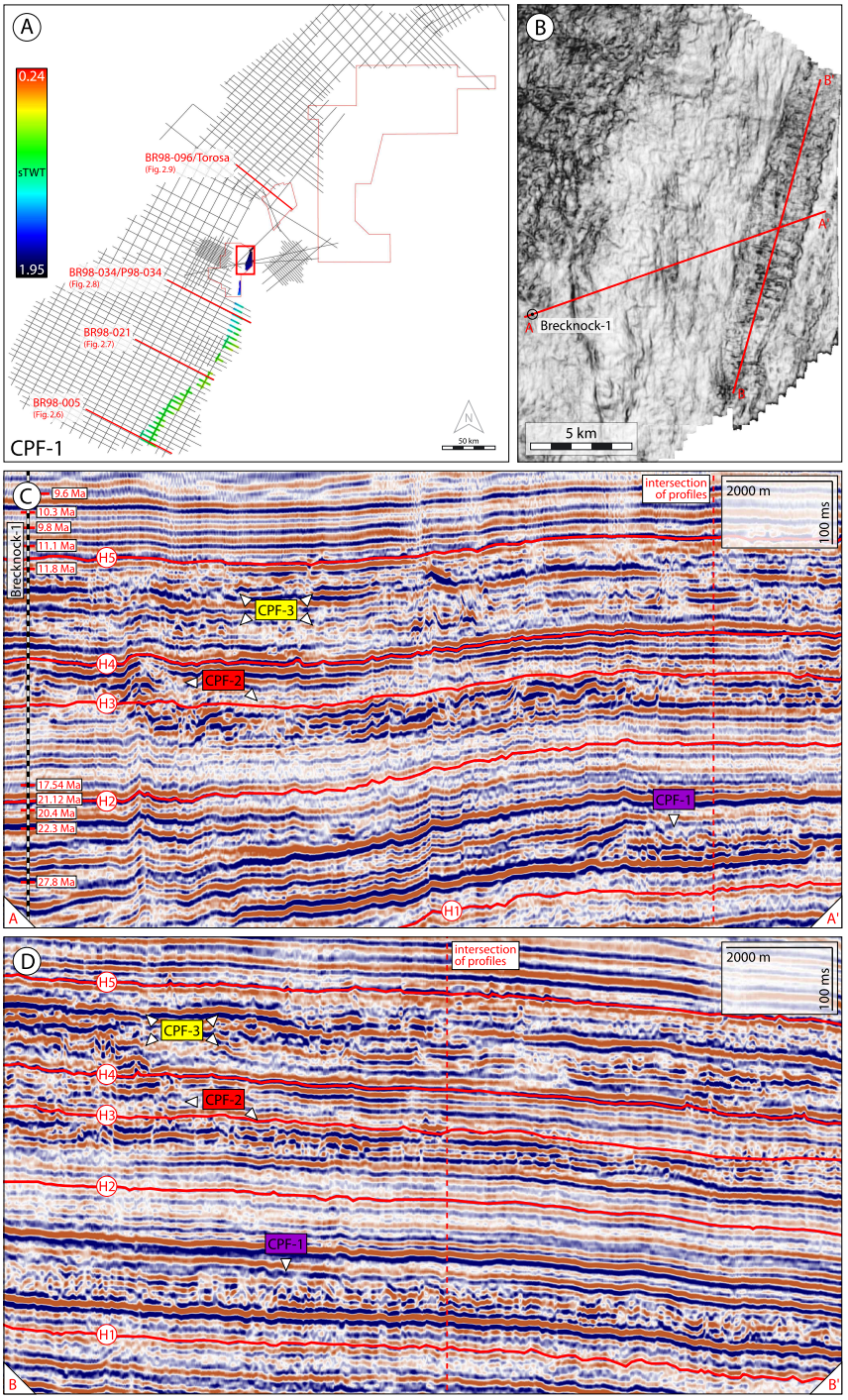

Figure 2.10: *Lateral distribution of the carbonate platform facies interval CPF-1 with exemplary variance data and vertical sections. (A) Depth map showing the top of CPF-1, which has the form of a narrow platform belt that extends over approximately 220 km with a width of up to 17 km. (B) Variance horizon slice intersecting CPF-1 in the Brecknock 3D seismic survey. (C-D) Seismic-reflection sections of an arbitrary line between the well Brecknock-1 and CPF-1 (A-A'), and an arbitrary line along CPF-1 (B-B'). The sections show the similarity between the seismic signatures of CPF-2 and CPF-3 which are interpreted as carbonate platforms and CPF-1 which may alternatively be interpreted as a bryozoan reef-mound complex. Reference horizons are marked in red.*

and south-central study area it is up to 55 km wide and contains a central lagoon with restricted reef growth. This lagoon is bound on its landward side by another reef belt, landward of which a shelfal lagoon (apparently lacking reefs) developed. The width of CPF-2 decreases because of the width of the central lagoon to 14 km in the Brecknock region, after which it expands again to around 50 km in the Torosa region and 80 km in the Northern Browse region, where the reef belt splits up in several isolated platforms of sizes up to several tens of kilometres that are separated by narrow channels (Fig. 2.11B). The age of CPF-2 can be constrained to lie between approximately 16.38-14.53 Ma in the south and 17.54-14.53 Ma in the north (Table 2.1; Figs. 2.4, 2.6B, 2.7B, 2.8B, 2.9B). The ages for the onset of reef development vary in both areas due to the different age datums available (Fig. 2.4). Since in both cases the base of the carbonate platform facies does not correspond directly to an age marker, reef development may nevertheless have begun at the same time in both areas.

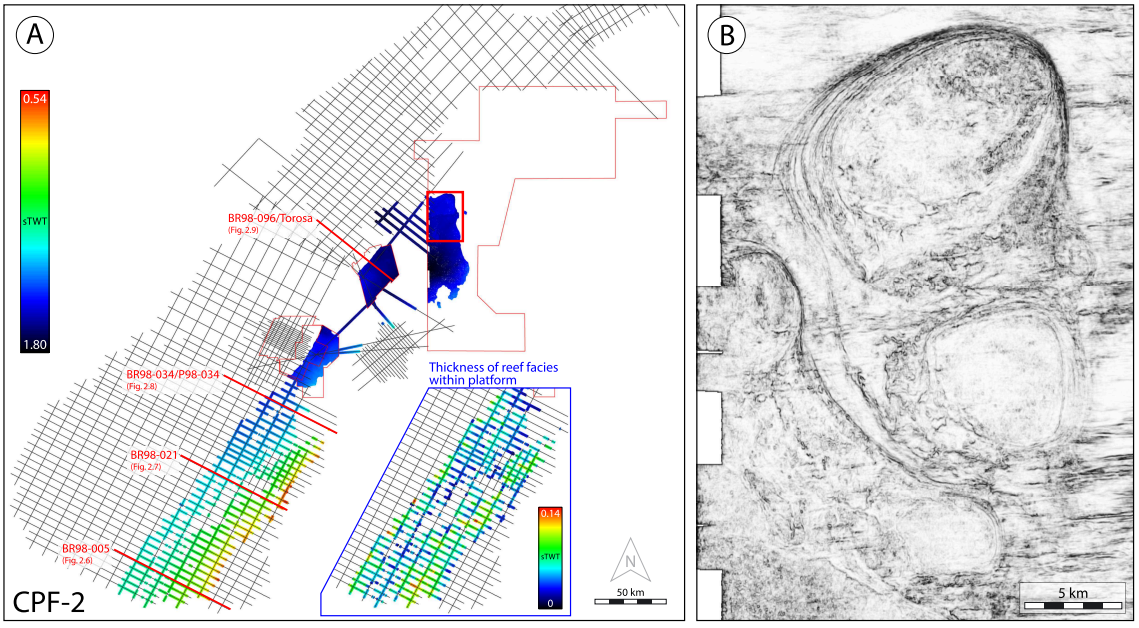

Figure 2.11: *Lateral distribution of the carbonate platform facies interval CPF-2 with exemplary variance data. (A) Depth map showing the top of CPF-2, which extends over 360 km and consists of a seaward barrier reef, visible on the Brecknock and Torosa surveys. Isolated carbonate platforms characterize the landward side of the reef. At its narrowest point in the Brecknock region, the carbonate platform facies belt is 14 km wide, but up to 80 km wide in the north of the study area. (B) Variance timeslice at 1.712 s TWT showing CPF-2 in the Northern Browse 3D seismic survey.*

Carbonate platform facies 3 (CPF-3)

CPF-3 is interpreted to indicate the most seaward reef-rimmed carbonate platform (Fig. 2.12A) exhibiting a distinct reef-front signature in the southern, south-central and north-central study area (Figs. 2.5B & 2.12B). In the northern study area the massive bulk of CPF-4 rests upon the reef-front of CPF-3 (Fig. 2.9), making its exact position difficult to identify due to imaging artefacts. The top of CPF-3 dips towards the north, its front increasing in depth from 1.15 s TWT in the south to 1.5 s TWT in the north (Fig. 2.12A). CPF-3 in general has the form of an extensive platform rimmed by a continuous barrier reef. In the very south of the study area in particular, CPF-3 thins out severely on its landward side (Fig. 2.12A), showing several indentations into the reflectors above (Figs. 2.6 & 2.7), possibly indicating the presence of patch reefs (Fig. 2.12B). According to these observations, retrogradation of CPF-3 is much stronger in the very south of the study area than further north, which is also in agreement with the observations of Rosleff-Soerensen et al. (2016, their figure 8). The top of CPF-3 is indistinct where it is closely overlain by CPF-4, suggesting a direct transition between these two carbonate platform facies intervals. In the south, CPF-3 is located approximately 10 km farther seaward than CPF-2, a distance that decreases to a few kilometres in the Brecknock area (Figs. 2.11A & 2.12A). In the Torosa area the reef fronts of CPF-2 and CPF-3 are approximately 6 km apart. CPF-3 extends from south to north over at least 500 km, and has a width of 25-38 km in the south, which decreases northwards to less than 18 km in the Torosa area, before increasing again to approximately 60-70 km in the Northern Browse area (Fig. 2.12A). The thickness of CPF-3 generally increases from the south to the north of the study area (Fig. 2.12A). CPF-3 formed approximately between 15.10-9.83 Ma (Table 2.1; Figs. 2.4, 2.6B, 2.7B, 2.8B, 2.9B).

Carbonate platform facies 4 (CPF-4)

CPF-4 was mapped in the south of the BR98 2D survey and correlated stratigraphically using data from well North Scott Reef-1 (Fig. 2.3) into the Torosa 3D and central BR98 2D surveys (Fig. 2.12C). In the south the top of CPF-4 dips in the direction of the slope. The seaward and landward boundaries of CPF-4 have an arcuate form, indicating it to be composed of multiple elliptical platforms that are connected in places or dissected by

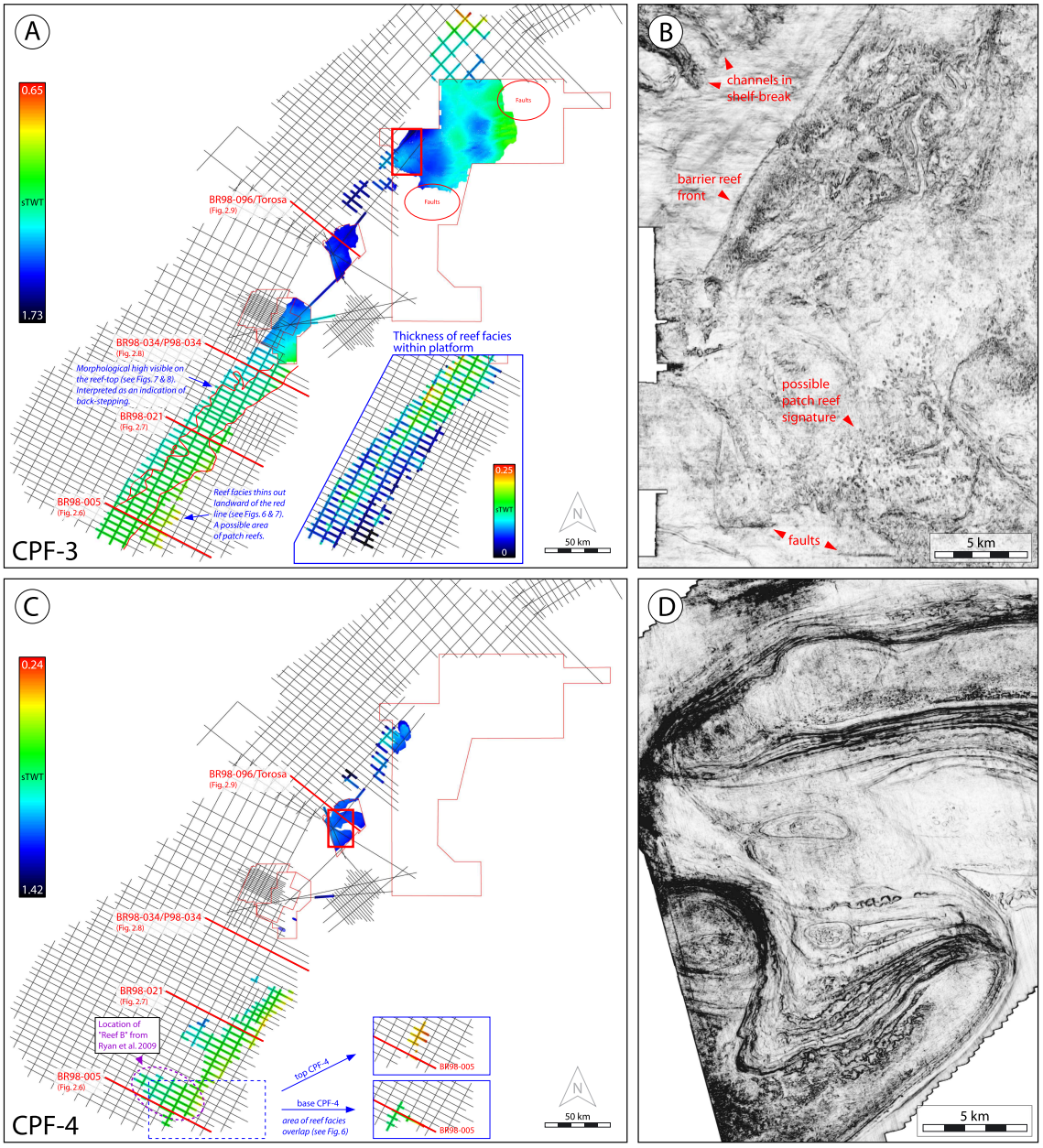

Figure 2.12: *Lateral distribution of carbonate platform facies intervals CPF-3 and CPF-4 with exemplary variance data. (A) Depth map showing the top of CPF-3. This is the most seaward of the studied reefs and extends over at least 500 km along the shelf. In the south it has the form of a barrier reef with a width of 25-38 km that decreases to less than 18 km in the Torosa area, further north of which isolated carbonate platforms begin to appear. CPF-3 has a width of approximately 60-70 km in the Northern Browse area. (B) Variance horizon slice intersecting CPF-3 in the Northern Browse 3D seismic survey. (C) Depth map showing the top of CPF-4, the youngest carbonate platform interval observed, which consists mainly of isolated buildups. In the south of the study area, multiple overlying isolated carbonate platform facies build-ups (also see Fig. 2.5) are plotted individually as insets. (D) Variance timeslice at 1.152 s TWT showing CPF-4 in the Torosa 3D seismic survey.*

channels (Fig. 2.5A). Bachtel et al. (2011) have analysed this interval of carbonate platforms in detail in the Torosa region and attribute the complex morphology visible there to phases of initiation, coalescence, backstepping (Fig. 2.12D) and terminal drowning in a current influenced setting. In the south of the study area a circular platform of CPF-4 (Fig. 2.12C) corresponds to "Reef B" of Ryan et al. (2009), who constrain its age between the middle and late Miocene. In this study the age of CPF-4 can be constrained as younger than 11.1 Ma by the available data (Table 2.1; Figs. 2.4, 2.6B, 2.7B, 2.8B, 2.9B), with Rosleff-Soerensen et al. (2016) interpreting an age of less than 9.7 Ma. In the southernmost extents of the BR98 survey several independent reef rimmed platforms within CPF-4 occur above one another (Figs. 2.6 & 2.12C).

2.5.5 Platform development through time

In the southern, south-central and north-central study area, the distribution of the carbonate platform facies shows progradation between CPF-1 and CPF-3, and the onset of significant retrogradation within CPF-3 (Figs. 2.6-2.8) continuing into CPF-4. On line BR98-005 (Fig. 2.6B) an additional phase of platform progradation and retreat can be seen within CPF-4. The northern study area shows a rather continuous platform progradation from CPF-2 to CPF-4 followed by significant aggradation within CPF-4 (Fig. 2.9). The vertical sequence of reefs is furthermore characterized by an overall reduction of gaps within CPF-2 towards the north (Figs. 2.6-2.9), and also the local disappearance of CPF-4 (Fig. 2.7). In the very north of the study area, CPF-1 seems to have terminated and only CPF-2 to CPF-4 are observed (Fig. 2.9). The front of the most extensive carbonate platform interval CPF-3 is always positioned further seaward than that of the underlying CPF-2 in the southern study area, although the distance between the two reef-fronts grows narrower towards the Brecknock area. This is most likely due to steeper slopes in this area resulting in a narrower region in which reef growth may occur (cf. Rosleff-Soerensen et al. 2016). In contrast, the reef-front of CPF-4 is the most seaward in the north. Due to the imaging artefacts caused by the massive carbonate build-ups in CPF-4, the exact seaward termination of CPF-3 is difficult to establish, but it appears to be located not as far seaward as CPF-4.

2.6 Discussion

The seismic interpretation has shown that a considerable variation within the carbonate platform facies architecture exists between the southern and northern study areas. This is reflected in the generally larger reef facies thicknesses and more seaward position of the reef front of CPF-4 in the north. In general CPF-4 shows a high variability in its lateral distribution, while the reef generations of CPF-2 and CPF-3 are easily identified due to their strong similarity throughout the entire study area. The architecture of CPF-1 shows very little variation, but is only imaged in the southern study area. Initial carbonate platform development (CPF-1) in the southern study area initiated on an unrimmed shelf, on the topsets of Oligocene carbonate clinoforms (Figs. 2.6-2.8). The relatively flat top of the discontinuity zone (Fig. 2.10C, D) is suggestive of a depositional process associated with a physical barrier such as the sea surface. In connection with seaward-dipping reflection foresets (Fig. 2.10C) and intercalated areas of high reflection continuity, possibly indicating lagoons (Fig. 2.10C), CPF-1 could be interpreted as a reef-rimmed carbonate platform. With an age between 34.03 and 27.8 Ma, this would be the oldest tropical reef documented along the NWS so far. In SE Asia coral reefs are isolated occurrences in the Oligocene, forming smaller barrier reefs and patch reefs in carbonate systems dominated by larger benthic foraminifera (Wilson 2015). Coral dominated carbonate systems only became widespread after the Oligocene/Miocene boundary, substantially after the Oligocene expansion of coral reefs in other parts of the world including the Mediterranean or the Caribbean (Wilson 2008). This is partly attributed to the equatorial humid environment under which the carbonates in SE Asia developed during the Oligocene. At 31 Ma the central Browse Basin was situated at $\sim 28^{\circ}$ S (van Hinsbergen et al. 2015) and therefore likely experienced more arid conditions than most SE Asian carbonates. This could have fostered an early dominance of a coral dominated carbonate system on the NWS.

An interpretation as bryozoan reef-mound complex would be an alternative, possibly more reconcilable with the lower temperatures along the NWS during the middle to late Oligocene (McGowran et al. 2004) than a tropical reef. The dimensions of CPF-1 could also be easily matched by a bryozoan reef mound complex, as an example by Sharples

et al. (2014) from the Great Australian Bight shows, where cumulative lengths of several hundreds of kilometres and widths of up to 17 km were documented. Against an interpretation as bryozoan reef mound complex however speaks the relatively flat top of CPF-1 and its location landward of the assumed palaeo shelf-break (Figs. 2.6-2.8). Based on the available data the origin of CPF-1 can not be conclusively resolved, as the internal structure on the seismic sections is not imaged in enough detail due to its low thickness. The seismic signature however has strong similarities, e.g. discontinuous medium to high amplitude reflectors, to those interpreted as tropical reefs in this study (Figs. 2.5 & 2.10). Should CPF-1 indeed correspond to a tropical reef-rimmed platform, the first reef development in the study area would have occurred as early as between 34.03 and 27.8 Ma. After this period no further signs of reef development are documented until around 17.54-16.38 Ma, when continuous reef development in the form of the seismic discontinuity zones CPF-2 and CPF-3 began, which also formed on the topsets of clinoforms (Figs. 2.6-2.9). Throughout the study area, carbonate platform progradation seems to be restricted by the increase in slope of the underlying clinoform foresets, which can also be seen at the base of CPF-4 in the very north of the study area (Fig. 2.9). The more southern reef-rimmed platforms of CPF-4, however, retrograded into positions up to 40 km landward of their CPF-3 predecessors, thus are all located at significant distance to the slope break with isolated platforms and reef patches widely distributed across the shelf.

The depth maps of the individual carbonate-platform tops all show a pronounced northward increase in their present-day depth location (Figs. 2.10, 2.11, 2.12), which indicates a general northwards increasing regional subsidence trend in the study area after deposition (cf. Rosleff-Soerensen et al. 2016). If compared with the lateral thickness variation within each facies interval, it seems that for CPF-1 and CPF-2 this northward tilt occurred post-depositionally, as the respective platform thicknesses within these intervals are rather constant (e.g. Fig. 2.11A inset). The thickness of CPF-3, however, significantly increases towards the north (Fig. 2.12A inset), likely reflecting that the carbonate system counteracted higher northern subsidence rates with increased production and upward growth. The thickness distribution of CPF-4 is, because of its patchy and inboard location at the edge of the seismic dataset, difficult to establish. However, CPF-4 also appears to

reach its maximum thickness in the very north of the study area (Fig. 2.9). It is thus likely that both CPF-3 and CPF-4 experienced northwards increasing, laterally differential subsidence during platform growth, contrasting a regionally uniform subsidence trend during the development of CPF-1 and CPF-2 that led to laterally homogenous platform thicknesses. This difference can be interpreted to document the onset of a downward bending of the northern part of the Browse Basin between the development of CPF-2 and CPF-3, thus around 15 Ma (Fig. 2.4). A regional tectonic event that approximately corresponds to the time interval between 15 and 10 Ma is the Java trench developing eastward in a new position (Banda Trench of Audley-Charles 2004) in association with the beginning of the Banda Volcanic Arc (Audley-Charles 2004; Hall 2009), which was, however, located at that time >500 km north of the study area (Hall 2002).

Figure 2.13 shows subsidence curves calculated for the northern and southern study areas at two exemplary positions (see Figs. 2.6 & 2.9) based on seismic horizon interpretations, stratigraphic ages derived from wells North Scott Reef-1, Brecknock-1 and Barcoo-1 (Table 1), and estimated seismic-interval velocities of 1500, 2000 and 3000 $\frac{m}{s}$ for water, shallow sediments and carbonate platform facies respectively. For subsidence calculation (Fig. 2.13A), the mapped facies intervals were used as a palaeo-waterdepth indicator, constraining the palaeo-depositional surface to a depth of 0-30 m. Approximated ages for the other horizon levels (Figs. 2.6 & 2.9) were excluded from the subsidence estimation since they are ambiguous with respect to their palaeo-waterdepth. The comparison of the northern and southern burial trends (Fig. 2.13A) shows from ca. 15 Ma onwards a generally high northern subsidence with an average long-term rate of ca. 125 $\frac{m}{Ma}$, as opposed to a lower subsidence in the south with an average long-term rate of ca. 64 $\frac{m}{Ma}$. The Miocene to recent subsidence estimates of Rosleff-Soerensen et al. (2016) of 102 $\frac{m}{Ma}$ and 83 $\frac{m}{Ma}$ on a different seismic dataset and at more seaward locations within the central and southern study area fall in-between these values. The late Miocene (10 Ma to recent) subsidence rates calculated by Czarnota et al. (2013) north of the study area are with ca. 60 $\frac{m}{Ma}$ less than half of the northern estimates of this study (Figs. 2.9 & 2.13A). It has to be kept in mind when discussing these trends that the observed results may depend considerably on the chosen location. Factors influencing subsidence calculation in this study include in particular the proximity to the Barcoo Fault Zone in the south,

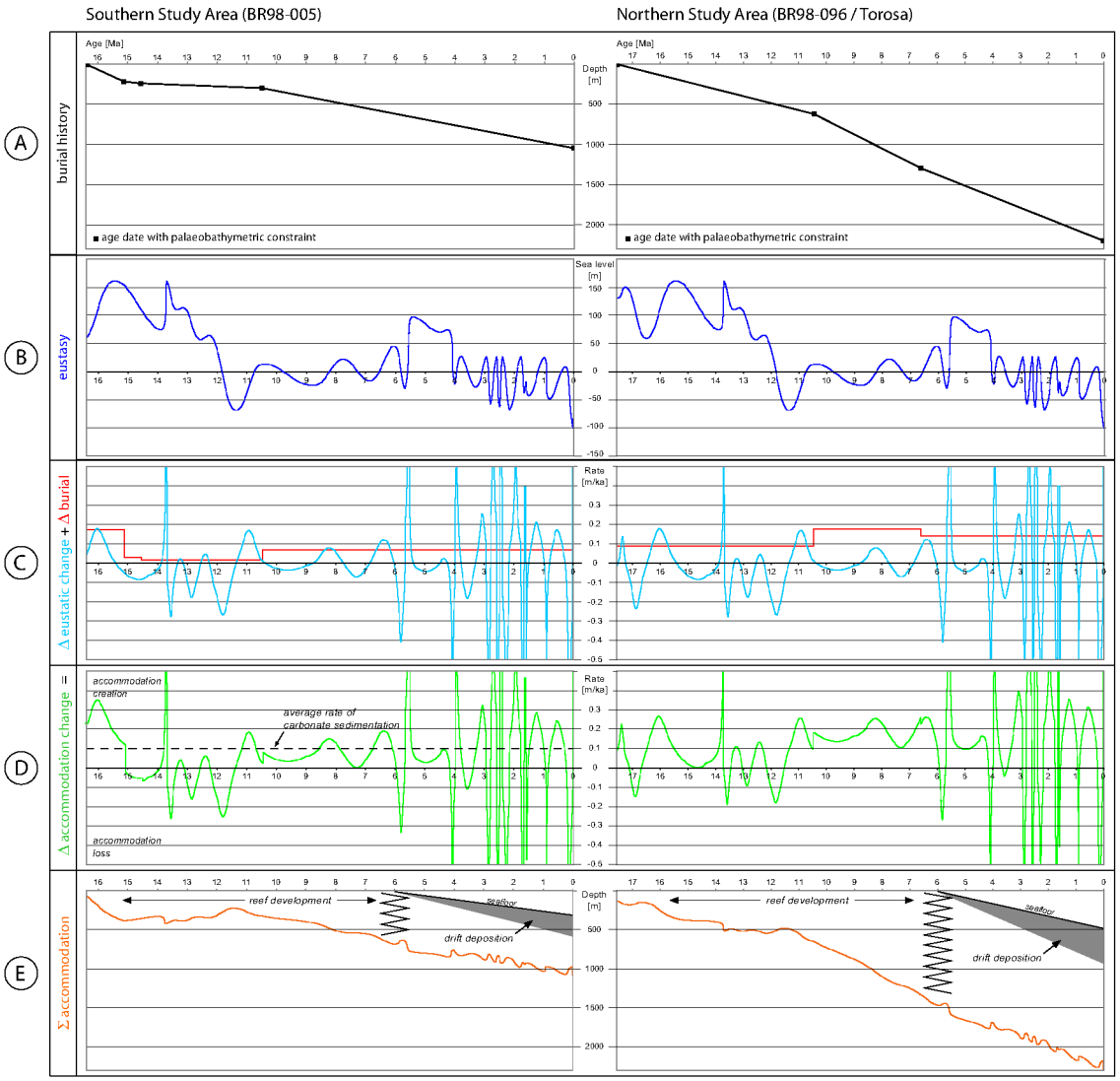

Figure 2.13: *Concept for evaluating the influence of eustasy and variable subsidence based on subsidence analysis at two exemplary study sites located on seismic-reflection line BR98-005 in the south of the study area (Fig. 2.5) and composite seismic-reflection section of line BR98-096/Torosa in the north (Fig. 2.8), using the interpreted carbonate platform facies as palaeo-waterdepth indicator. (A) Burial history based on time-depth conversion applying average seismic-interval velocities of 1500, 2000 and 3000 $\frac{m}{s}$ for water, shallow sediments and carbonate platform facies respectively. The calculated long-term subsidence is $\sim$ 64 $\frac{m}{Ma}$ in the south and $\sim$ 125 $\frac{m}{Ma}$ in the north. (B) Eustatic sea-level curve of Hardenbol et al. (1998). (C) Rate of eustatic change calculated from the eustatic curve shown in light blue. Rate of burial (expressing the rate of accommodation creation and loss) shown in red. (D) Rate of accommodation change (relative sea-level change) through time calculated as the sum of the rate of eustatic change and the rate of burial shown in green. Positive portions of green curve indicate times of cumulative accommodation creation under consideration of both eustatic change and burial history; negative parts of green curve indicate times of accommodation loss. Dashed black line shows an average rate of carbonate accumulation of 0.1 $\frac{m}{ka}$, based on Kemp et al. (2014). Intersections between this line and the green curve emphasize periods characterized by an accommodation surplus (black < green), in which reef retrogradation could have happened. Periods characterized by a general accommodation deficiency (black > green > 0) indicate times in which a sedimentary surplus could have lead to reef progradation. (E) Cumulative available accommodation space with respect to palaeo-sealevels.*

which may have locally influenced the observed burial-depth, and lateral thickness variations within the overall seawards divergent sedimentary succession (e.g. Fig. 2.6). To evaluate the potential impact of combined changes of subsidence and sea level on reef development, the rates of accommodation creation or loss through time by subsidence and eustasy (Fig. 2.13B; eustatic curve of Hardenbol et al. 1998) were measured from old to young in 1 ka increments (Fig. 2.13C). Figure 2.13D plots the sum of the rates of accommodation change through time by eustasy and subsidence in m per ka, separating intervals of accommodation creation (positive values) from intervals of accommodation loss (negative values).

A comparison between the southern and northern study sites with respect to accommodation change through time (Fig. 2.13D) shows although different in magnitude a similar trend of relative sea-level change. The interval between ~16.38 and 15.1 Ma is dominated by accommodation creation, a period between ~14 and 11.4 Ma with major fluctuations between accommodation creation and loss, and a time span between ~11.4 and 6 Ma is characterized by the re-establishment of conditions of dominant accommodation creation. If compared with the thickness of carbonate platform facies at the measurement sites, the intervals dominated by accommodation creation (CPF-2, CPF-4) seem to have led to the development of thicker platforms, the phase of major highs and lows in relative sea level (CPF-3) to thinner systems (Figs. 2.6 & 2.9). It is remarkable that at both, the southern and northern study sites, reef-rimmed platforms of CPF-2, CPF-3 and CPF-4 managed to survive intervals of accommodation creation with rates of 0.3 $\frac{m}{ka}$ and above, requiring accumulation rates significantly above average to remain within the reef-growth window (e.g. McNeill 2005; Kemp et al. 2014). In turn, the Miocene Browse Basin carbonate platforms also survived intervals of major accommodation loss (e.g. ~12.2 to 11.4 Ma), in which the studied sites might have been exposed to subaerial conditions (as documented by Rosleff-Soerensen et al. (2012) in the nearby Brecknock area). Figures 2.13B and D further show that the major eustatic fluctuations between 6 Ma and today triggered high-frequency and high-amplitude oscillations in the rates of accommodation creation, which approximately coincide with the times of termination of carbonate platform development at the studied sites. If plotted with respect to the sum of relative sea-level change (Fig. 2.13E), these high-frequency and high-amplitude sea-level

variations only attenuate (fall) and amplify (rise), but do not completely change the overall subsidence-dominated accommodation pattern. The measurement of the interplay of eustatic change and subsidence (Fig. 2.13) thus does not provide a solely accommodation-driven explanation by e.g. long-term subaerial exposure or abrupt drowning for the decay of the Browse Basin carbonate platforms around the Miocene-Pliocene boundary, which have previously documented an enormous robustness to comparable sea-level changes over a long time span. However, what significantly changes around 6 Ma is the sedimentary system, switching from reef accumulation to drift sedimentation. Averaged sedimentation rates during drift deposition (omitting potential erosional periods) at the measured sites were around 0.04 $\frac{m}{ka}$ (south; Fig. 2.6) and 0.08 $\frac{m}{ka}$ (north; Fig. 2.9). This is significantly lower than during the period of reef growth, ultimately leading to underfilled basin conditions with subsidence rapidly outpacing sedimentation (Fig. 2.13E).

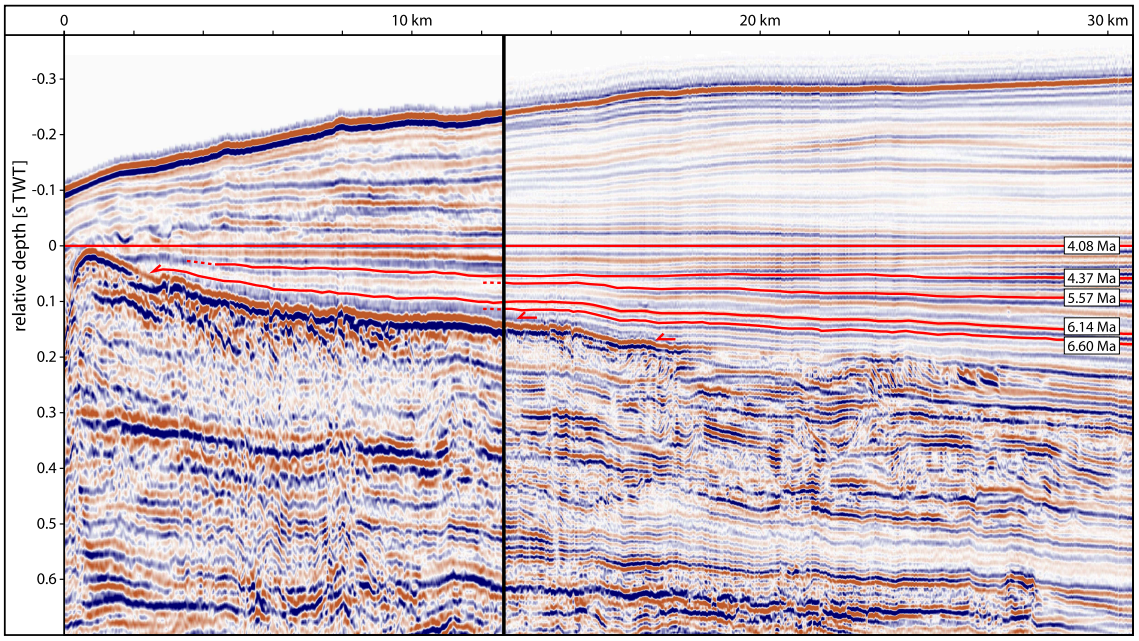

Figure 2.14: *Part of seismic-reflection section BR98-096/Torosa (Fig. 2.8) flattened to the seismic reflector dated at 4.07 Ma (age data provided by nearby well North Scott Reef-1, see Table 2.1). This illustration highlights the burial history of the youngest palaeo-reefs (CPF-4) in the northern study area through sediment drifts. Onlaps onto the reef top begin to develop around 6.6 Ma. For details on eustatic and accommodation change at this site between 6 and 4 Ma see figure 2.13.*

Figure 2.14 emphasises the unconformable and successive coverage of CPF-4 by sediment drifts on the landward side since ca. 6.6 Ma. Figures 2.6, 2.7 and 2.8 additionally

document that late Miocene/Pliocene platform burial by drift deposits was not a local phenomenon, but a regional process. The lateral transition between carbonate platform facies and drift deposits (Figs. 2.6, 2.7, 2.9, 2.14) suggests that the terminal phase of platform development coincided with considerable current-driven drift sedimentation, initially affecting morphological lows and successively conquering former structural highs (Fig. 2.14). Bachtel et al. (2011) have shown that current activity during the development of CPF-4 was already strong enough to significantly influence the reef development in the Torosa region. The effects of an increased current activity on reef development in the study area however could have been manifold, e.g. also leading to a higher suspended load in the water column narrowing the photic zone and changing nutrient levels, or introducing waters of different temperature or salinity to the study area. Such effects might have disturbed the ecological balance of the reef-building organisms, reducing carbonate production until it could no longer compete with the generally very high subsidence. However, the ultimate cause for the onset of dominantly current-controlled sedimentation in the study area remains unclear. With the given data and interpretation results it can only be speculated that e.g. regional changes in water temperature and/or salinity as result of a possibly tectonically triggered interruption or reduction of the Indonesian Throughflow (Kennett et al. 1985; Gallagher et al. 2009; Karas et al. 2011; Rosleff-Soerensen et al. 2012) could have led to significant changes in the oceanic current regime of the Browse Basin.

2.7 Conclusions

1. The analysis of an extensive 2D and 3D seismic-reflection dataset tied to borehole data documented the presence of numerous carbonate platforms in the subsurface of the Browse Basin offshore NW Australia. The oldest platform documented is of Oligocene age (34.03 - 27.8 Ma), and can be interpreted either as a reef-rimmed platform or a giant bryozoan reef-mound complex located on the topsets of a heterozoan ramp.

2. A major reef-rimmed platform belt extending over 500 km in NE-SW direction across the Browse Basin developed in the Miocene between 15.1 to 9.83 Ma. This platform belt

documents remarkably little variation along its length considering the large area under study. Antecedent topography seems to have played an important role in controlling reef development, which preferentially took place on the topsets of underlying clinoforms and reef progradation being restricted by the slope angles of the underlying systems.

3. Significant lateral differences in the distribution and architecture of reef-rimmed carbonate platforms are documented between the north and the south of the study area. In the north, thick, massive platforms remained rather stationary in respect to their seaward termination, whereas the platforms of the south are generally thinner and more widely distributed across the shelf. Reef-rimmed platforms that formed after 15 Ma exhibit an internal northward thickening trend, probably related to the onset of a downward bending of the northern part of the Browse Basin.

4. Subsidence trends calculated using reef occurrences as palaeo-waterdepth indicators result in average subsidence rates of ca. 64 $\frac{m}{Ma}$ for the southern and ca. 125 $\frac{m}{Ma}$ for the northern study area. Due to the lower subsidence rates in the south, reef development there may have experienced periods of inhibiting conditions during eustatic changes more often, forcing frequent reef migration and resulting in thinner, more widespread reef development. In contrast, the generally high subsidence in the north likely damped the influence of eustatic variations, resulting in thicker, comparatively fixed reef systems.

5. Around 11.1 - 9.83 Ma, the main connected reef-rimmed platform belt was superseded by numerous isolated reefs, of which the youngest in the northernmost study area (Torosa) might have persisted until ca. 6.14 - 4.08 Ma. Yet, widespread reef development in the study area ceased around 6.14 Ma, which coincides with the onset of current-driven drift sedimentation. Modern reefs in the study area include the North Scott Reef and the Seringapatam Reef; their relation to the studied Miocene reef systems however remains unclear.

6. Additional controls on reef development, such as the possible influence of changing oceanic currents (i.e. change of the Indonesian Throughflow by closure of the SE Asian Gateway) on water temperatures, salinity and nutrients during the respective time interval require further investigation.

2.8 Acknowledgements

We thank Geoscience Australia for access to the 3D seismic data. The Department of Mines and Petroleum (DMP) of Western Australia is thanked for providing well data and reports through the database WAPIMS. We thank Volker Liebetrau (GEOMAR) for the Sr-isotope analyses. IHS is gratefully acknowledged for providing the KINGDOM software under an Academic User License Agreement. Schlumberger is acknowledged for providing the software Petrel. Conny Lutter is particularly thanked for her help in acquiring scientific literature. This study is a spin-off of project RE 2697/3-1 funded by the Deutsche Forschungsgemeinschaft (DFG). J. Belde is funded by DFG project BA 2136/4-1.

Chapter 3

3D seismic analysis of sediment-waves and related geomorphological features on a carbonate shelf exposed to large amplitude internal waves, Browse Basin region, Australia

The contents of this chapter were published in January 2015 in Sedimentology Volume 62, pages 87-109, by J. Belde, S. Back and L. Reuning of the EMR Geological Institute, RWTH Aachen University, Wüllnerstr. 2, 52062 Aachen, Germany.

3.1 Abstract

This study analyses the 3D geometry of sedimentary features recorded on the modern sea floor and in the shallow subsurface of a shelf to upper slope region offshore Australia that is characterized by a pronounced internal wave regime. The data interpreted comprise an extensive, >12,500 km^2 industrial 3D seismic-reflection survey that images the northern part of the Browse Basin, Australian North West Shelf. The most prominent seismic-morphological features on the modern sea floor are submarine terrace escarpments, fault-scarps, incised channels as well as restricted areas of seismic distortion interpreted as mass wasting deposits. Besides these kilometre-scale sea floor irregularities, smaller bedforms were discovered also, including a multitude of sediment waves with a lateral extent of several kilometres and heights up to 10 m. These sedimentological features generally occur in extensive fields in water depths below 250 m mostly at the foot of

submerged terraces, along the scarps of modern faults and along the shelf break between the outer shelf and the upper continental rise. Additional bedforms that characterize the more planar regions of the outer shelf are elongate, NW-SE-oriented furrows and ridges. The formation of both sediment waves and furrow-ridge systems requires flow velocities between 0.3 and 1.5 $\frac{m}{s}$, which could be generated by oceanic currents, gravity currents or internal waves. In the studied setting, these velocities can be best explained as being generated by bottom currents induced by internal waves, an interpretation that is discussed against oceanographic background data and modelling results. In addition to the documentation of 3D seismic-geomorphological features of the modern sea floor it was also possible to map kilometre-scale buried sediment wave fields in the seismic volume down to ca 500 ms two-way-time (TWT) below the present sea floor, indicating the general potential for the preservation of such bedforms in the sedimentary record.

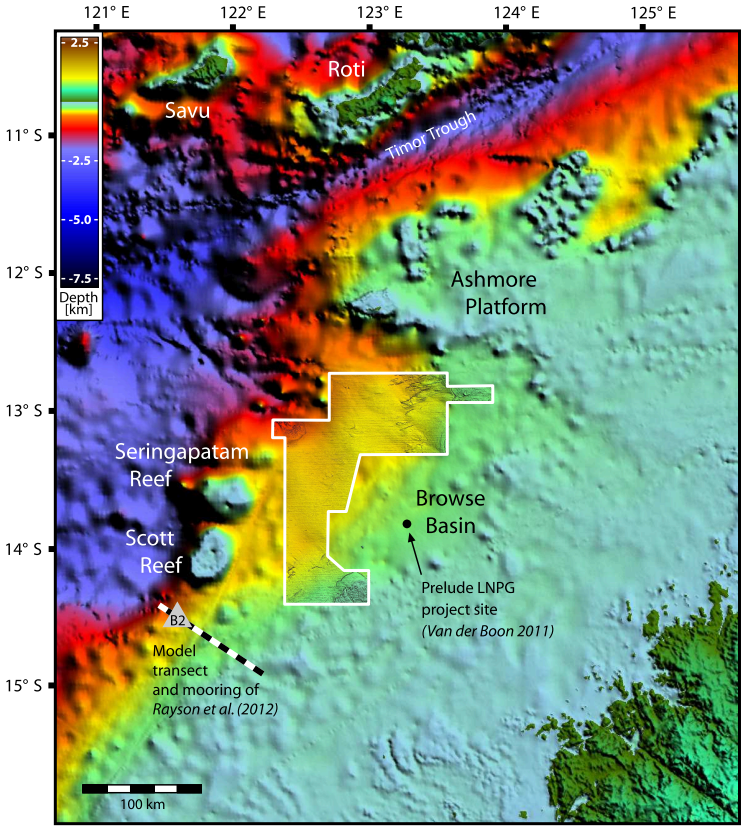

Figure 3.1: *Regional bathymetry of the North West Shelf of Australia. The sea floor topography of the seismic survey is coloured to represent water depth, accentuated by a gradient shader and superimposed on a GEBCO one-minute-resolution bathymetry grid. Seismic acquisition footprint oriented E-W. Annotations include important landmarks and the locations of measurements and model transects referenced.*

3.2 Introduction

Internal waves as a possible trigger for submarine sediment transport and accumulation have only recently become the focus of increasing attention and discussion (Pomar et al. 2012; Shanmugam 2013a; Pomar et al. 2013). Internal waves are gravity waves that oscillate along the interface between two fluid layers of different densities. On continental shelves and slopes they can be generated by the interaction of barotropic tidal currents with the bathymetry in well-stratified water bodies. The North West Shelf (NWS) of Australia is characterized by rapid bathymetric changes, a year-round stratification of the water column and strong tidal activity, a combination of factors that supports the generation of internal waves (e.g. Van Gastel et al. 2009). The internal waves and tides on the Australian NWS have been subject to previous research (e.g. Baines 1981; Holloway 1983a, 1984, 1987) supporting increasingly detailed computer models (e.g. Holloway 2001; Rayson et al. 2011, 2012). Internal solitary waves (solitons) with heights of up to 60 m have been reported in the direct vicinity of the 3D seismic study area presented in this paper (Wolanski and Deleersnijder 1998; Van der Boon 2011; Fig. 3.1). Such solitons can induce an intense increase in the near-bottom current speed which has in the past severely disrupted offshore oil and gas exploration and drilling (e.g. Kurup et al. 2011). The ubiquity and high amplitudes of internal waves along the Australian NWS make this region an ideal study site for analysing and discussing the influence of internal waves on the development of large-scale sedimentary structures and sea-bed morphology.

This study focuses on the shallow-subsurface seismic geomorphological and sedimentological analysis of an extensive, >12,500 km^2 3D seismic-reflection survey located in the northern Browse Basin of the Australian NWS (Fig. 3.1). The 3D seismic dataset images a modern sea floor characterized by a multitude of sedimentary-morphological features including marine terraces at various levels (Jones 1973) and large subaqueous sediment waves (Figs. 3.2 & 3.3). The latter are a common feature along the Australian margin in general (Heap and Harris 2008) and have been previously documented on the NWS by several authors (e.g. Jones 1971, 1973; James et al. 2004; Jones et al. 2009). For example, sediment waves were documented south of the study area on the central NWS, in water

depths of 70 to 90 m (James et al. 2004) and 98 to 118 m (Jones et al. 2009). These sediment waves were interpreted to be either shallow tidal structures, or caused by internal tides or stranded coastal structures (James et al. 2004), with the latter interpretation deemed unlikely by Jones et al. (2009). As the sediment waves analysed in this study all occur in water depths below 250 m, an influence of surface waves appears rather unlikely. This shifts the focus of the interpretation concerning their origin towards shelfal and deepwater bottom currents.

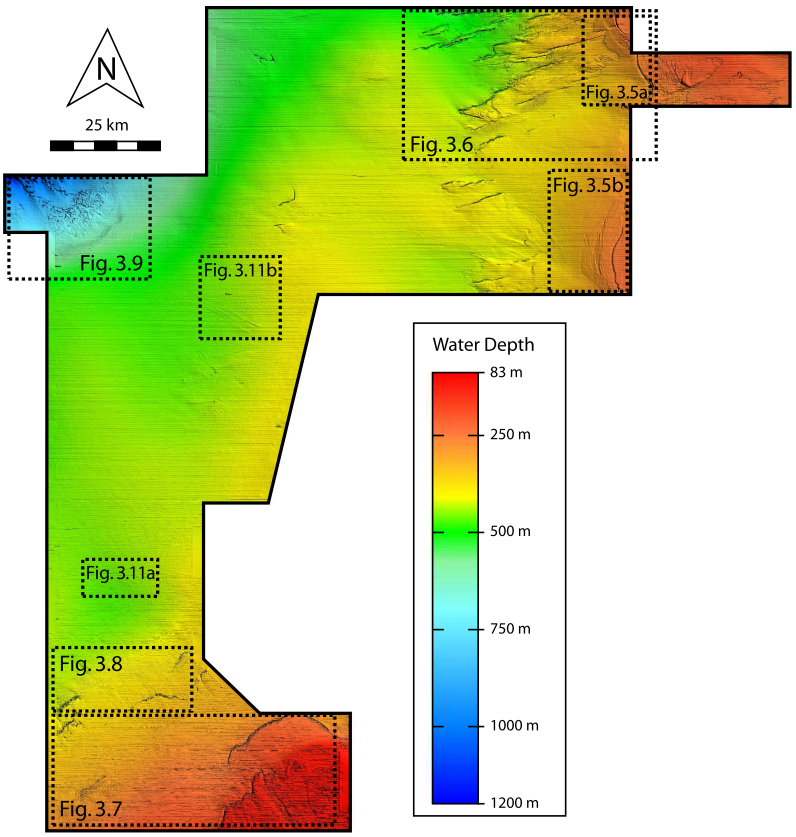

Figure 3.2: *Bathymetry of the study area. The visibility of sea floor features is enhanced by a gradient shader and the boxes indicate the position of the following figures. Seismic acquisition footprint oriented E-W.*

This paper makes use of the large scale of the available 3D seismic reflection data to: (i) document the lateral extent and the 3D seismic-reflection signature of sediment waves at surface level; (ii) image related seismic-geomorphological features such as furrows, mass-transport complexes and channels in a canyon head; (iii) discuss the relationship between the individual geomorphological features and the oceanographic environment; and finally (iv) depart from surface imaging and sea floor analysis into a 3D interpretation of the deeper seismic-reflection levels to study the potential preservation of such bedforms in the geological record.

3.3 Physical Setting

The Australian NWS forms the shallow-water part of the SW-NE trending West Australian continental margin (Fig. 3.1). Along most of its length it has a width of around 150 to 200 km (Jones 1973). The area under study is located between 12.5 and 14.5° S and 122 and 124° E in the Browse Basin, south of the Ashmore Platform and east of Seringapatam and Scott Reef (Fig. 3.1). This places the study area on the outer shelf to upper slope domain (sensu Baker et al. 2008) with water depths between at least 100 m in the southeast and 1200 m on the continental slope in the northwest (Fig. 3.2).

Immediately north of the study area, the Indonesian Throughflow (e.g. Condie and Andrewartha 2008; Schiller 2011) transports warm, low saline and oligotrophic water from the Pacific into the Indian Ocean (Gordon and Fine 1996), primarily through the Timor Straight (Fig. 3.1; Molcard et al. 1996; Gordon et al. 2010). The upper surface waters in the studied region are thought to be derived directly or indirectly by this current system. The Indonesian Throughflow induces a pressure gradient that results in the formation of the Leeuwin Current (Smith et al. 1991) in the vicinity of North West Cape (Godfrey and Ridgway 1985). The Leeuwin Current flows south along the west coast of Australia (Smith et al. 1991), being in part sourced by waters from the NWS (Holloway 1995). The Holloway Current, which is sourced by a recirculation of water from the Indonesian Throughflow, is a seasonal surface current that flows southward across the shallow shelf of the Browse Basin during winter (Condie et al. 2006). During the Northwest Monsoon season in summer the throughflow weakens, resulting in an anti-clockwise circulation and a net northward flow of surface waters across the shelf (Condie and Andrewartha 2008). Besides periodic cyclone-generated storm winds (Lourensz 1981; Porter-Smith et al. 2004), the wave regime of the NWS is characterized by low mean heights in conjunction with strong tides which have amplitudes of up to 10 m (Porter-Smith et al. 2004; Van Gastel et al. 2009). Throughout the year, the water column in the Browse Basin shows a pronounced density stratification, due to strong solar heating and low precipitation (Van Gastel et al. 2009).

The Australian NWS is an oceanic carbonate ramp similar in scale to the great Bahama Bank (James et al. 2004). Sedimentation offshore NW Australia has changed from a non-tropical ramp (Eocene to early Miocene) to a tropical, rimmed shelf (early to middle Miocene), and to a hemipelagic setting since the late Miocene (Apthorpe 1988; Rosleff-Soerensen et al. 2012). The sediment distribution across the shelf was compiled and analysed by several authors (e.g. Jones 1973; James et al. 2004; Dix et al. 2005; Collins 2011). The depositional environment is dominated by winnowing and the transport of sediment instead of its accumulation (Jones 1971, 1973; James et al. 2004). A variable facies distribution is documented by underwater photographs (Jones 1973) and sea bottom samples that show a "facies mosaic" of different particle types of different ages (James et al. 2004). Sediments are composed mainly of carbonates - 54% of the samples taken by Jones (1973) consisted of more than 90% carbonate and only slightly more than 1% of less than 60% - with minor terrigenous components playing a role chiefly on the inner shelf in regions affected by river discharge (Baker et al. 2008). Only a few of the lithological samples described by Jones (1973) or data points of the auSEABED database (Jenkins 2000) are positioned directly inside or in close proximity to the study area. The auSEABED (Jenkins 2000) data points in question show a considerable variation in grainsize distribution (Fig. 3.3A), both in the sense of data points differing among one another, but also in the sense of the data points themselves being comprised of highly variable samples. In addition, three box cores collected as part of the SO-185 cruise (Fig. 3.3A) show that the upper few metres of the modern sea floor consist of foraminiferal ooze containing a varying percentage of foraminiferal sand (Kuhnt et al. 2006). A number of industrial wells are located in the Caswell-Calliance area, but the lithological composition of the uppermost 300 m of sediment was not recorded. In summary, it is to be expected that the observations of Jones (1973) and James et al. (2004) also apply to the study area, although the available data is sparse.

3.4 Data and Methodology

The seismic data interpreted in this study comprise the post-stack time-migrated multichannel 3D seismic-reflection survey "North Browse TQ3D". This 3D seismic survey was acquired between October 1998 and June 1999 by Western Geco using dual source arrays of 8 airguns in flip-flop mode alternately releasing approximately 44,000 cm^3 (44 litres) of air at 140 bar. The seismic reflections were recorded by six 5200 m long streamers equipped with 9984 hydrophones each. The 3D data underwent standard processing steps including 3D multiple attenuation, DMO gathering and stacking, velocity analysis, static-tidal compensation, binning, migration, deconvolution, filtering to suppress minor wrap-around and random noise, a shift of the data to mean sea-level and amplitude scaling. The survey was zero-phased in SEG standard polarity ("American Polarity") and has a bin spacing of 18.75 m for inlines (E-W) and 12.5 m for crosslines (N-S), with a total vertical record length of 7 s TWT sampled at a rate of 4 ms. Directly on the modern sea floor the lateral resolution is defined by the inline and crossline spacing, whereas the approximate vertical seismic resolution is better than 10 m (sonic velocity of 1500 $\frac{m}{s}$ in water; upper frequency spectrum >50 Hz). The data contains E-W oriented seismic acquisition artefacts (e.g. Fig. 3.2).

3D seismic interpretation in this study started on reflectivity data in a top-to-bottom approach, defining the first prominent positive reflection as the modern sea floor and moving from this first interpretation level successively deeper into the subsurface. A second interpretation phase involved the generation and analysis of 3D seismic attributes (e.g. variance) on horizon slices or subcrops, i.e. extractions from seismic volumes at a constant time distance from an interpreted horizon (e.g. Back et al. 2006). In order to minimize the interpretation of subsurface multiple reflections of surface bedforms, the traced seed bathymetry and deeper horizon interpretations were generally smoothed before being used as subcrop. As the generated subcrop levels were not necessarily parallel to the underlying strata, relevant reflectors in the surrounding area were mapped once a promising structure was found. This helped to obtain a clearer image and to counter the possibility of misinterpreting intersected layers or similar artefacts as sediment waves. Due to the number of artefacts along the survey acquisition-direction (E-W; see Fig. 3.2)

and general concerns over the restrictions by resolution, only bedforms that could be discerned from their surroundings with reasonable certainty were further investigated. Since a positive relationship between the bedform height and its variance signature could be observed, this was interpreted to be a useful indicator of bedform state; i.e. a strong variance signature indicated larger bedforms or a good preservation, whereas smaller or less preserved bedforms showed a generally weaker variance. A first-pass depth conversion of the sea floor reflector was performed by assuming a constant sonic velocity of 1,500 $\frac{m}{s}$ over the water column, to allow for the generation of contour lines and the approximation of slope angles.

3.5 Results

The sea floor in the study area is subdivided into four zones (Fig. 3.3A) based on the following seismic-geomorphological characteristics: Zone 1, comprising both the far northeast and the far southeast of the survey area, is defined by several pronounced morphological steps at variable depth levels (Fig. 3.2). As Jones (1973) described segments of various marine terraces to occur along the entire NWS, determining palaeo-strandline erosion as their most likely origin, the observed morphological steps are interpreted to represent terrace escarpments. In the northeast of the study area, the observed morphological steps in the sea floor (Figs. 3.3A & 3.4) can be assigned to two individual water-depth intervals of 245 to 260 and 260 to 280 m. The inferred terraces in the far southeast of the study area (Fig. 3.3A) occur in water depths of 130 to 140 and 235 to 245 m, with additional linear features preserved at depths of up to 375 m (Figs. 3.2 & 3.3A). These deeper-water terrace-like features are less characteristic in their morphological appearance in comparison to their shallow-water counterparts, and in places oblique to the local bathymetric trend. The respective heights of the terrace escarpments in the northeast are between ca 10 and 25 m and in the southeast between 40 and 60 m, indicating a northwards decreasing escarpment height with increasing water depth. The south-eastern terraces probably correlate with the terrace features documented by Jones (1973) that trend in a NE-SW orientation near Scott Reef at 145 and 190 m water depth, respectively.

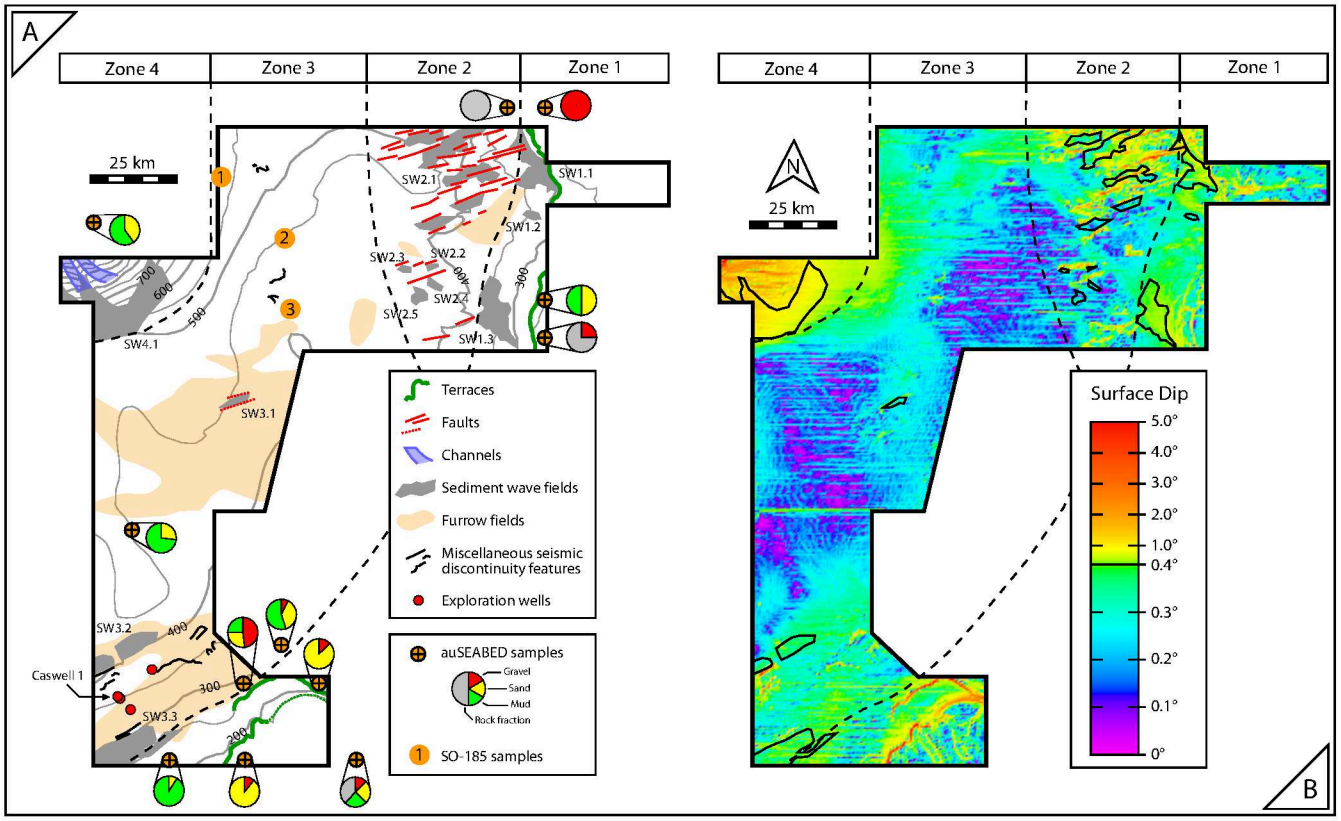

Figure 3.3: *(A) Map of the sea floor topography and geomorphological features, based on which the study area can be sub-divided into four zones. Zone 1: submerged terraces (green); Zone 2: major faults offsetting the sea floor (red); Zone 3: relatively flat topography and longitudinal furrows (light orange); Zone 4: submarine channels within a canyon head (blue). Sediment wave fields (grey) and miscellaneous seismic discontinuity features (black) occur in all zones. The contour lines are labelled in metres water depth. Exploration wells are marked by red dots and the location of well Caswell 1 is labelled. The orange circles indicate the centre of auSEABED sample grid cells close to the survey area for which lithological data was available. Adjacent pie charts show the mean grainsize distributions. The numbered orange circles indicate the position of gravity corer sites (1: 18488-5; 2: 18489-2; 3: 18490-2) of the SO-185 cruise (Kuhnt et al. 2006). (B) Map of the surface dip in the study area. The dip values are averaged over a 500x500 m grid to minimize the footprint of seismic acquisition artefacts.*

Zone 2 is a triangle-shaped area of ca 3100 km^2 extent in the northeast of the studied 3D seismic survey (Fig. 3.3A). This zone is located in a water depth between 350 and 530 m and is characterized by the occurrence of numerous ENE to WSW oriented linear seismic-reflection discontinuities (Fig. 3.2) interpreted as faults. Deeper-seated faults occur also further southwest in the study area, however almost none of these structures reach the sea floor. All faults of Zone 2 are extensional, forming pronounced horst and graben systems with an ENE-WSW orientation (Fig. 3.3A).

Zone 3 is located further basinward covering an area of approximately 8200 km^2. This zone defines a rather flat region on the outer shelf in water depths between 350 and 550 m exhibiting generally low slope angles rarely exceeding 0.3° (Fig. 3.3B). Characteristic seismic-geomorphological features on the sea floor are extensive fields of NW-SE to NNW-SSE oriented longitudinal ridges and furrows that differ from sediment waves by a lower relief, a smaller width and a closer spacing.

Zone 4 finally defines the transition between the outer shelf and the upper continental slope in the study area (Fig. 3.3), which is only covered by seismic-reflection data in the far northwest of the 3D seismic survey. This zone, which is situated at a submarine canyon head (Fig. 3.1), is characterized by a distinct steepening of the slope from gradients of around 0.3° in the southeast to gradients of ca 4° in the northwest, and a basinward increase in water depth from 500 to 1200 m (Fig. 3.3). Characteristic seismic-geomorphological sea floor features of Zone 4 are two submarine channels incised into the continental slope (Figs. 3.2 & 3.3). In their headwall region, pronounced seismic-reflection discontinuities suggest the presence of gravity-driven downslope mass movement.

The following paragraphs describe the 3D seismic-geomorphological sea floor features of the study area in detail, including: (a) sediment waves on the sea floor; (b) sea floor furrows and ridges; and (c) buried seismic-sedimentological features interpreted as palaeo-sedimentwaves, as well as signatures indicative of palaeo-furrows or palaeo-ridges.

3.5.1 Sediment waves on the sea floor

On the modern sea floor, several fields of parallel to subparallel, linear to undulating bedforms occur (Fig. 3.3A). The areas marked by these bedforms range in size from 1 to 220 km^2, and mainly comprise NNE-SSW oriented ridge-trough associations. Depending on the location, the lateral extent of the bedforms within their respective field ranges between 0.4 and 12 km, with a spacing (wavelength, measured from ridge crest to crest) commonly between 120 and 400 m. Due to the constraints of the vertical resolution of the 3D seismic-reflection data, an accurate, metre-precise measurement of the bedform height is difficult, but its maximum can be estimated at 10 m in slope settings (Zone 4) and around 5 m in the remaining shelf areas (Zones 1 through 3). Due to their spatial arrangement, shape and size, the observed bedforms can be classified after Wynn et al. (2000) as sediment waves. The location of the observed sediment-wave fields in the study area is shown in figure 3.3A; an overview of the common seismic-geomorphological characteristics of these features is provided by Table 3.1.

Table 3.1: Overview of the seismic-geomorphological characteristics of the modern sediment-wave fields analysed in this study (bsl: below sea-level).

Zone	Name	Max. variance signature strength	Field size [km^2]	Spacing [m]	Relative sediment wave orientation to local isolines	Approximate depth [m bsl]
1	SW1.1	strong	72	150	parallel to slightly oblique [S] normal to oblique (45°) [N]	280-330
	SW1.2	weak	3.5	160-200	parallel	340-350
	SW1.3	intermediate	92	130-170	parallel to slightly oblique	300-390
2	SW2.1	strong	175	160-250	approx. parallel, normal [S] (approx. 45° to faults)	340-510
	SW2.2	weak	1.0	160-170	-	400-410
	SW2.3	weak	2.3	120-130	-	400-405
	SW2.4	weak	3.2	180-200	-	395-400
	SW2.5	intermediate	9.2	180-220	-	405-410
3	SW3.1	weak	8.5	120-160	approx. parallel	430-450
	SW3.2	weak	39.5	200-300	approx. 45°	400-425
	SW3.3	intermediate	80	150-200	approx. 45° [N], approx. parallel [SE]	250-300
4	SW4.1	strong	220	150-350	oblique (<45°)	500-1000

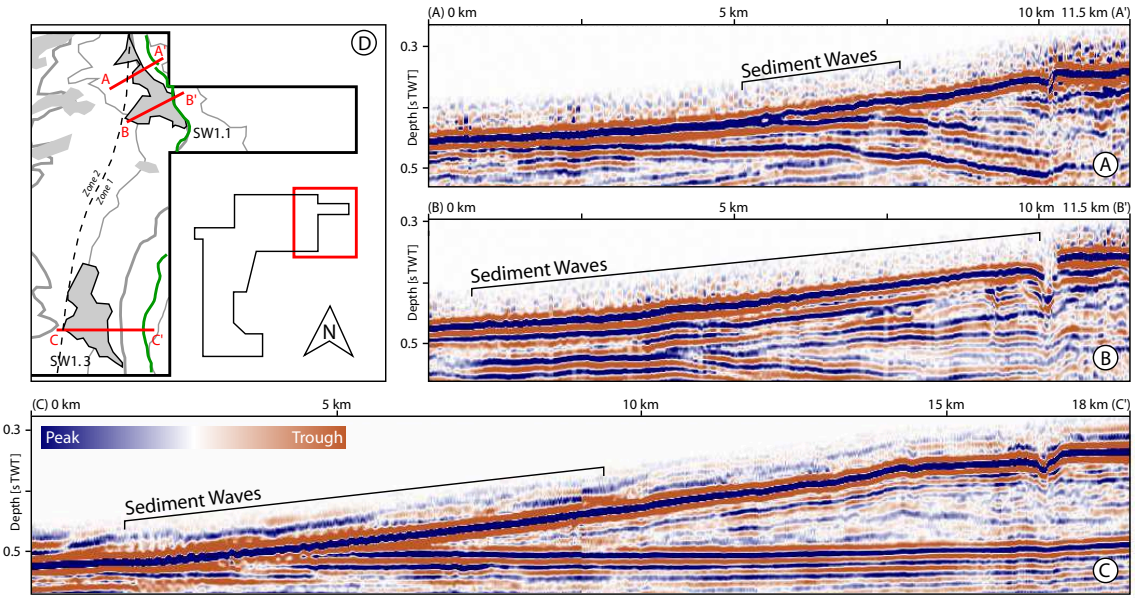

Figure 3.4: *Vertical seismic-reflection profiles across drowned terraces illustrating the positions of sediment wave fields SW1.1 (Fig. 3.5A) and SW1.3 (Fig. 3.5B). Polarity of the seismic data is shown in C (SEG standard).*

Three sediment-wave fields occur on the seaward side of the mapped terraces within Zone 1, in the northeast of the survey (Fig. 3.3A). The subsurface of the two largest fields is imaged by vertical sections of reflectivity data in figure 3.4, documenting that the terrace escarpment lies in the upper part of a subsurface sediment wedge that terminates 10 to 15 km basinward near the boundary to Zone 2. Figure 3.5A shows a seismic variance display of the 72 km^2 large sediment-wave field SW1.1, which is located on the sea floor in water depths between 280 to 330 m. The observed variation in distance of the sediment waves to the adjacent terrace is apparently not related to the escarpment height, but seems to reflect differences in the sea floor angle (Fig. 3.5A). Areas covered by sediment waves are characterized by average sea floor dips between 0.55 and 0.63°, whereas the blank, featureless areas neighbouring the terrace escarpment in the northeast of the survey exhibit higher average slope angles between 0.68 and 1.0°. The gradual disappearance of sediment waves in the west and southwest of the field correlate with the thinning out of the underlying sedimentary wedge and the associated decrease in slope to 0.2 to 0.3° (Figs. 3.4A,B & 3.5A). Internally, the south of sediment-wave field SW1.1 exhibits sediment waves that are parallel to slightly oblique to the terrace escarpment and preserved in its immediate vicinity. The variance signature of these sediment waves is intermediate to strong (Fig. 3.5A). Further north, the most proximal (landward) sedi-

ment waves are located ca 1.3 to 2.6 km west of the terrace and are oriented oblique to perpendicular in respect to the escarpment, displaying strong variance signatures (Fig. 3.5A). The wavelengths of the sediment waves in field SW1.1 average about 150 m.

Sediment-wave field SW1.3 is located south of the field SW1.1 and has developed in a similar setting, being positioned 3 to 7 km basinward of a drowned terrace escarpment (Fig. 3.5B). Field SW1.3 extends over 92 km^2 in a water depth of 300 to 390 m. In between the sediment-wave field and the terrace lies a crescent-shaped area that is characterized by arcuate reflection discontinuities, suggesting near-surface soft-sediment creep (e.g. Wynn and Stow 2002) or minor gravity gliding. As with sediment-wave field SW1.1, the extent of the more southern sediment waves is tied to the termination of the subsurface sediment wedge (Fig. 3.4C) and possibly controlled by its slope. Here, sediment waves occur in regions with an average sea floor dip between 0.39 and 0.56°, with the most prominent being observed in areas with a dip of around 0.44°. Sediment waves are lacking in areas directly adjacent to the drowned terrace level and immediately northwest of the terrace escarpment, although these areas show a similar range of dips (Fig. 3.5B). To the north an area adjoins, where the sea floor has a rather crinkled appearance, which may be a result of imaging sediment waves smaller than the vertical resolution or simply a large-scale roughness of the sea floor. Sediment-wave field SW1.3 terminates in the west in areas with a sea floor dip of 0.26° and below. The crest orientation of the sediment waves is parallel to slightly oblique to the local bathymetric contours and to those of the drowned terrace. The spacing of the waves in areas with a weak variance lies between 130 to 140 m, and increases to 170 m in regions of intermediate variance (Fig. 3.5B).

Figure 3.6 provides an overview of the typical distribution of sediment-wave fields in Zone 2, where most sediment waves occur in fault-controlled morphological lows. The individual sediment-wave fields shown in figure 3.6, summarized under the designation SW2.1, together extend over an area of approximately 175 km^2 and are located in water depths between 340 and 510 m. Variance signatures of the sediment waves are generally strong but fade out towards the west and southwest of the study area. The observed bedforms are mostly straight-crested in the north but exhibit an increasing sinuosity further south, which becomes especially pronounced in the southernmost fields that are not so

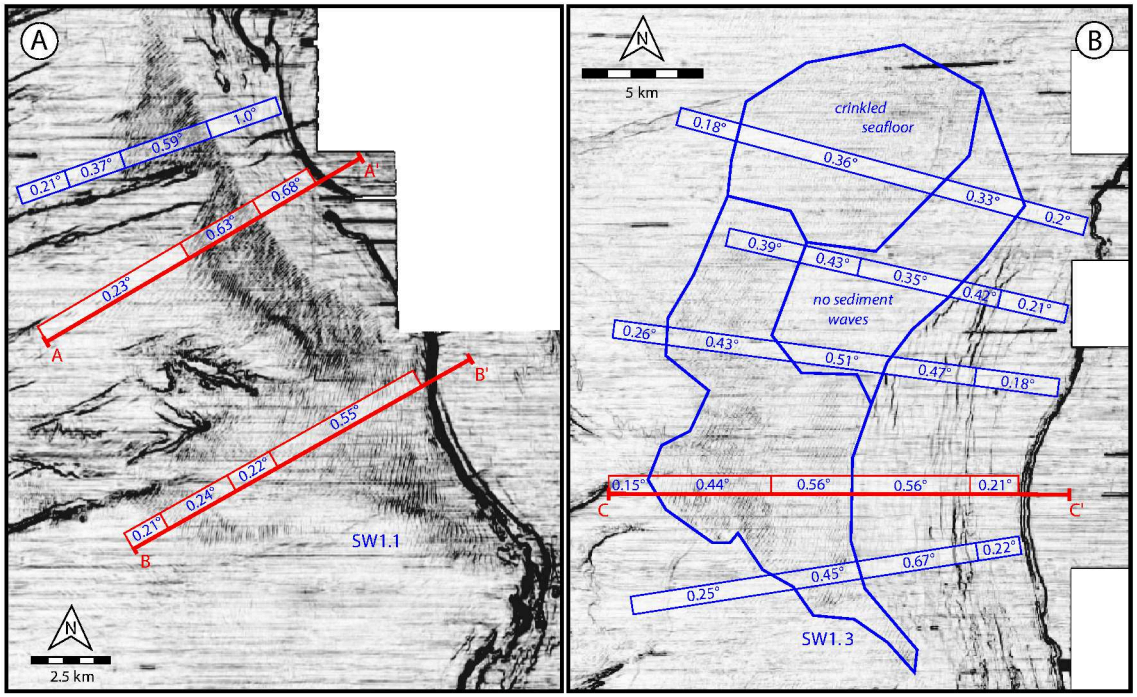

Figure 3.5: *(A) Sediment wave field SW1.1 shown on a variance map of the sea floor that highlights variations in the seismic amplitude of adjoining data points. Regions of reflection continuity are shown in lighter colour, areas of pronounced reflection discontinuity (e.g. faults, scarps) are shown in darker tones. Slope-angle measurements are indicated in blue suggesting a correlation between the slope angle and areas of sediment waves (i.e. sediment waves appear to form where the slope angle lies within a certain range). The positions of the sections shown in figure 3.4A and B are marked in red. (B) Variance map of sediment wave field SW1.3. Slope-angle measurements are indicated in blue, showing an existent but apparently less reliable correlation between the slope angle and areas of sediment waves. The position of the profile shown in figure 3.4C is marked in red. Seismic acquisition footprint oriented E-W.*

narrowly framed by faults. In these fields, the sediment waves also often exhibit bifurcation of the crests, a geometry that is otherwise rare within the study area. The contour inset in figure 3.6 documents that the crests of many sediment waves trend approximately parallel to the local isolines and at an average angle of ca 45° to the observed faults. The wavelength of the sediment waves varies between 160 and 250 m, and bedform heights of up to 5 m can be observed.

Zone 3 exhibits three sediment-wave fields (Fig. 3.3A), one small field in the central part of the study area (SW3.1) and two larger fields (SW3.3 and SW3.2), located in the south of the survey region. Sediment-wave field SW3.1 extends over 8.5 km^2 in 430 to 450 m deep water, comprising almost N-S oriented waves that occur between two ENE-WSW

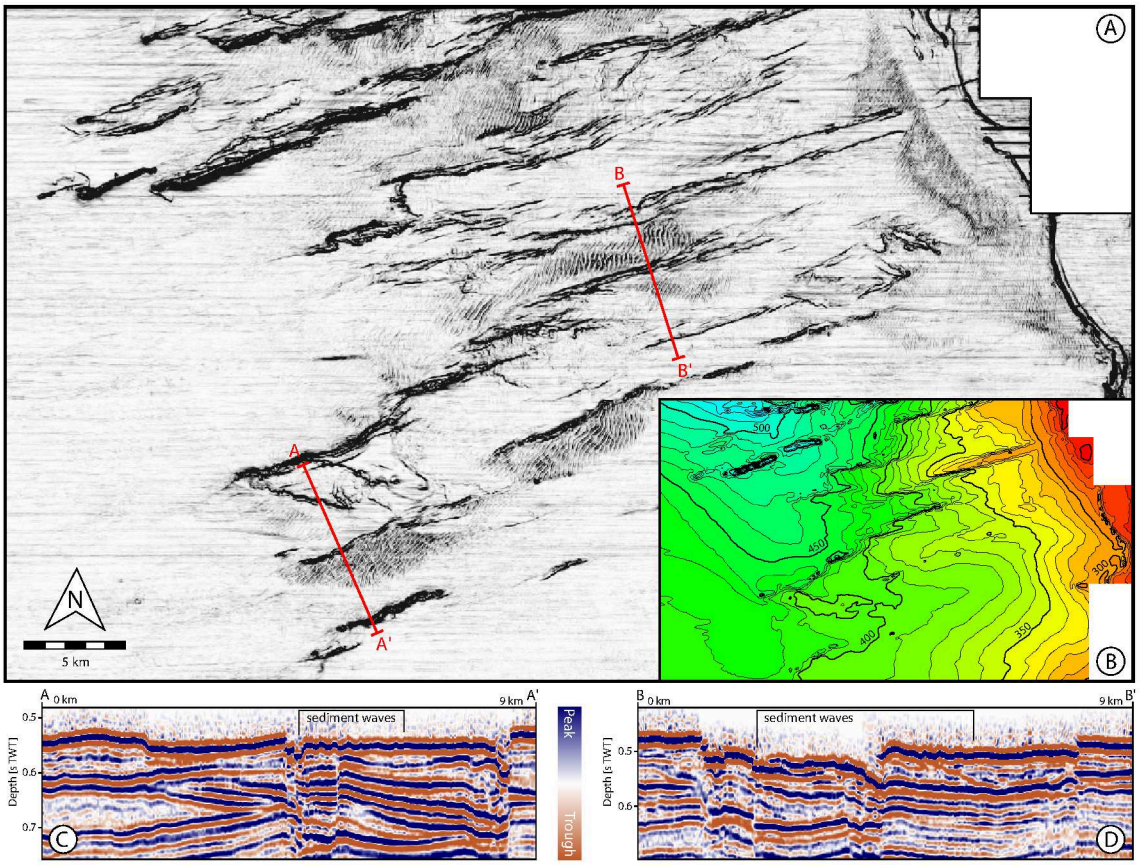

Figure 3.6: *(A) Variance map of fault controlled sediment wave field SW2.1. The seismic sections A and B are shown in inset C and D respectively. Seismic acquisition footprint oriented E-W. (B) Bathymetry map of the region (isolines labelled in metres water depth). (C-D) Seismic reflectivity sections further illustrating the position of the sediment wave fields as occurring in relative topographic lows.*

oriented faults. Sediment-wave field SW3.3 is located upslope of a set of parallel, linear, high-amplitude seismic-reflection discontinuities and downslope to the west of two submerged terrace escarpments (Fig. 3.7). The wave field covers an area of approximately 80 km^2 in water depths of 250 to 300 m, with a main wave area in the southwest and an almost linear, NE-SW-trending outlier in the east that follows the 250 m sea floor contour. The seismic variance signature of the observed sediment waves in field SW3.3 is intermediate, and most of the wave crests are strongly sinuous and oriented at 45° to the local isolines (Fig. 3.7). A slightly different pattern characterizes the north-eastern part of the outlier field, where the wave crests are only slightly sinuous and in places parallel to local isolines. The average wavelength of the sediment waves in field SW3.3 lies between 150 and 200 m.

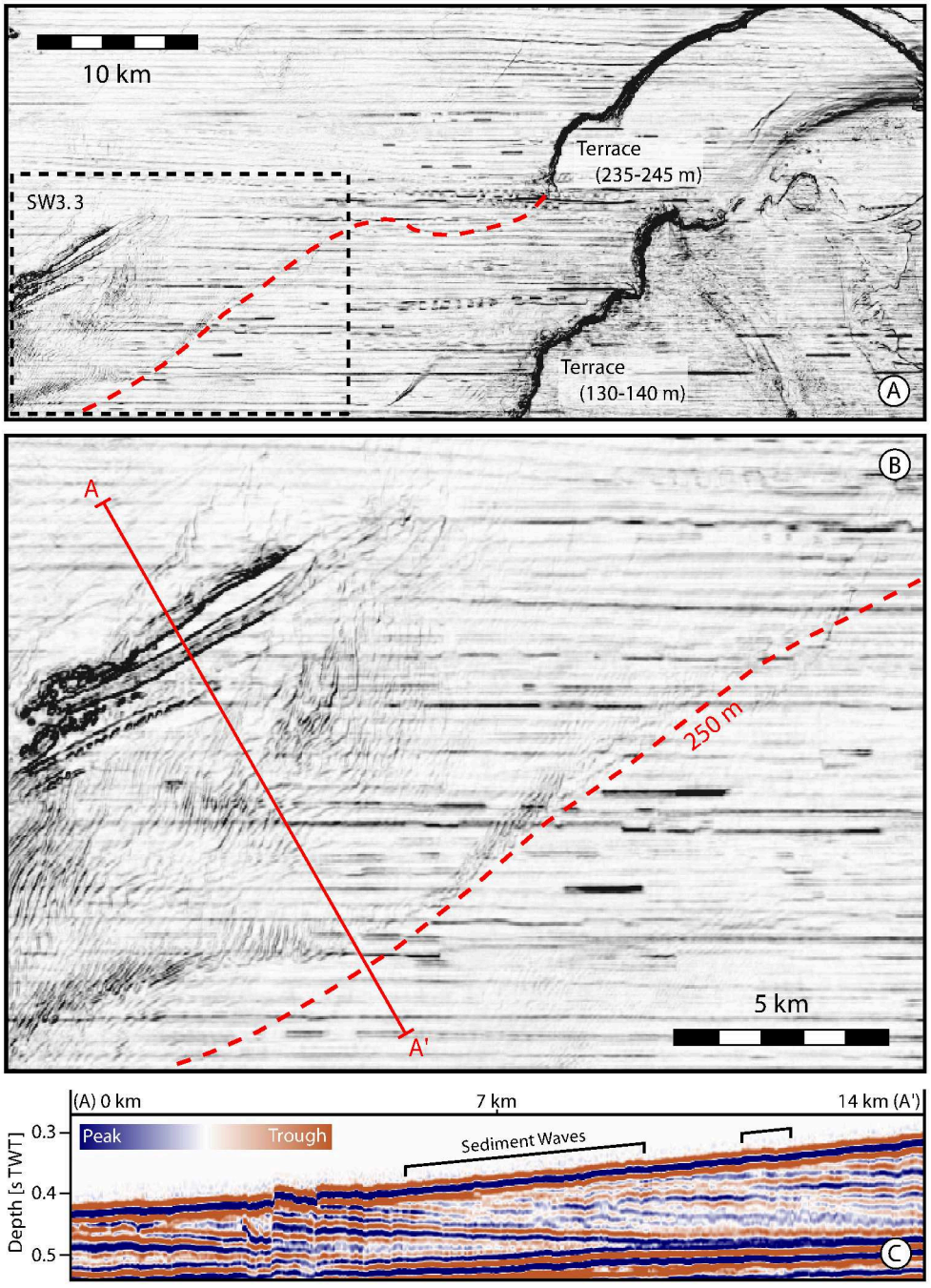

Figure 3.7: *(A) Variance map showing the sediment wave field SW3.3 located west of submerged terraces (depth values correspond to terrace tops). Seismic acquisition footprint oriented E-W. (B) Close-up showing sediment wave field SW3.3 positioned upslope of an unidentified sea floor disturbance and downslope of the 250 m water depth isoline (indicated in red). The NE-SW-trending outlier of the sediment wave field extends along this extension of the lower terrace. (C) Section showing sea floor disturbance and position of sediment waves. The visible undulations of reflectors are primarily caused by E-W running acquisition artefacts. Polarity of the seismic data is shown in the upper left (SEG standard).*

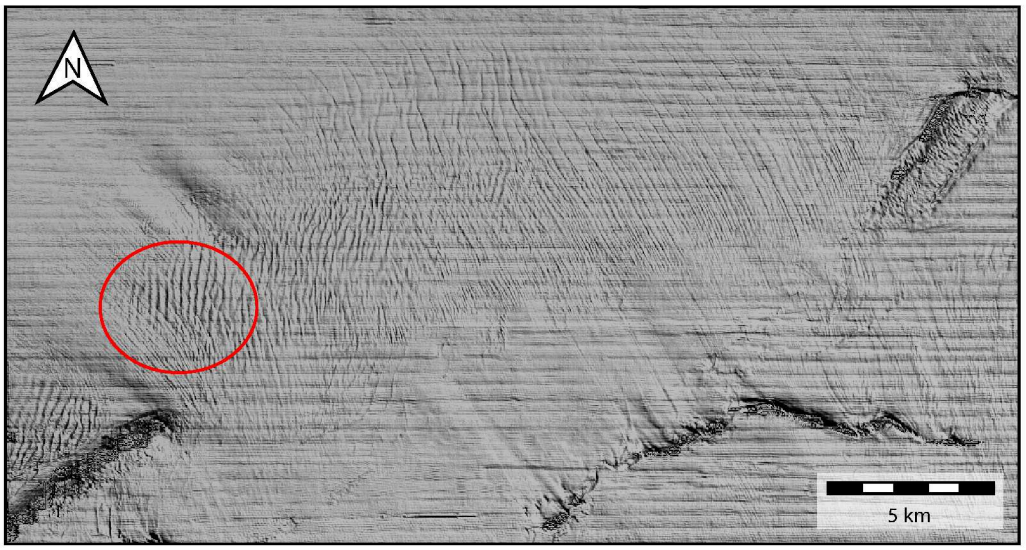

Figure 3.8: *Gradient shaded bathymetry showing sediment wave field SW3.2 surrounded by longitudinal furrows displaying varying degrees of curvature. Visible superposition of longitudinal furrows (mainly NNW-SSE oriented) on sediment waves (mainly NNE-SSW oriented) is indicated by the red circle. Seismic acquisition footprint oriented E-W.*

The third sediment-wave field within Zone 3 is field SW3.2 (Fig. 3.8), which lies downslope of several high-amplitude seismic-reflection discontinuities. The field has a size of 39.5 km^2 and is positioned in water depths of 400 to 425 m. It appears to contain sediment waves that are oriented NNE-SSW and obliquely at a 45° angle to the local isolines, have relatively straight crests and are spaced 200 to 300 m apart. The exact geometry of the bedforms in this field is difficult to analyse however, due to the co-occurrence of NNW-SSE oriented ridges or furrows along with the sediment waves.

Zone 4, the most basinward zone, contains the sediment-wave field SW4.1, which is located on the beginning of the continental slope in water depths between 500 to 1000 metres and covers an area of ca. 220 km^2 (Fig. 3.9). This sediment-wave field is dominantly located basinward of an increase in the sea floor slope from approximately 0.3 to 0.9° (Figs. 3.9 & 3.10). It is limited downslope by prominent seismic reflection disturbances, most likely related to gravity-driven mass-movement and channelling within the region of the canyon head. Whereas the sediment waves on the top of the fill of channel A are continuous with the rest of the field, displaying the same linear crests, those occurring on the fill of channel B are isolated by the possible mass-transport deposit and show a slight upslope convex crest curvature. The overall variance signature of the sediment-wave

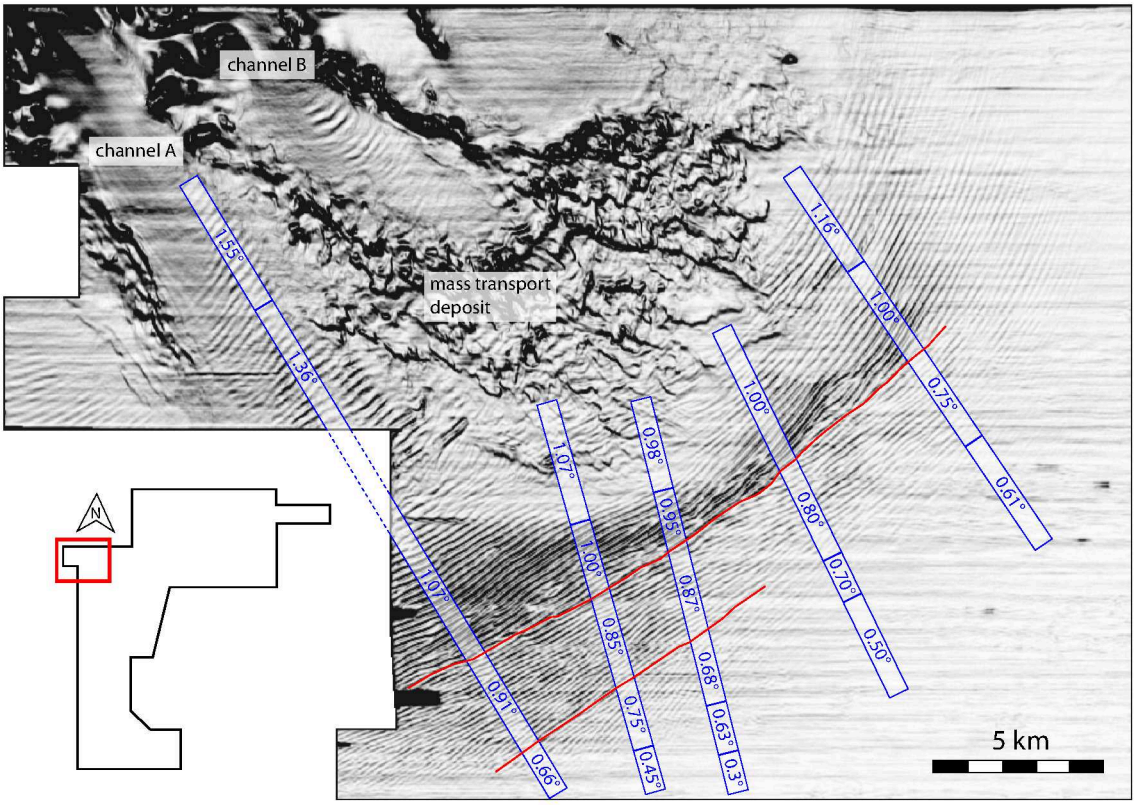

Figure 3.9: *Variance map of sediment wave field SW4.1. Slope angles were measured along the profiles shown in blue, showing a good correlation between the slope angle and the upslope boundaries of the sediment wave field (i.e. sediment waves appear to form where the slope angle exceeds a critical value). The slope angle also appears to play a role in the strength of the variance signature, i.e. the size of the sediment waves (Fig. 3.10A, D), and slight changes in their crest orientation (indicated by the red lines). Seismic acquisition footprint oriented E-W.*

field SW4.1 is strong, generally decreasing in a landward direction and vanishing below slope angles of 0.5 to 0.6°. Along the southern slope margin of field SW4.1 most wave crests are oriented parallel to the local bathymetric contours, which changes in channel A (ca. 45° angle to the local bathymetry) and on the eastern slope margin (ca. 25°). Bifurcations of the sediment waves are rare, except in areas where the crest orientation and variance strength changes (Fig. 3.9). These locations correlate with changes in slope angle of 0.1 to 0.25°. The spacing of the sediment waves observed in field SW4.1 increases with distance from the shelf-slope transition and with steepening of the slope angle, rising from approximately 150 m in the south-eastern fringes of the field, to 200 m in the central regions, up to 300 to 350 m in the downslope channel areas (Fig. 3.9). The maximum bedform heights of up to 10 m however occur in the central upslope areas at slope angles between 0.9 and 1.0° (Figs. 3.9 & 3.10A, D).

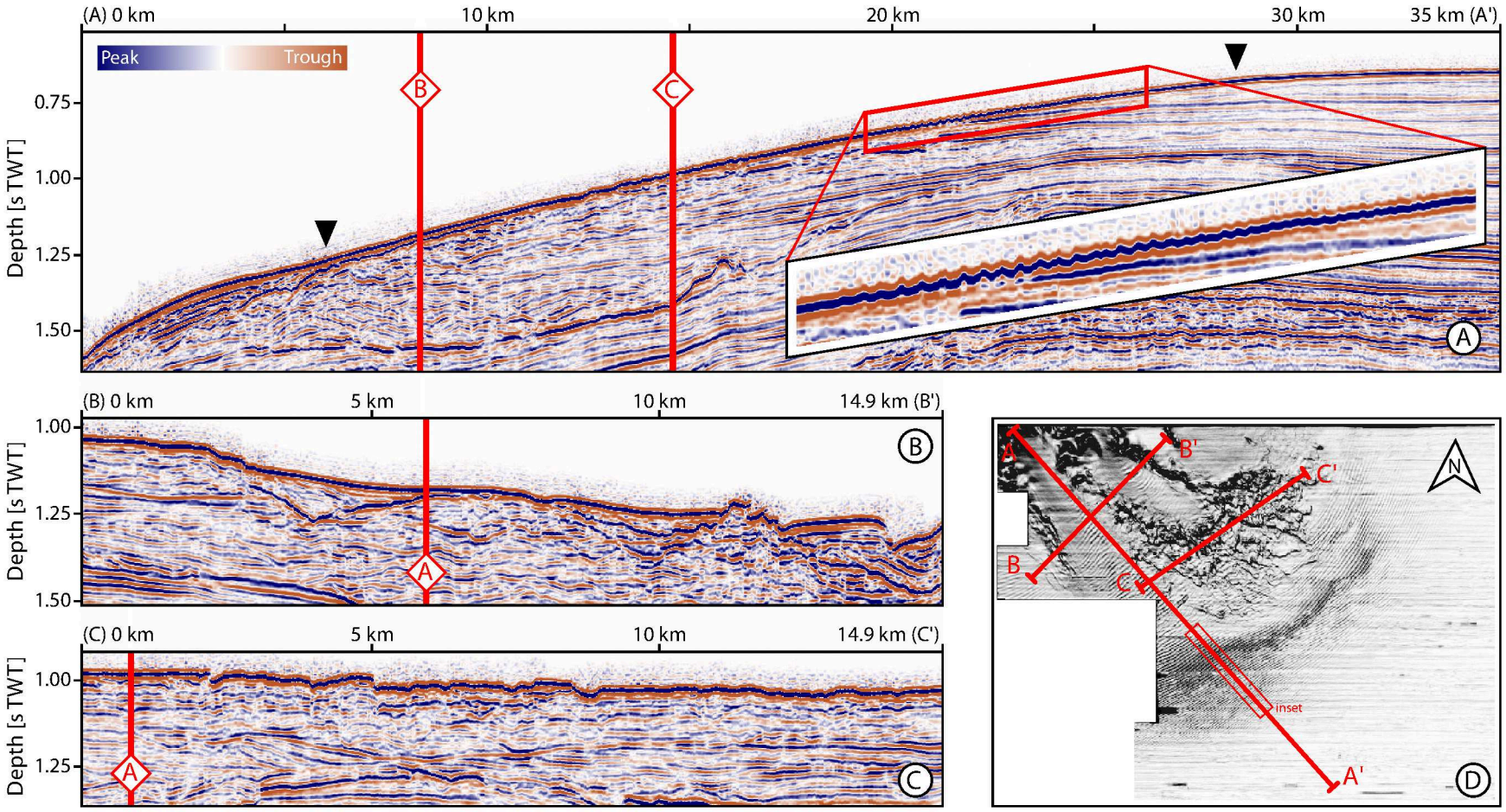

Figure 3.10: *Seismic reflectivity sections showing the subsurface beneath the sediment wave field SW4.1. (A) Seismic reflectivity section oriented along one of the channels of the canyon head. The black triangles indicate the upper and lower bounds of the sediment wave field, illustrating that the sediment waves are located basinward of a notable increase in slope angle. The inset shows a close-up of the pattern of sediment waves on the topmost seismic reflector. (B) Seismic reflectivity section positioned perpendicular to the channels. (C) Seismic reflectivity section across the area interpreted as possible mass transport deposits, showing minor faulting within the upper 0.1 s TWT. (D) Overview map (variance attribute) of the position and orientations of the sections shown.*

3.5.2 Furrows and ridges

In addition to sediment waves, the sea floor of the study area is also marked by fields of linear, elongate bedforms, which differ from sediment waves by displaying lower relief, smaller width, closer spacing and relatively constant orientation. These ridges or furrows occur mainly in Zone 3, with some overlap into Zone 2 in the northeast of the study area (Fig. 3.3A). In the studied dataset these bedforms vary between a NW-SE to NNW-SSE orientation in most cases. The local bathymetric contours appear to exert only a minor influence, with the ridge and furrow bedforms in the south dominantly normal, in other regions often oblique and in very rare cases even parallel to the local bathymetric trend. Due to the low relief, interference from E-W running acquisition artefacts and resolution constraints, a distinction between ridge and furrow is usually not possible. Given these circumstances, the height differences can only be estimated to lie below 1 m and the spacing between 50 and 250 m. The furrows superimposed on sediment wave field SW3.2 (see above), are an exception in this respect and part of a prominent furrow field, located in the south of the study area, enclosing sediment-wave field SW3.2 and extending further east (Figs. 3.3A & 3.8). These more prominent furrows can be observed over an area of approximately 190 km^2 in water depths between 380 and 440 m, with an orientation normal to the local isolines. Some of these furrows appear to have formed within the sediment waves of field SW3.2, with furrow superposition documented by the dissection of sediment waves occurring in the southwest of the furrow field (Fig. 3.8).

A second type of elongate bedform can be observed in two instances, located in the central and southern part of Zone 3 (Fig. 3.3). In these areas, NW-SE oriented low relief ridges occur. These differ from the previously described features by being broader, having a more pronounced relief and having a wider lateral spacing of 125 to 400 m (Fig. 3.11). The most distinguishing characteristic however is that the individual features are not parallel. This is evidenced by ridges terminating against each other, both in upslope and downslope directions at angles of 5 to 10° (Fig. 3.11).

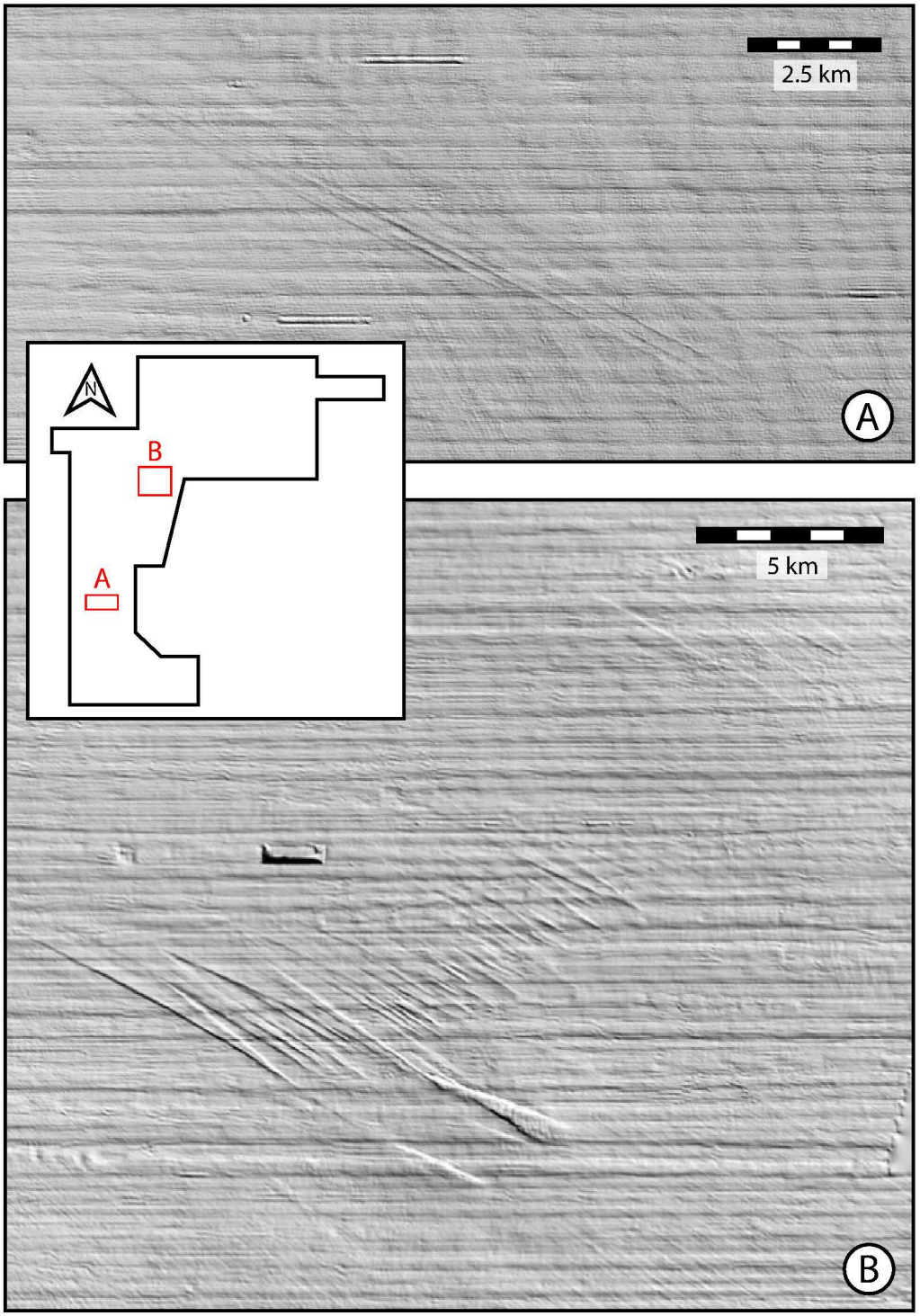

Figure 3.11: *Gradient shaded bathymetry showing longitudinal ridges. In contrast to the furrows observed in the study area, the ridges are not oriented parallel to each other and taper in both up-slope and down-slope direction. Seismic acquisition footprint oriented E-W.*

3.5.3 Buried seismic-sedimentological features

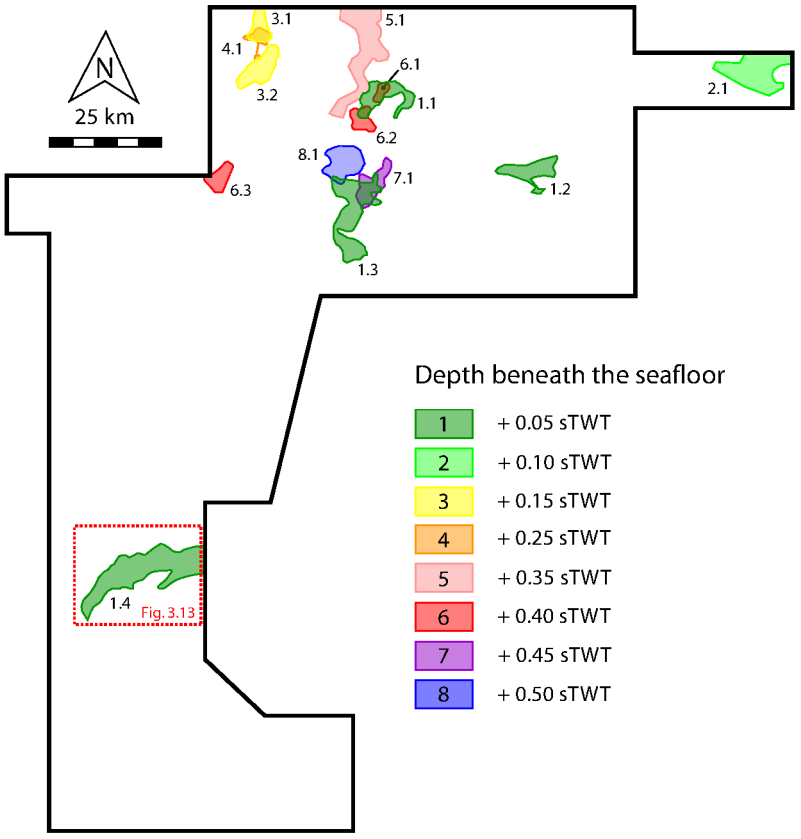

Figure 3.12: *Map showing the location and depth beneath the sea floor of buried sediment-wave fields in the study area.*

By using the subcropping technique on the 3D seismic variance data sampling the most recent sediments of the study area at steps of 50 ms (TWT), it was possible to identify several seismic-sedimentological features (Fig. 3.12; Table 3.2) down to depths of 500 ms (TWT) beneath the modern sea floor. This respective sedimentary package lies above the Messinian reflector of Struckmeyer et al. (1998), thus constraining the age of the contained structures to the post-Messinian. The therein identified features include buried sediment-wave fields and NW-SE oriented lineations (Fig. 3.13). The seismic-reflection signature of the buried sedimentary features is, due to the resolution deterioration with depth, generally less distinct than that of similar-sized sea floor features. This deterioration of resolution with depth may be partly responsible for the fact that only a few small sized sediment-wave fields (<20 km^2) were observed. Among the individual fields the sediment wave crest orientation ranges from NNW-SSE to NNE-SSW, with the majority being N-S oriented. The spacing of the buried sediment waves in the study area

is 75 to 450 m, quite similar to that observed on the sea floor, whereas the estimation of the height of individual wave features is rather difficult, due to the limited vertical resolution and possible near surface compaction effects. The observed lineations (Fig. 3.13) are interpreted to be preserved relicts of erosional features similar to the longitudinal furrows and ridges observed on the sea floor, due to their similarity in appearance and orientation.

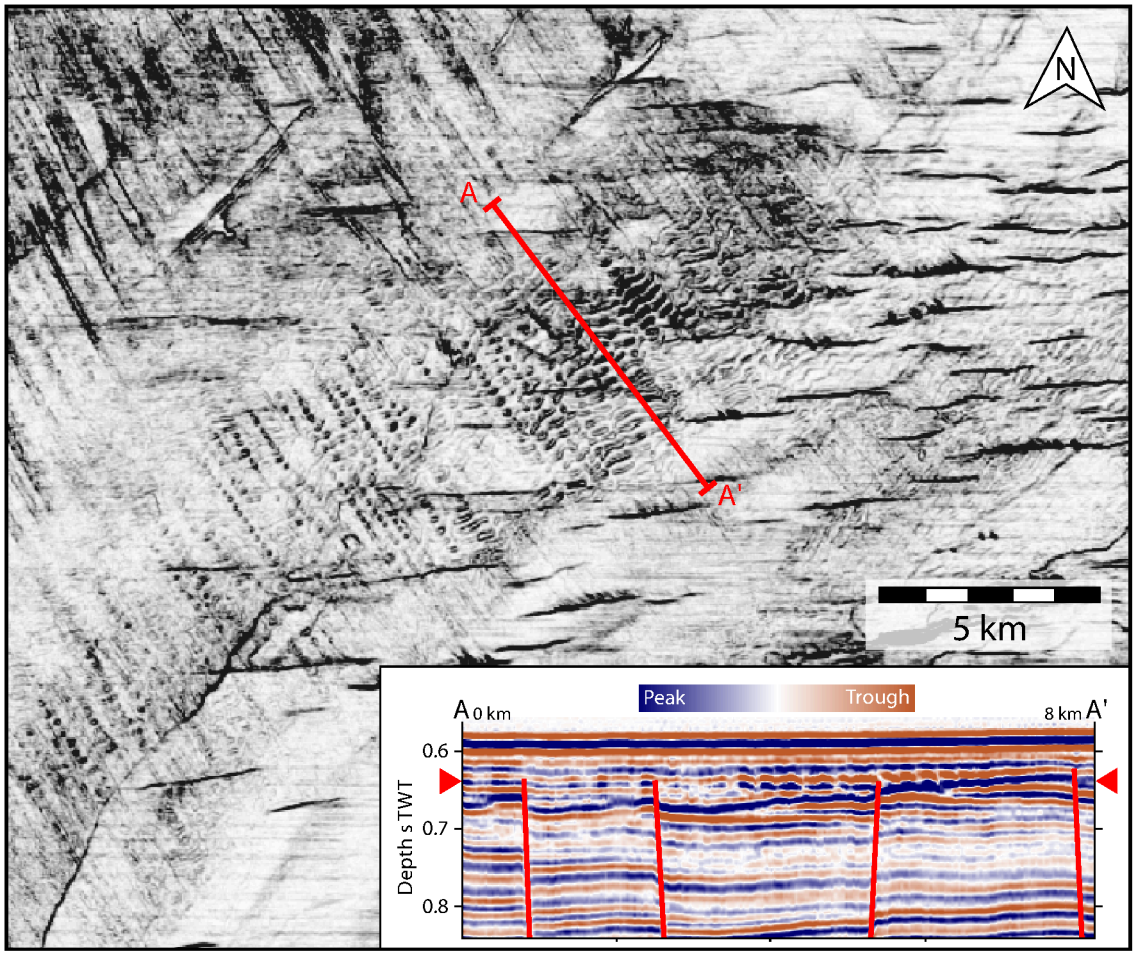

Figure 3.13: *Variance map showing the buried sediment wave field PSW1.4 on a sea floor-horizon subcrop 50 ms below the modern sea floor. Like the modern examples, the sediment waves are oriented NW-SE. Lineations in the NW show a similar appearance as the observed longitudinal ridges on the sea floor (Fig. 3.11). This pattern is also reflected by the strength of the variance signature belonging to the southwestern extents of the sediment-wave field, indicating the lineations to be erosive features. The seismic section shows that unlike in Zone 2 on the modern sea floor, the faults (that are oriented E-W on the variance map) crosscut and therefore postdate the sediment waves. Seismic acquisition footprint oriented E-W.*

A prime example of a buried sediment-wave field is PSW1.4 (Fig. 3.13). As in most of the modern examples, the sediment waves of this field are NE-SW oriented. Variance signatures of varying quality imaging sediment waves are discernable over an area of approximately 150 km^2. In the north these signatures are clearest, however they are very faint in the east. In the southwest isolated ribbons of strong signatures are visible, the alignment of which is similar to that of the signatures belonging to presumed palaeo-ridges or furrows in the northwest. This relationship indicates that the south-western part of the sediment wave field may have been subject to erosion prior to burial. In contrast to the sea floor sediment waves of Zone 2, fault control appears not to have played a role in the formation of the buried sediment waves in this example, with faults only very recently intersecting the deposits.

Table 3.2: Overview of the seismic-geomorphological characteristics of the buried sediment-wave fields analysed in this study (bsl: below sea-level; bsf: below sea floor).

Name	Field size [km^2]	Spacing [m]	Main orientation	Approx. depth [s TWT bsl]	Approx. depth [s TWT bsf]
PSW1.1	39.3	140-160	N-S / NNE-SSW	0.61-0.63	0.03-0.07
PSW1.2	43.7	170-220	N-S	0.55-0.58	0.02-0.10
PSW1.3	104.6	130-160	N-S / NNE-SSW	0.58-0.69	0.03-0.10
PSW1.4	150.6	220-260	NE-SW	0.59-0.67	0.01-0.08
PSW2.1	95.1	340-450	NNW-SSE	0.38-0.44	0.05-0.15
PSW3.1	24.9	-	N-S	0.82-0.84	0.10-0.16
PSW3.2	44.3	(120)	N-S / NNE-SSW	0.84-0.93	0.13-0.22
PSW4.1	13.8	(150-200)	N-S	0.95-0.97	0.25-0.27
PSW5.1	114.6	120-200	N-S	0.92-1.03	0.33-0.41
PSW6.1	9.7	90-130	N-S	0.96-0.99	0.38-0.47
PSW6.2	22.0	160-200	N-S	0.97-1.00	0.38-0.43
PSW6.3	20.4	130-160	NNE-SSW	1.03-1.12	0.30-0.38
PSW7.1	40.1	75-160	NNE-SSW	0.97-1.05	0.42-0.47
PSW8.1	53.7	100-140	N-S	1.06-1.08	0.49-0.51

3.6 Discussion

The dominant seismic-geomorphological and seismic-sedimentological bedforms in the study area are sediment waves, sea floor furrows and ridges, and their buried counterparts. A discussion of the processes controlling the development of these features is possible using the bedform-velocity matrix of Stow et al. (2009) based on a large dataset of siliciclastic and carbonate dominated environments. This constrains the average grain size and bottom-flow velocity required to generate bedforms of a specific geometry and dimension. According to the definitions given by Stow et al. (2009), sediment waves with a spacing between 120 and 400 m and a maximum height of 10 m as observed on the upper continental slope, immediately below the shelf-slope transition, or <5 m on the shelf best fit into the category of sand waves.

Winnowing and transport of sediments on the modern NWS (Jones 1971, 1973; James et al. 2004) is reflected by the multitude of longitudinal furrows that shape vast regions within the survey area. These most likely formed through erosion by secondary helical flow patterns (Flood 1981, 1983). Due to the limit in vertical and lateral resolution of the 3D seismic data there is no hard, measurable information on the surface morphology of the furrow and ridge systems to compare with the data of Flood (1983). Based on the bedform matrix of Stow et al. (2009), erosional furrows may either form at higher flow velocities than sand waves within material of the same grainsize or, alternatively, at the same flow velocities in finer sediments, such as mud. The former may be the case in the region of sediment wave field SW3.2, where the furrows have a less regular appearance than elsewhere in the study area, a characteristic usually observed in sand furrows (Flood 1983). The latter may be the case throughout the remaining furrow fields.

It is important to keep in mind that most of the sediment-wave fields of the study area occur in conjunction with morphological irregularities, such as terraces or fault escarpments, features with prominent relief that potentially influence currents and therefore possibly the local lithological distribution. Combined with the apparent variability in grain sizes displayed by the available sedimentological data in the study area, a sample-based verification of the sea floor and subsurface features interpreted on the 3D seismic-

reflection data is not yet possible. However, the classification of the observed bedforms as most likely sand waves and muddy or sandy furrows and ridges constrains, sensu Stow et al. (2009), the magnitude and range of flow velocities for sediment mobilization. In order to form sediment of sand and mud grain-sizes into bedforms of the observed geometry and dimension, flow velocities of 0.3 to 0.75 $\frac{m}{s}$ would be necessary for sand-waves, velocities of >0.3 $\frac{m}{s}$ for mud furrows and velocities of 0.6 to 1.5 $\frac{m}{s}$ for sand furrows (Stow et al. 2009). As the number of possible oceanographic factors that need to be considered in respect to flow velocity on the sea floor depend on the water depth, it is necessary to differentiate between two fundamental assumptions at this point, whether; (i) the observed bedforms are seen as inactive, having formed in the past at shallower water depths in times of lowered sea-level; or if (ii) the bedforms are recent (or relatively recent) features formed in water depths, flow regimes, depositional and morphological environments identical or at least similar to those of today.

When interpreting the sediment waves as inactive and conserved bedforms, their development could most easily be explained in shallow water depths governed by the impact of surface waves, which would offer sufficient bottom-flow velocities. On the NWS, the depths that are affected by storm waves reach down to ca 115 m (Fig. 3.14), whereas the fairweather wavebase is generally shallower than 50 m (James et al. 2004). The drowned marine terraces documented by Jones (1973) indicate multiple stages of water depth changes shaping the sea floor. The most distinct and widespread drowned terrace on the NWS is located today at approximately 120 m water depth, a depth level commonly attributed to the global sea-level lowstand of the last glacial maximum (Jones 1973). A study-area-wide lowering of the sea-level by 120 m would place most of the observed sediment waves as high as the swell-wavebase domain (Fig. 3.14), which is above 300 m water depth (James et al. 2004). It is however doubtful that the energy of the swell alone would be sufficient to reach the necessary bottom-flow velocities for the interpreted sand waves and mud/sand furrows and ridges. The lowest observed terrace levels of the study area on the other hand are located at depths between 260 and 280 m and are reported to be of pre-Pleistocene age (Jones 1973). In contrast, the oldest surface sediments on the NWS are of terminal Pleistocene age (James et al. 2004), postdating the terraces. A generation of the bedforms in shallower water by fairweather-waves or

storm-waves and a subsequent conservation on the sea floor appears, with respect to the involved timescales rather unlikely.

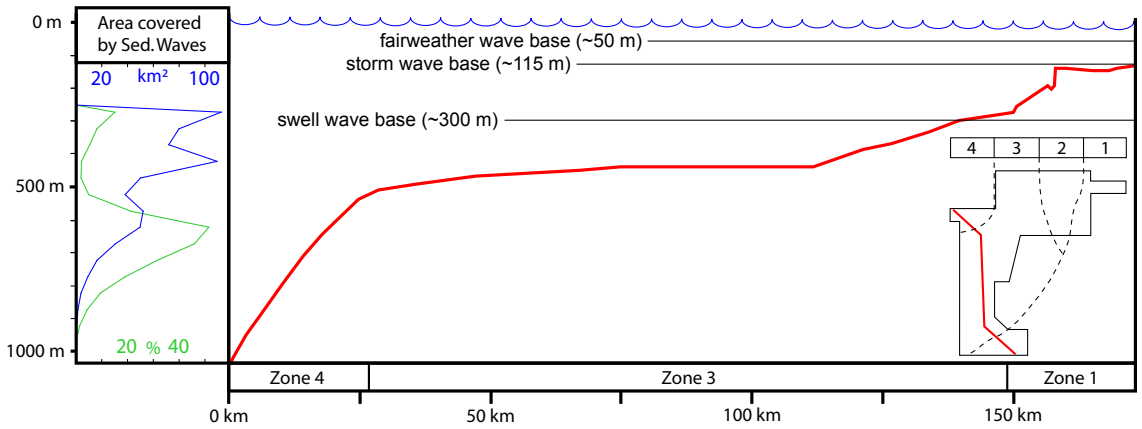

Figure 3.14: *Bathymetrical profile across the survey area from its shallowest elevation, the top of a terrace in the south at 120 m to 1000 m water depth on the slope, overlain with barotropic wave bases as reported by James et al. (2004). The percentage of survey area of a certain water depth that is covered by sediment waves is indicated on the left in green, and the total area in blue. Overall there are two main sediment wave populations, one on the shelf and one on the upper continental slope. Note that all terraces in the study area occur below the storm wave base.*

The interpretation of the observed bedforms as recent morphological structures would exclude any direct influence of surface waves on their development, as the respective water depths are too great (Figs. 3.3A & 3.14). However, since strong seabed currents reportedly caused problems and delays during the initial drilling stage of the exploration well Caswell 1 in the south of the study area (Fig. 3.3A; WCR Caswell-1 1978), a number of other mechanisms inducing bottom currents must be considered: these are (i) oceanic currents (e.g. contour currents of Trincardi et al. (2007); counter currents of Grasmueck et al. (2006), Correa et al. (2012)); (ii) gravity currents (e.g. Simpson 1982); (iii) turbidity currents (e.g. Lowe 1982; Betzler et al. 2013); and (iv) internal waves or tides (e.g. Holloway 2001; Pomar et al. 2012) that may cause or make a contribution towards significant bottom flow velocities at these depths. The occurrence or absence of larger-scale oceanic currents within the survey area is hard to deduce based on the available 3D seismic data alone. However, most of the sediment waves are not oriented perpendicular to the local contours and thus make the existence of a dominant contour current unlikely. Other strong currents comparable to e.g. the unidirectional counter current observed to influence the sea floor in the Straits of Florida (Grasmueck et al. 2006; Correa et al. 2012) may

exist in this area, but have not been proven. Gravity currents caused by higher salinity coastal waters that form by evaporation and flow down the shelf do not propagate any deeper after reaching their density equilibrium at approximately 200 m water depth (James et al. 2004). With respect to turbidity currents, the relatively planar shelf regions of the survey do not exhibit slope angles sufficient to generate and maintain such flows (Fig. 3.3B). However the steeper areas below the shelf break and on the continental slope, for example around sediment wave field SW4.1 (Figs. 3.2 & Fig. 3.3), can bear sediment waves constructed by gravity flows. In this particular setting it is yet difficult to establish whether the observed sediment waves within the channels (Fig. 3.9) were directly formed by turbidite flows (e.g. Malinverno et al. 1988; Wynn et al. 2002), or if the turbidite deposits were reworked by other bottom currents in the channels (e.g. Shepard et al. 1979), as both processes would result in bedforms of comparable dimensions (Lesshafft et al. 2011). The sediment waves on channel B (Fig. 3.9) are isolated from the main sediment wave-field SW4.1 and exhibit a slight landward curvature that may hint at a turbiditic origin, as the typical upward migration of sediment waves formed by turbidite flows increases together with the flow velocity towards the channel-axis (Wynn et al. 2000). For channel A, the interpretation of a current reworking the sediments is favoured, as the sediment waves have straight crests and appear to be continuous up to the shelf break.

The recurrence of directional bottom flows could alternatively be explained by the presence of internal waves, gravity waves that propagate along density boundaries. These may occur periodically as internal tides or isolated as internal solitary waves (e.g. Pomar et al. 2012). The waters of the Australian NWS are generally tide dominated (Porter-Smith et al. 2004), which together with the complex and steep topography of the Browse Basin and an almost constant water-density stratification during the year creates an ideal setting for the generation of a large amplitude semi-diurnal internal tide (Rayson et al. 2011) as well as solitons (Apel 2002).

Internal solitary waves in shelf waters may occur by nonlinear steepening of the internal tide as it moves towards the shore on a sloping shelf (Holloway 1987). On the NWS the occurrence of solitons is documented through satellite observations (Baines 1981) and field data obtained from moorings in the vicinity of the North Rankin A platform (see Holloway 1987) and in direct vicinity of the study area at the Prelude FLNG project site

(Fig. 3.1; see Van der Boon 2011). The data presented by Van der Boon (2011) indicates that solitons occurred throughout the year and led to maximum bottom flows of 0.71 $\frac{m}{s}$ at the 255 m deep Prelude site (Fig. 3.1). Of the different types of solitons discussed by Van der Boon (2011), depression waves appear to have the biggest influence on bottom flows. Although directed offshore to the NW, the depression waves have a SE orientation within the lower layers (Van der Boon 2011). Thus, both direction and strength of the bottom flows induced by the depression wave solitons support the generation and the observed orientation of the sediment waves interpreted on the 3D seismic data, at least in shallower water. In addition, sediment waves of comparable size that occur in similar water depths to those observed in this study were analysed on the upper continental slope in the South China Sea (Reeder et al. 2011), where their generation was proposed to be associated with internal solitary waves that are believed to trigger highly energetic resuspension events in depths of over 600 m (Reeder et al. 2011).

The occurrence of a large semi-diurnal internal tide on the Australian NWS was first documented by Holloway (1983a, 1984, 1987) and described as being directed shoreward in a NW-SE orientation (Van Gastel et al. 2009). Assuming that sediment waves formed by bottom currents should develop at a normal to oblique orientation in respect to the mean flow direction of the current (Wynn and Stow 2002), most of the observed sediment waves (as well as the observed furrows) could be created by bottom flows with such an orientation. At which water depths bottom flows that are induced by the propagation of depression waves (Van der Boon 2011) and the breaking and shoaling of internal waves on a slope (e.g. Southard and Cacchione 1972; Aghsaee et al. 2010) may occur, depends on the depth of the pycnocline. Around the study area, the main pycnocline was measured at 100 m water depth at Scott Reef (Wolanski and Deleersnijder 1998), which appears to be in agreement with the temperature and buoyancy frequency data published by Rayson et al. (2012). Further southwest on the NWS, on the shelf offshore of Port Hedland, it was reported to lie at the slightly greater depth of 150 to 250 m (Brink et al. 2007). Given the water depths of the furrows and sediment-wave fields in respect to the main pycnocline, the concept of secondary stratification (Shanmugam 2013b), possibly aided by intruding salt layers (Turner 1998), may serve to supply additional density boundaries deeper in the water column.

Besides moving along density boundaries, the wave energy of internal tides in a setting of continuous temperature stratification also has the ability to travel independently of density interfaces in the shape of rays (Pomar et al. 2012). These form by the superposition of multiple tidal modes (e.g. Gerkema et al. 2004) and have the ability to reflect off the sea floor and sea surface, enabling them to propagate away from their site of generation (Jackson et al. 2012). When intersecting a sloping shelf, the nature of interaction depends on the angle of slope in relation to the internal tidal characteristic, a value determined by the frequency of the internal waves, the local density profile and the latitude (Cacchione et al. 2002). In the case of both values being significantly unequal, the ray may be reflected. Alternatively, if both values are equal, in which case the slope is termed critical, internal wave energy may be transferred into the generation of along-slope currents in the area of incidence (e.g. Thorpe 1999; Zikanov and Slinn 2001).

The generation and trajectories of wave energy rays in the Browse Basin region were analysed in the analytical model of Rayson et al. (2012), which is based on mooring data collected south of Scott Reef (Fig. 3.1). Rayson et al. (2011, 2012) describe a partly standing internal wave in the shelf area of the Browse Basin, generated at spring tide by opposing internal waves forming at the shelf break on the one side and at submerged terraces in water depths between 100 and 250 m on the other. The corresponding wave-energy trajectories across the shelf calculated by the model are presented in a vertical section (Rayson et al. 2012; their fig. 11), indicating that flow velocities of approximately 0.5 to 1 $\frac{m}{s}$ can occur near the sea floor in a zone that shifts from 250 to 350 m water depth in the Australian summer to around 250 to 300 m in the Australian winter. Although the section in question does not intersect the seismic survey of this study and is positioned further south-west (Fig. 3.1), the calculated wave-energy trajectories still correlate surprisingly well with the relative position and water depth of the sediment-wave fields documented in this study (Figs. 3.3A & 3.14).

The different types of internal waves described above may cause or contribute to increased bottom flows in the areas marked by sediment wave fields in Zones 1 through 3. However, since the sediment waves in the study area dominantly occur in the vicinity of sea floor structures (Figs. 3.2 & 3.3A), it seems that bottom flows alone may not suffice for their generation and that an interaction with sea floor relief (exerting a local influence

on sedimentary processes) may also be of importance. This could either be by providing accumulation shelter for sediments otherwise transported across the shelf, or - in turn - by locally increasing the flow velocity through the obstruction, diversion or channelling of bottom flows (Viana et al. 1998).

For example, in depositional zone 1 of the study area (Fig. 3.3A), the terrace escarpments form an obstacle for potential NW-SE oriented flows, possibly leading to an increased flow down the sedimentary wedge towards the foot of the terrace. It is also possible that a flow along the terrace forms, but this would conflict with the orientation of most sediment waves, with the only exception being the north-western half of SW1.1. In this particular case the sediment waves are oriented roughly perpendicular to the terrace and have not developed uniformly on the sides of a raised fault block (Figs. 3.5A & 3.6A). The arrangement of sediment waves around this morphological obstacle and their slight NW-convex curvature may point towards a NW-directed flow direction being dominant. Furthermore, it can be noted that the sediment wave fields of Zone 1 are positioned at water depths and distances from the terrace similar to those of the most shoreward reflection of internal wave energy in the model of Rayson et al. (2012), also providing a mechanism which could explain increased bottom flows. Sediment waves in a similar setting, located basinward at the foot of a terrace escarpment with adjoining rise, can be found in comparable water depths on the upper continental slope in the South China Sea, which is also a region known for the occurrence of very large internal solitary waves (Reeder et al. 2011).

The development of sediment waves in Zone 2 on the other hand, might be dominantly influenced by the differential topography created by modern faulting (Fig. 3.6). Since the sea floor in the area of sediment-wave field SW2.1 generally dips to the west (Figs. 3.3 & 3.6B), towards a local depression basinwards of the main faulted area, the low-lying fault blocks define topographic lows that may attract bottom currents flowing up or down the shelf. Additionally, flow velocities within the topographic lows would also be locally enhanced by the comparative increase in slope angle (Viana et al. 1998). The higher frequency of bifurcations and the shorter length of the sediment waves in Zone 2 could very well result from varying flow velocities within the graben systems, ultimately reflecting differences in the slope gradient or irregularities of the bounding fault planes.

In the southwest of the survey, the two largest sediment-wave fields of Zone 3 (Fig. 3.3A) also display a comparatively large variation in their internal crest orientation (see Figs. 3.7 & 3.8). In the area, a NNW-SSE to NW-SE-oriented mean bottom-current direction possibly affected by varying sea floor dip can be inferred from the erosional furrows present in the region. Their larger scale in the surroundings of sediment wave field SW3.2 and their partial superposition (and thus the implied reworking of the sediment waves) may be indicative of higher flow velocities. The observed irregular crest orientations and curved furrows on the other hand may be an indicator of a less constant flow orientation over time. Variations in the flow regime may result from the additional influence of, for example, contour currents or a different set of internal waves. In this regard, Rayson et al. (2011) describe landward directed internal waves that are not generated at the outer shelf break, but instead at Scott Reef, propagating south-eastward across the shelf and possibly affecting the study area.

Zone 4 finally contains only sediment wave field SW4.1, which begins at the shelf break and reaches partway down the submarine channels of a canyon head. This setting differs from those of Zones 1 through 3 and consequently, different mechanisms inducing bottom flow may apply. It can be expected that relative to the internal tides on the shelf, those on the NWS slope may be more energetic, as the density stratification in these water depths is more persistent and less influenced by seasonal changes (Nash et al. 2012). The upslope area around the shelf break and to a certain degree the lower shelf thus may experience bottom flows induced by the passing of vortex cores of denser fluid (Venayagamoorthy and Fringer 2007) or thermal fronts (Thorpe 1992). These internal boluses might move upslope across the shelf, forming when internal waves overturn and break on a critical slope, a phenomenon that has been modelled by Venayagamoorthy and Fringer (2007) and that has been documented in several coastal settings (e.g. Bourgault et al. 2008; Klymak and Moum 2003; Scotti and Pineda 2004). With respect to the sediment waves observed within the slope channels of the study area (Fig. 3.9), internal tides themselves also need to be considered. Shepard et al. (1979) documented currents in submarine canyons flowing both upslope and downslope at semidiurnal tidal frequencies, indicating a connection to internal tides (Pomar et al. 2012, 2013). The highest current velocities within canyons were observed to occur at water depths between 400 and 600 m,

with a sharp decrease towards shallower and a more gradual decrease towards greater depths (Shepard et al. 1979; their fig. 15). This dependency may explain why no sediment waves are visible further downslope.

In addition to the sediment waves observed on the modern sea floor, buried analogues could be detected at depths of up to 500 ms (TWT) below. Buried sediment-wave fields have been analyzed before by, for example, Dunlap et al. (2013) documenting their general preservation potential in the sedimentary record for such bedforms. In the study area the modern sediment waves, when compared to those of the subsurface, show many similarities such as the field size or crest spacing. The crest orientation is also quite similar, although the buried sediment waves show a more dominant N-S trend. The palaeo-sediment waves presented can be approximated to have formed in post-Messinian times and the strong resemblance to their modern counterparts suggests that the processes controlling their development (including internal waves) were comparable to today.

3.7 Conclusions

3D seismic reflection data of the northern Browse Basin, Australian NWS, enabled mapping of the 3D geometry and spatial distribution of various large-scale sea floor bedforms including sediment waves, furrows and elongate sediment ridges over areas of several hundreds of square-kilometres. These bedforms were not only discovered and analysed on the modern sea floor, but were also documented within the uppermost part of the seismic-sedimentary record down to depths of ca 500 ms (TWT). The extent, orientation, morphology and seismic signature of the sea floor sediment waves and furrow-ridge systems varies across the study area depending on the respective location: the modern sediment waves dominantly occur in conjunction with morphological irregularities including submarine terrace escarpments, fault-scarps, incised channels as well as mass wasting deposits. These areas of pronounced submarine relief seem to provide in many cases shelter against strong bottom currents that can be erosive or, at least, keep sediment in transport. In contrast, furrows and sediment ridges are dominantly located on the plane portions of the shelf. This indicates that significant regions of the 3D survey

area are today controlled by current erosion and sediment movement, with the dominant bottom-flow orientation interpreted from the furrow orientation between the SE and the NW; this direction is in line with the orientation of present-day internal tides in the greater study area.

Many arguments indicate that the sediment waves of the study area also formed under the present-day environmental conditions at their current position. Their development can be best explained by the activity of internal waves generating bottom flows sufficient to locally re-distribute sediment of variable grain size. Based on the height and spacing, the building material of the sediment waves of the study area comprises most likely sand-sized grains. Based on the comparable morphology and orientation of the observed buried sediment waves, similar processes may have persisted since their post-Messinian formation.

A final statement addressing whether individual 3D sea floor bedforms of the northern Browse Basin are today inactive and subject to erosion or actively growing or migrating is difficult with the given industry seismic data. To examine these aspects, access to additional high-resolution 2D seismic transects in combination with precise grab samples, short cores and precise age dating would be advantageous. A better understanding of the local bottom currents could ultimately be gained by performing current-meter measurements at sediment-wave and furrow sites.

3.8 Acknowledgements

We thank Geoscience Australia for access to the 3D seismic data. The Department of Mines and Petroleum (DMP) of Western Australia is thanked for providing well data and reports through the database WAPIMS. IHS is gratefully acknowledged for providing the KINGDOM software under an Academic User License Agreement. Schlumberger is acknowledged for providing the software Petrel. The Gocad research group and Paradigm are gratefully acknowledged for providing the software Gocad. Conny Lutter is particularly thanked for her help in acquiring scientific literature. Reviewer S. Bachtel, an anonymous reviewer and the Sedimentology editors G. Eberli and T. Frank are gratefully

acknowledged for their helpful comments and suggestions on improving the manuscript. This study is a spin-off of project RE 2697/3-1 funded by the Deutsche Forschungsgemeinschaft (DFG). J. Belde is funded by DFG project BA 2136/4-1.

Chapter 4

Sediment waves imaged on seismic reflection data from the high-energy carbonate ramp of the Northern Carnarvon Basin, North West Shelf Australia

The contents of this chapter are an early draft of the manuscript. A revised version was published in March 2017 with the title "Bottom currents and sediment waves on a shallow carbonate shelf, Northern Carnarvon Basin, Australia" in the Journal of Continental Shelf Research Volume 138, pages 142-153, by J. Belde, L. Reuning and S. Back of the EMR Geological Institute, RWTH Aachen University, Wüllnerstr. 2, 52062 Aachen, Germany.

4.1 Abstract

The modern seafloor of the Australian Northwest Shelf between Exmouth and Dampier was analyzed for large scale sedimentary bedforms on 3D seismic reflection data. The PGS Carnarvon MegaSurvey, a merged dataset of multiple industrial 3D seismic reflection surveys with a total size of 49,717 km^2, offers an extensive view of the continental shelf, slope and rise of the Northern Carnarvon Basin. On the shelf portion of the data two fields of large scale sediment waves could be observed in water depths between 55-130 m, where the seafloor may be influenced by different processes including internal waves, tides and storms. The grain sizes of the sediment and the dominant local currents could be estimated based on the dimensions and orientations of the sediment waves.

These estimates are generally consistent with local grain size data from the auSEABED database. The first sediment wave field, positioned northwest of the Montebello Islands where the shelf is comparatively narrow, has most likely formed through increased bottom currents induced by the diversion of tidal flows around the islands. The second sediment wave field is positioned north of the Serrurier and Bessieres Islands within a local seafloor depression containing poorly sorted sediments. The coarser sediment fraction could have been reworked to sand waves by cyclone-induced bottom currents. Alternatively, the finer sediment fraction could form mudwaves shaped by less energetic along-slope oriented currents in the topographic depression. The sediment waves consist partially of carbonate grains such as ooids and peloids that formed in shallow water during initial stages of the post glacial sea-level rise. These stranded carbonate grains therefore formed in a different environment than the sediment waves in which they are incorporated. In fossil examples of similar high-energy ramp systems this possible out-of-equilibrium relationship between grains and bedforms has to be taken into account for the interpretation of the depositional environment.

4.2 Introduction

Large scale sedimentary bedforms such as sediment waves can be analyzed on 3D seismic reflection data and used as indicators for local sediment mobilization. Sediment movement on this scale may prove hazardous to submarine installations, potentially destabilizing underwater drilling platforms and moorings or causing free spans in pipelines. Sediment waves along the Australian Northwest Shelf (NWS) and on the northern extends of the west coast were documented at several sites (Jones 1973; James et al. 2004; Jones et al. 2009; Nichol and Brooke 2011; Belde et al. 2015), indicating that these types of bedform are common in the region.

The study area on the NWS is located between Exmouth and Dampier (Fig. 4.1), a region known for its significance in hydrocarbon exploration and production. A significance that is also reflected in the amount of data available on three key aspects: the morphology of the seafloor, current measurements and the detailed data on sediment grain size distri-

bution. The shelf is imaged over a large area by multiple industrial 3D seismic reflection surveys providing information on the morphology of the modern seafloor. The oceanography of the region has also received comparatively much attention, partially owed to the several platforms and pipelines present, including analysis of long term flow meter measurements (e.g. James et al. 2004; Van Gastel et al. 2009; Van Gastel 2010) and detailed computer models (e.g. Condie and Andrewartha 2008; Van Gastel et al. 2009; Van Gastel 2010). Information on sediment grain size distributions are provided by the auSEABED database (Jenkins 2000).

Choosing 3D seismic reflection data instead of, for example, multibeam sonar to analyze large scale bedforms on the shelf has the advantage of providing a much larger study area, while the resolution is nevertheless sufficient to gather information on the dimensions, water depths and orientations of large scale bedforms. A large study area can provide a much deeper insight into the distribution and frequency of occurrence of bedforms, while also drawing a more comprehensive picture of their relationship to the shelf morphology. This is particularly the case when the occurrence of bedforms is limited or favoured by slight differences in relief or slope angle, or if a relationship of the bedforms to the proximity of submarine structures like terrace escarpments can be established. The dimensions of the bedforms, in the case of sediment waves the height, width and spacing, are useful to estimate the local current velocity and may also help to infer the approximate grain size of local sediments (Stow et al. 2009). The water depth of the observed bedforms determines the relevant oceanic processes responsible for sediment mobilization at the respective site, which in this study include storm and swell waves, internal waves and along slope oriented currents. Although the influence of tidal currents on sediment mobilization in the Northern Carnarvon Basin is interpreted to be negligible (Porter-Smith et al. 2004), models by Harris et al. (2000) and Condie and Andrewartha (2008) indicate that tidal currents may nevertheless in some places result in increased energy dissipation on the seafloor and thus can not be dismissed entirely. The orientation of the bedforms can also help to further constrain the origins of the local bottom currents, as these are commonly oriented approximately normal to the direction of the local mean current orientation.

Making use of the extensive data available on the oceanography and sedimentology of the region, the most likely mechanisms responsible for the development of the observed sediment waves are discussed and compared to the interpretations of similar bedforms along the NWS and the northern west coast.

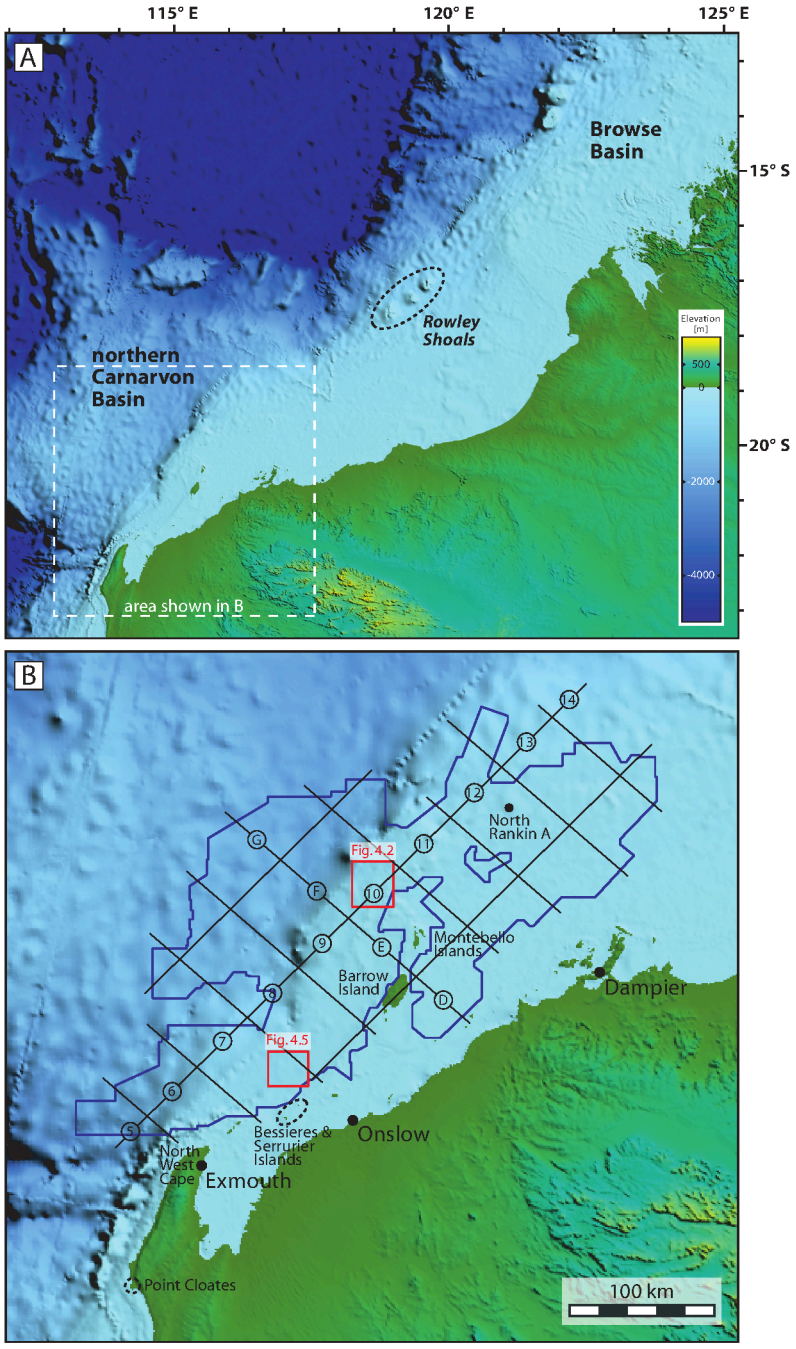

Figure 4.1: *Map showing the location of the PGS Carnarvon MegaSurvey 3D on the Australian NWS. The survey is subdivided into multiple data cubes, referenced by the letters D-G in the offshore and the numbers 5-14 in the alongshore direction. The bathymetry is provided by a GEBCO one-minute-resolution bathymetry grid. Locations of the figures 4.2 and 4.5 are indicated by red boxes.*

4.3 Physical Setting

The study area is located on the Australian NWS between 19° and 21° S and 113° and 117° E, offshore North West Cape and Dampier (Fig. 4.1). The 3D seismic reflection data analyzed in this study extends over the Rankin Platform, including the Exmouth, Barrow and Dampier sub-basins and the SE edges of the Exmouth Plateau. Water depths ranging between a few metres down to 1.600 m are imaged, but the main focus of this study lies on the shallow sections of shelf (<250 m) above the slope.

The NWS is a tropical carbonate ramp with an oceanic regime defined by swell waves, large tides, internal tides, internal solitary waves, tropical cyclones and oceanic currents such as the Indonesian Throughflow and the Leeuwin current. The fair-weather-, storm- and swell wave bases lie at around 50 m, 115 m and 300 m respectively (James et al. 2004).

Swell waves are generally defined as wind forced surface gravity waves that have moved outside of their generating area (Thomson 1981). For example waves generated by a distant storm may arrive as swell at the shelf (Munk et al. 1963). Due to the effect of dispersion, swell waves are synonymous with gravity waves of large wavelengths (Thomson 1981). Results from the GEOMAT modelling project show that within the study area the wave-induced sediment mobilization threshold may be exceeded in some regions for grains between 0.5-0.01 mm in diameter (Harris et al. 2000, their figures 9A-C). This indicates the possibility of sediment with grain sizes between silt and coarse sand, if present, to be locally transported or suspended by swell waves in these areas (Harris et al. 2000).

The tides on the NWS are semidiurnal and their rate and direction heavily influenced by the local morphology of the coastline and seafloor (Jones 1973). Tidal ranges vary strongly along the NWS and increase from the south (e.g. 1.5 m in Carnarvon) towards the north (e.g. 8.5 m in Broome) (Jones 1973), a cross-shelf amplification associated with the widening of the shelf (Holloway 1983b). In general the tidal currents on the shelf are oriented in cross-shelf (NW-SE) and off the shelf in along-shelf direction (Van Gastel 2010; Jones et al. 2009). The area around Barrow Island and the Montebello Islands forms an exception where the tidal currents are oriented closer to east-west (Condie et al.

2006; Condie and Andrewartha 2008). Tidal movements within the study area are ebb-dominated (Porter-Smith et al. 2004).

The Australian NWS hosts a complex internal wave climate, a result of the interaction of the persistent density stratification and strong barotropic tide with the complex topography (Rayson et al. 2011), which has been the focus of continuous research (e.g. Holloway 1983a, 1984, 1987; Van Gastel et al. 2009). The density stratification on the NWS is constant in deeper water, i.e. seaward of the shelf-slope transition, but varies in shallower regions such as the shelf (Nash et al. 2012). In the winter the shelf waters are well mixed down to a depth of 120 m, but become well stratified in the summer with the thermocline lying in around 30-60 m water depth (James et al. 2004). However, even in summer the temperature stratification is weaker on the shelf inhibiting the generation of internal tides (e.g. Baines 1982), which results in internal tides being an order of magnitude less energetic across the shelf in comparison to regions seaward of the slope (Nash et al. 2012).

On the upper slope of the NWS large semidiurnal internal tides are generated that propagate onshore, oriented approximately normal to the slope (approximately NW-SE), and dissipate over the outer-shelf (Holloway 1983a, 1984, 1985, 1987; Craig 1988; Holloway et al. 1997; Holloway 2001; Katsumata 2006). These internal tides have a semidiurnal character and show a strong seasonal variability (Holloway 1983a, 1984, 1987; Van Gastel et al. 2009). As the internal tides move onshore they evolve into internal solitary waves and other non-linear wave forms (Baines 1981; Holloway 1987, 1994; Holloway et al. 1997; Lim et al. 2008). Field measurements in the region of the North Rankin A (NRA) platform (Fig. 4.1) for example show the occurrence of large amplitude internal waves, which are most energetic during the transition from summer to winter conditions (Van Gastel et al. 2009). Bottom currents induced by such an event may locally reach velocities of up to 1 $\frac{m}{s}$ (Van Gastel et al. 2009).

Tropical cyclones on the NWS occur on average more than twice a year during the summer (Condie et al. 2006) and approximately every 2.5 years within the study area (Porter-Smith et al. 2004). Such storm events cause increased mixing, weakening the stratification of the water column (Davidson and Holloway 2003). Condie et al. (2006) have shown that this may lead to increased bottom stresses, especially in regions where the entire water

column becomes mixed, suppressing vertical shear through the absence of a thermocline. Thus modelled bottom stresses in areas like the outer-shelf, which were otherwise comparatively low, showed a strong increase during these storm events (Condie et al. 2006). Through their effect on the stratification of the water column, tropical cyclones may also modify the strength of the local internal wave regime (Davidson and Holloway 2003). Depending on the cyclone track relative to the sites of internal tide generation, the strength of the internal tide may be increased by cyclones moving parallel or normal to the shore, but may also, in turn, be decreased by cyclones moving over the shelf (Davidson and Holloway 2003).

The two main oceanic currents affecting the NWS are the Indonesian Throughflow (ITF) and the Leeuwin Current (LC). The ITF consists of warmer waters driven by a steric height gradient from the Pacific towards the Indian Ocean via the Timor Strait (Molcard et al. 1996; CSIRO 2004; Baker et al. 2008; Gordon et al. 2010). The waters of the ITF induce a pressure-gradient in the eastern Indian Ocean forcing warm surface water southward along the west coast of Australia, the LC (Smith et al. 1991). The strength of the ITF shows a strong interannual variability and a response to ENSO cycles, which in turn also affects the strength of the LC (Godfrey 2001; Zinke et al. 2014). In general, the LC is strongest in May and nearly ceases in September (Godfrey 2001). During May/June it originates as far north as 17° S on the NWS (Holloway 1995). The LC is around 100 km wide, mainly occurs within the upper 300 m of the water column (James et al. 2004) with indications of an oppositely oriented undercurrent directly beneath it (Godfrey 2001; James et al. 2004) and in general flows along the shelf edge (Godfrey 2001) and the slope region (James et al. 2004). Landward of the LC in water depths below 50 m the Ningaloo current, driven by south oriented wind stress, flows along the Australian west coast from Shark Bay past North West Cape and into the study area (Pattiaratchi 2006).

Sediments covering the Australian NWS are mainly comprised of carbonates, which in water depths between 50-100 m dominantly consist of relict and stranded particles (James et al. 2004). This reflects a decline in accumulation rate of typical warm water carbonates at around 12 ka associated with lower salinity water introduced by the LC in combination with rising sea-levels and a suppression of the modern benthic production by saline water plumes (James et al. 2004). As a result many sediments are no longer in equilib-

rium with their modern environment (James et al. 2004). Holocene sediments are sparse and consist mainly of heterozoan bioclasts and large benthic foraminifera (James et al. 2004). Due to the occurrences of cyclones (Lourensz 1981), the strength of the storm and fair-weather waves (Jones 1973; James et al. 2004) and the strong tidal currents the NWS is interpreted as a high-energy depositional environment (Dix et al. 2005). Currents appear to be strong enough to support sediment movement on the entire shelf (Jones 1973; James et al. 2004). The grain size data of the auSEABED database (Jenkins 2000) within the study area show a general trend of fine grain sizes mainly occurring in near-shore areas and along the shelf margin, as reported by Jones (1973). Since the study area lies on an ebb-dominated part of the shelf, mud-sized sediments are most likely winnowed and transported down the slope (Porter-Smith et al. 2004), leading to the majority of the outer shelf being dominated by sand and courser grain sizes (Jones 1973).

4.4 Data

The information on the seafloor morphology used (49,717 km^2) was provided by the 3D PGS Carnarvon MegaSurvey (Fig. 4.1). This dataset consists of over 30 individual 3D seismic reflection surveys whose data were time, amplitude and phase matched, re-gridded and in some cases reprocessed. The inline and crossline spacing is 50 m and the sample rate 4 ms. The PGS 3D seismic survey is supplemented by the AGSO Survey 136 / CTT-95 2D seismic survey, which consists of 28 2D lines (4,218 km) of data across the Carnarvon Basin. The lines shown have a sample rate of 2 ms. Both surveys are zero-phased in "European polarity", with a downward increase in acoustic impedance corresponding to a seismic trough. On seismic sections the seismic amplitudes are uniformly displayed in blue when positive and orange when negative. Isolines and dip-maps generated from a GEBCO bathymetry-grid with a one-minute-resolution were used to reference the absolute water depths of the observed structures in meters and calculate dip-angles of the topography. Data on surficial sediments within the study area is provided by the auSEABED database (Jenkins 2000) at a resolution of 0.1° (around 10 km). The database uses the Folk classification (Folk 1965) to define sediment types, which follows the Wentworth scale to specify grain sizes.

4.5 Interpretation

4.5.1 Seismic Interpretation

To obtain the clearest possible image of the modern seafloor morphology from the PGS 3D Carnarvon MegaSurvey, the first reflector with the highest amplitude, or in some areas the zero-crossing in amplitude above, was mapped. The resulting bathymetric image exhibits two large sediment wave fields positioned in comparatively shallow sections of the shelf (<130 m). Sediment wave field SWF-A (Fig. 4.2) is located in survey segment F10 (Fig. 4.1), in a comparatively steep region for the shallow shelf (0.38° mean, 1° maximum dip), and displays the most distinct morphological signature within the data. The second sediment wave field SWF-B, which is positioned at the intersection of segments E07-E08 (Fig. 4.1) on a comparatively plane section of the shelf (0.11° mean, 0.27° maximum dip), displays a less distinct morphological signature. In both cases the sediment wave fields are also imaged on intersecting 2D lines of the AGSO 136 2D survey, supporting the reliability of the interpretation.

Sediment wave field SWF-A (Fig. 4.2) has a size of approximately 115 km^2 and lies in relatively shallow water depths of around 55-100 m, directly seaward of a low morphological ridge and 11-16 km landward of the shelf-break. The wave crests are sinuous, have heights of up to 10 ms TWT (approximately 7.5 m assuming 1500 $\frac{m}{s}$ interval velocity) and are spaced between 200-500 m apart. The crests are oriented mostly normal to slightly oblique relative to the local isolines. For a detailed evaluation of the overall sediment wave crest orientation, crests clearly visible on topographical and variance maps were subdivided into linear segments and the resulting orientations plotted in a rose diagram, weighted according to their length (Fig. 4.3). This indicates a main crest orientation of approximately N (350-10°), with a secondary orientation of NW (310-320°) and an overall average orientation of NNW (347°). The auSEABED database (Jenkins 2000) shows that sediments in the area of the sediment wave field are mainly sand sized, with a substantial increase in gravel content to the SE (sample bins 5, 8, 11) towards the low morphological ridge (Fig. 4.4A). Based on this data the observed sediment waves are most likely sandwaves.

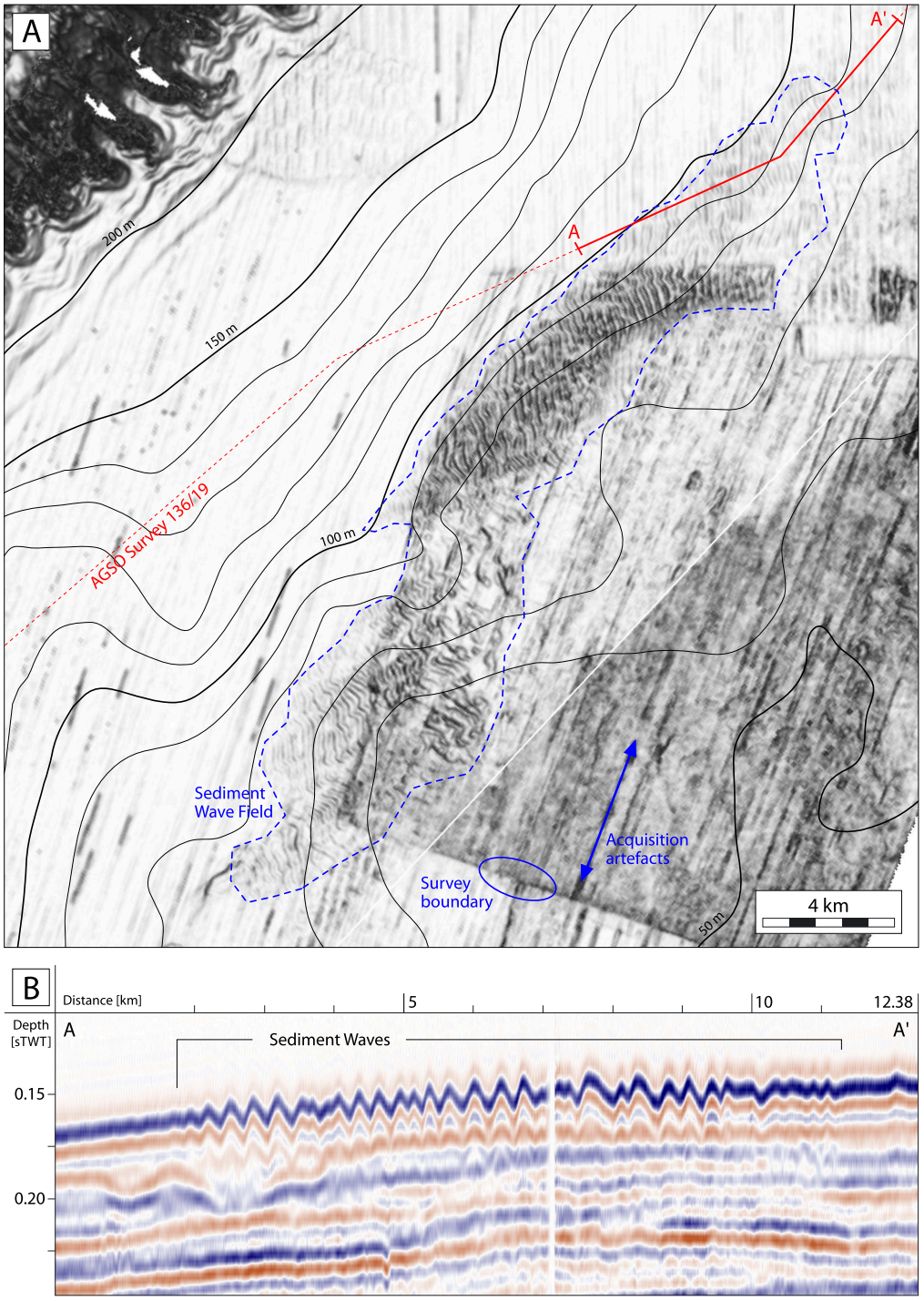

Figure 4.2: *A) A map of the variance attribute extracted along the seismic seafloor-reflector showing the sediment wave field SWF-A. Variance values and acquisition directions differ slightly for the different 3D seismic reflection surveys that were combined into the Carnarvon MegaSurvey. Depending on the respective surveys, acquisition directions are oriented approximately N-S in the northeast corner and approximately NNE-SSW in the rest of the figure. The waterdepth isolines are provided by a GEBCO one-minute-resolution bathymetry grid. The location of AGSO Survey 136 line 19 is indicated by a red dashed line and the section displayed in B by a solid red line. B) Seismic vertical reflectivity section of AGSO Survey 136 line 19 intersecting the sediment wave field SWF-A.*

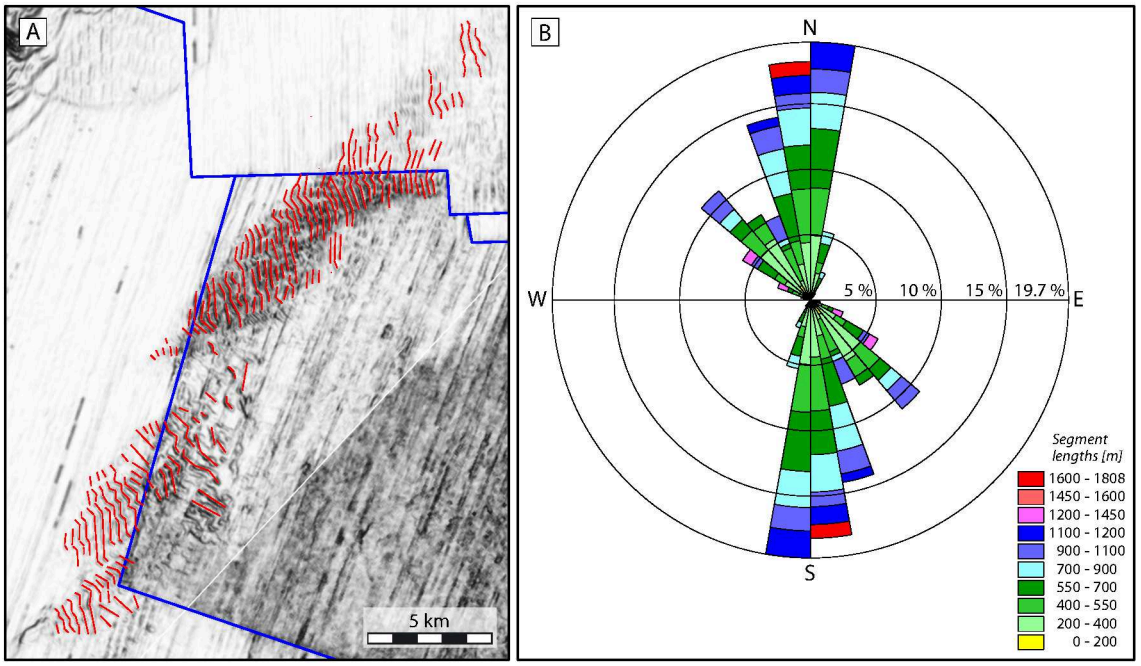

Figure 4.3: *A) A map of the variance attribute extracted along the seismic seafloor-reflector showing the sediment wave field SWF-A. The linear segments of clearly visible sediment wave crests used for the evaluation of the general orientation are indicated in red. The boundaries of 3D seismic reflection surveys combined in the Carnarvon MegaSurvey are indicated in blue. B) Rose diagram of the linear segments traced along the sediment wave crests weighted by segment length. The main crest orientation is approximately N (350-10°) with a secondary orientation of NW (310-320°). The average crest orientation is NNW (347°).*

Sediment wave field SWF-B occupies an area of approximately 114 km^2 and lies in slightly deeper water, between 100-130 m (Fig. 4.5). It is positioned at the landward edge of a comparatively planar segment of the shelf, at the foot of a rise in seafloor. Figure 4.5B shows that this rise also corresponds to the reflector against which the reflectors displaying the sediment waves form onlaps. The crests of the sediment waves are mostly linear although sometimes slightly curved at the edges of the field. The waves have heights of up to 4 ms TWT (approximately 3 m assuming 1500 $\frac{m}{s}$ interval velocity), a spacing of around 400-600 m and are oriented almost parallel to the local isolines. Due to the low crest height of the sediment waves the crest orientations had to be evaluated on a shaded relief image with increased contrast instead of topographical and variance data (Fig. 4.6). The main crest orientation is approximately N (0-10°) with an average orientation of 3°. Based on data from the auSEABED database (Jenkins 2000) sediment grain sizes in the area of the sediment wave field are mainly sand, except in the SE (sample bin 5) towards

the rise where the main component is gravel (Fig. 4.4B). In the central and south-western parts of the field grain sizes show a significant average mud component between 22.33% (sample bin 4) and 44.67% (sample bin 3). According to these data the observed sediment waves are most likely sandwaves, although the sediment contains a significant mud component. It has also to be noted that the sediment waves are best visible on the available data in the areas with the higher mud content.

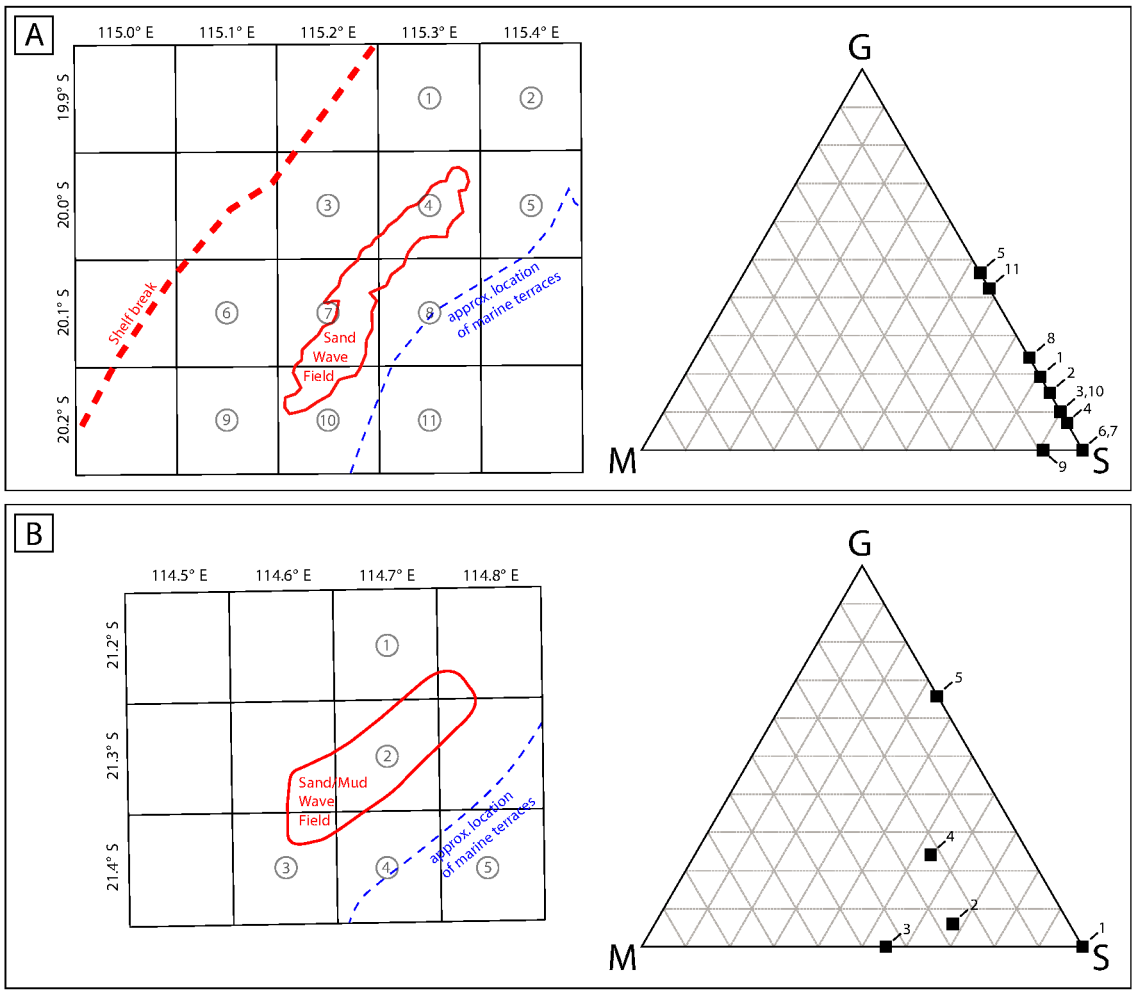

Figure 4.4: *Grainsize distributions around the sediment wave fields based on the auSEABED database (Jenkins 2000). A) In the region of SWF-A the sediments are on average mostly sand sized with no or a very small mud component. In the vicinity of the terraces, landward of the sediment wave field, the sediments contain increasing amounts of gravel (sample bins 5, 8 and 11). B) In the region of SWF-B the poorly sorted sediments are mainly sand sized, but also contain a large mud component and very little gravel. This trend appears to be inverted southeast of the sediment wave field towards the terraces, where the amount of gravel increases and mud decreases (sample bin 5).*

4.5.2 Topographic Analysis

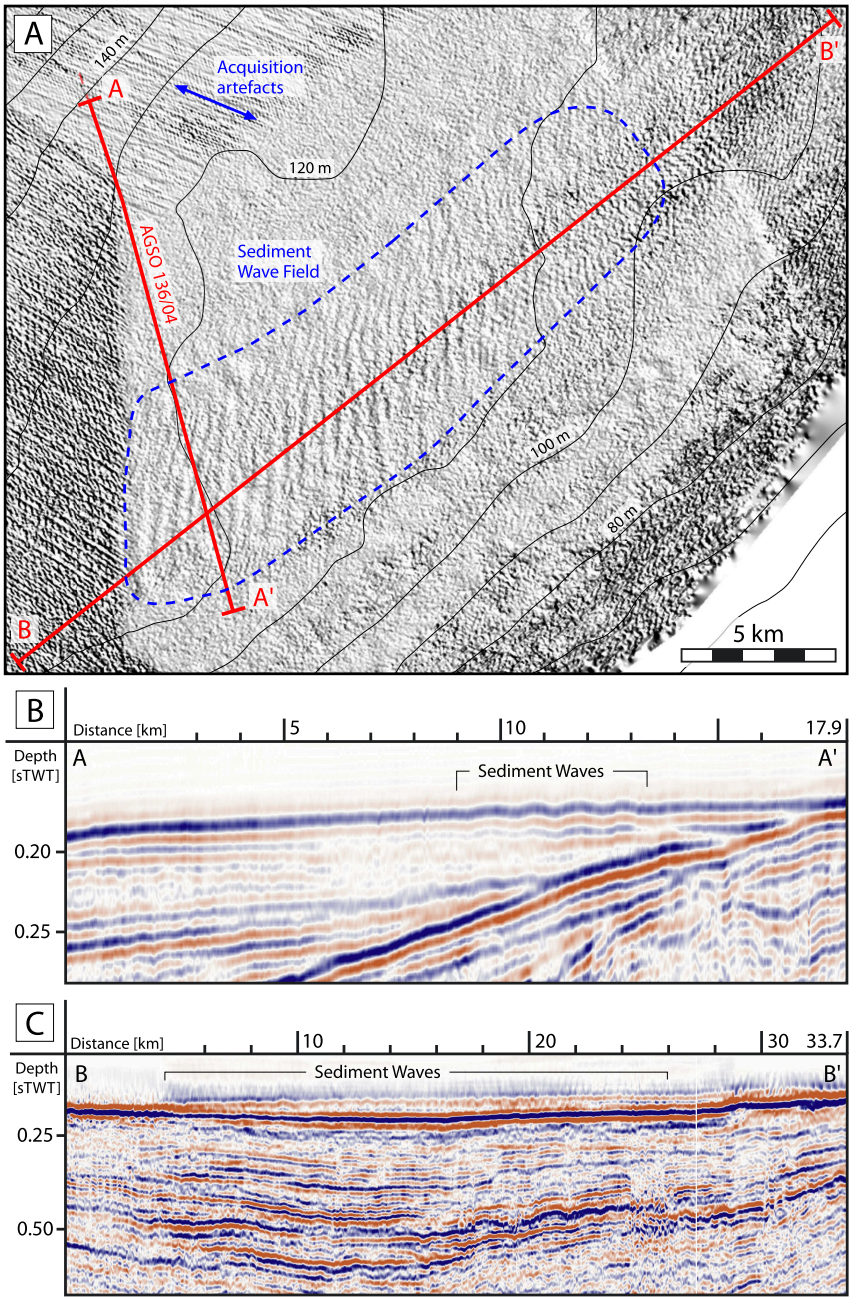

Figure 4.5: *A) The sediment wave field SWF-B shown on a shaded relief of the seismic seafloor reflector. The acquisition directions and data quality of the upper seismic reflectors of the individual surveys that form the basis of the PGS Carnarvon MegaSurvey vary, which is also reflected in the relief of the seismic seafloor reflector. The surveys imaged in the western part of the figure show linear acquisition artefacts oriented approximately NW-SE. The waterdepth isolines are provided by a GEBCO one-minute-resolution bathymetry grid. The location of AGSO Survey 136 line 04 is indicated by a red dashed line and the section displayed in B by a solid red line. B) Seismic vertical reflectivity section of AGSO Survey 136 line 04 intersecting the sediment wave field SWF-B. C) Arbitrary vertical section through the Carnarvon MegaSurvey 3D dataset illustrating the local depression on which SWF-B can be observed.*

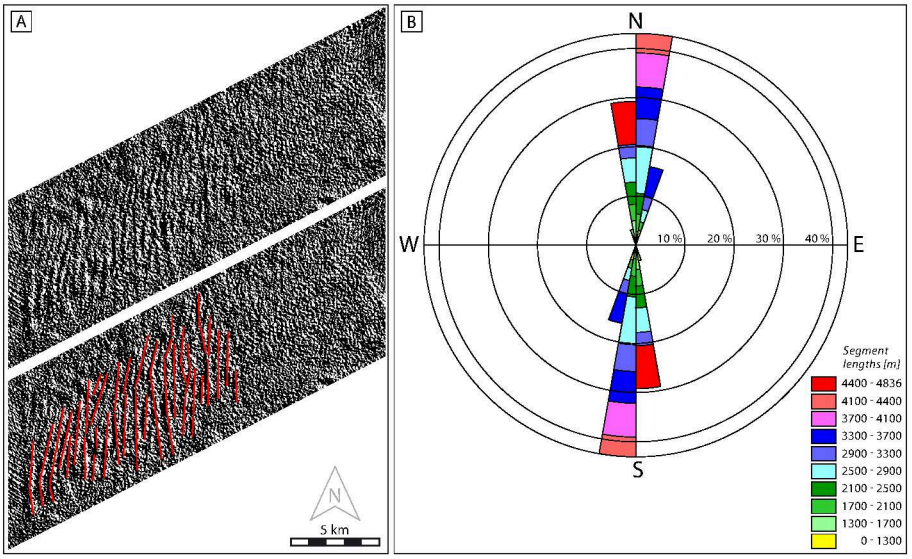

Figure 4.6: *A) The sediment wave field SWF-B shown on a shaded relief of the seismic seafloor reflector at maximum contrast to increase visibility of the crest orientations. The linear segments of sediment wave crests used for the evaluation of the general orientation are indicated in red. B) Rose diagram of the linear segments traced along the sediment wave crests weighted by segment length. The main crest orientation is approximately N (0-10°) and the average crest orientation is 3°.*

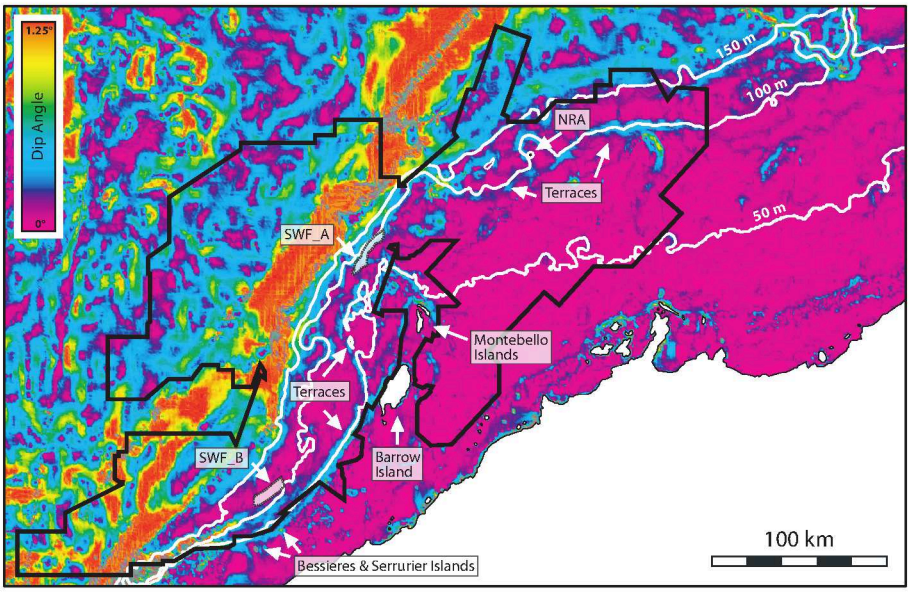

Figure 4.7: *A map showing the water depth and dip of the study area based on a GEBCO one-minuteresolution bathymetry grid. Dip values are capped at 1.25° to better illustrate the topography of the shelf, which in water depths of up to 150 m has a very low dip, seldom exceeding 0.25° with the exception of submarine terraces and areas close to the shore and slope. The terraces approximately follow the 50 and 100 m isolines. The shallow sections of the shelf (<150 m) decrease in width from east to west, with a local constriction in the region of the Montebello Islands.*

The main topographic features visible on the shallow shelf sections (<150 m water depth) of the data are morphological steps (Fig. 4.7). These terraces were first documented as submerged strandlines by Jones (1973) but have since also been interpreted as consisting in some places of drowned reef segments (Gallagher et al. 2014; Goktas et al. 2016). In the study area, submarine terraces can be observed to mainly occur around two levels of water depth, in around 50 m in the surroundings and to the west of the Montebello Islands, and in around 100 m further to the east (Fig. 4.7). Both observed sediment wave fields are located seaward in close proximity to one of these respective terraces (Fig. 4.4 & 4.7). With the exception of the terraces and areas close to the shore and near the slope, the seafloor topography of the shelf is relatively plane in water depths up to 200-250 m, with dip values seldom exceeding 0.25° (Fig. 4.7). The width of the shelf generally decreases from east to west; in respect to regions lying in 50-150 m water depth, the shelf width decreases from about 100 km north of the Dampier Archipelago to a few kilometres around North West Cape. In the region of the Montebello Islands the shelfal zone of 50-150 m water depth is also locally constricted through a terrace that extends northward towards the slope.

Sediment wave field SWF-A can be observed where the section of shelf between 50 and 150 m water depth is the narrowest (NW of the Montebello Islands; Fig. 4.7). This strait may influence local current patterns, as has been shown in the model of Condie and Andrewartha (2008) and likely poses as an obstruction or choke-point especially to along-slope oriented currents. The sediment wave field SWF-B is positioned on the shelf directly landward of a point where the general orientation of the shelf-break changes from N-S to NE-SW, north of the Serrurier and Bessieres Islands (Figs. 4.1 & 4.7), forming a landward concave bend possibly influencing along-slope oriented currents flowing along the shelf-break, e.g. the LC. The position of the observed sediment waves also coincides with the location of a shore-parallel (approximately NE-SW) oriented local depression, which has a relatively shallow expression on the modern seafloor due to sediment fill but is quite pronounced in underlying reflectors (Fig. 4.5C). Given these observations, it is very likely that the topography of the shelf plays a significant role for the development of both sediment wave fields.

4.5.3 Sedimentological Interpretation

On the NWS winnowing and transport of sediments is more common than their deposition (Dix 1989), and sediment movement appears to occur on the entire shelf (Jones 1973; James et al. 2004). Thus it seems unlikely that the observed sediment waves are relict bedforms.

The sediment around SWF-A (Fig. 4.4A) mainly consists of carbonate particles (>90%) that are on average mostly sand sized with no or a very small mud component. In the vicinity of the terraces, landward of the sediment wave field, the sediment contains increasing amounts of gravel, possibly owed to diagenetic cementation associated with the formation of the terraces. Sediments sampled in the area of SWF-B (Fig. 4.4B) are also mainly sand sized, but have a large mud component and very little gravel, a trend which appears to be inverted as the water depth decreases southeast of the sediment wave field towards the terraces, where increasing amounts of gravel and less mud sized grains were recorded (auSEABED database, Jenkins 2000). Increased mud concentrations in the vicinity of SWF-B likely reflect a higher proportion of aragonitic mud deposited during the initial sea-level rise after the Last Glacial Maximum, a higher contribution by pelagic mud (James et al. 2004), or finer grained sediment being trapped in the observed local depression. Although the sediment samples in terms of grain size show sand as the main component, the sediment waves are better visible on the data, i.e. have larger amplitudes, in the areas showing a higher mud content. Thus it may also be possible that the sediment waves of field SWF-B could be mudwaves instead of sandwaves. Mudwaves in general usually display lower crest heights and a wider spacing than sandwaves (Stow et al. 2009), a characteristic that is also evident when comparing SWF-B to SWF-A, where the observed sediment waves are interpreted as sandwaves.

For carbonate sediments the grain size usually is not sufficient to fully characterize the sediment mobility, as the grain-size weight relationship is not as linear as it is for siliciclastic sediments due to the varying density of different carbonate particles. Information on the surface-sediment facies of the NWS was compiled by James et al. (2004). Within these data, SWF-A is located close to the border of two facies zones indicating that seafloor sediments most likely consist of either mainly ooids and peloids (70-80%)

and relict intraclasts (20-30%), or alternatively mainly poorly sorted benthic foraminifera sands and gravels with a minor part (20-40%) of relict grains (James et al. 2004). SWF-B is, in turn, clearly located within the second of these facies zones. The data of James et al. (2004) thus shows that the observed bedforms have, depending on the facies zone either completely or at least partially, formed out of sediments that are not in equilibrium with the current depositional regime.

4.6 Discussion

The general magnitude of the flow velocity necessary to form the observed bedforms, which have a spacing between 200-600 m and a maximum height of 7.5 m, can be estimated using the bedform velocity matrix of Stow et al. (2009). According to this matrix the current velocity required to form sandwaves with wavelengths of 5-500 m and heights between 0.5-5 m lies at around 0.3-0.75 $\frac{m}{s}$. Bottom currents on the NWS may be induced by barotropic tides, internal tides and waves, storm waves caused by tropical cyclones and along-slope currents. Based on the size and spacing of the observed sediment waves and the predominant sediment grain size in the area, it is most likely that these bedforms developed transverse to the main current orientation (Stow et al. 2009). The alignment of the wave crests can thus be interpreted to indicate the approximate orientation of the locally dominating bottom-current direction. In the case of SWF-A, the crest alignment indicates two main flow orientations, a dominant E-W oriented flow and a secondary weaker NE-SW oriented flow (Fig. 4.3B). This bimodal distribution could either reflect two interfering regimes of bottom currents, for example tidal and storm induced currents or it may be due to the obstruction of local currents by the narrowing of the shelf below 50 m water depth resulting in more chaotic flow patterns. The crest alignments of SWF-B indicate dominantly E-W oriented bottom currents (Fig. 4.6B). It is hardly possible to further narrow down the dominant current orientations based on the crest symmetry, as an assessment would not be meaningful at the available resolution.

The model of Harris et al. (2000) indicates that swell waves in general may transport or suspend sediments in some regions of the study area and observations by James et al.

(2004) confirm this. The swell environment was nevertheless found to be highly variable, due to refraction and shoaling of the swell waves, but also through sheltering of the region by the North West Cape (Santala 2011). Since neither the strength nor the orientation of swell waves at the sediment wave sites can be quantified, their impact remains unclear. Based on Harris (1995) their general influence on sediment transport in the study area lies below that of tropical cyclones and most likely also below that of tidal currents whose influence is dominant further northeast along the NWS.

According to a study by Porter-Smith et al. (2004), in which the threshold exceedance for the re-suspension of local sediments in relation to tidal current speeds and significant wave heights was analyzed, the energy exerted by tidal waves does not suffice to mobilize sediments across most of the study area, with the exception of regions near the Montebello Islands and North West Cape (Figs. 4.1 & 4.7). Based on this, barotropic tides are unlikely to have played a significant role in the development of SWF-B, but remain a possible mechanism for SWF-A, which lies 60 km north of Barrow Island. A circulation model of the NWS by Condie and Andrewartha (2008) predicts considerable dissipation of current energy near the seafloor for the approximate location of SWF-A. Although the dominant orientation of tidal currents on the NWS is cross-shelf, the model also shows that near the coast and in the region of Barrow Island and the Montebello Islands (Figs. 4.1 & 4.7) the current patterns are strongly influenced by the local bathymetry (Condie and Andrewartha 2008). A figure shows clockwise bottom flows around the islands during spring tide (Condie and Andrewartha 2008, their figure 7A), which are oriented approximately towards the northeast in the area of SWF-A. Thus both the orientation and energy exerted by tidal flows near SWF-A appear relevant for the development of sediment waves, whereas this is not the case in the area of SWF-B.

A detailed analysis of the potential impact of internal waves and tides is difficult, as no direct current measurement or modelling dataset is available that illustrates the impact of internal waves directly in the region of the sediment wave fields. It has been shown however that the character of the internal waves and tides may change considerably over short distances as it strongly depends on the slope of the local bathymetry (e.g. Holloway 1985). This appears to be especially relevant in the case of SWF-B, seaward of which the shelf-break is much less pronounced than along the rest of the shelf, likely influencing

the local internal wave regime. Nevertheless it is possible to draw some parallels to the model of Van Gastel et al. (2009), which images the region around the NRA platform in similar water depths ca. 100 km east of SWF-A (Fig. 4.1). This model is based on in-situ measurements over 4 months and shows that large amplitude internal waves in the region of the NRA platform are generated in water depths of 400-600 m on the slope, move onshore and dissipate in water depths of 60 m (Van Gastel et al. 2009). An example shows that two large amplitude internal waves are generated, oriented 308° and 15°, which move towards the site of the NRA platform where they merge and change their orientation to approximately SE, roughly normal to the shore, before dissipating 30 km further landward in water depths of approximately 60 m (Van Gastel et al. 2009). A vertical profile of the internal wave shows current velocities along the internal wave beam of up to 0.6 $\frac{m}{s}$ and an increase in bottom currents where it reflects off the seafloor (Van Gastel et al. 2009). These data show that internal waves in the area can locally induce bottom currents strong enough to re-suspend and transport sediment. The general orientation of the described internal waves normal to the slope does not necessarily disqualify them in respect to the observed sediment wave fields, as the bottom currents induced may still have an along slope orientation (e.g. Cacchione et al. 2002), especially when the internal waves are oriented obliquely to the slope (Thorpe 1999; Zikanov and Slinn 2001). The impact of internal waves and tides however is strongest in the summer, and may wane during the winter due to weakened stratification of the shelf waters (James et al. 2004).

Tropical cyclones are assumed to be mainly responsible for inducing currents that transport sediments in the study area (Harris 1995). Despite their comparatively rare occurrence the energy expended during such an event may correspond to that of extended periods of fair-weather conditions (e.g. Swift and Thorne 1991) in addition to enabling sediment mobilization in greater water depths (Porter-Smith et al. 2004). Current measurements taken near the NRA platform show that the passage of a cyclone led to increased along-slope poleward directed flow (Van Gastel 2010). This matches the modelling results of Hearn and Holloway (1990), which show that tropical cyclones induce strong westward oriented currents on the inner shelf between the eye of the cyclone and the coast. An increase in along-slope oriented bottom currents would be relevant for the development of both observed sediment wave fields, although this would indicate long

periods of inactivity between the storm events if this was the main formation mechanism. The effect of tropical cyclones on the strength of the internal waves and tides in relationship to the observed sediment wave fields is hard to quantify, as amplification or damping depends on the path of the cyclone (Davidson and Holloway 2003).

The main large-scale along-slope currents on the NWS are the LC or its source waters derived from the ITF respectively. These are usually described as being strongest over the shelf edge (Godfrey 2001) or the slope (James et al. 2004), making their direct involvement into the development of the observed sediment waves unlikely. An involvement of the Ningaloo current also seems unlikely as both sediment wave sites are located seaward of the 50 m isobar (Pattiaratchi 2006).

The above discussion suggests that the sediment waves observed at SWF-A are most likely the result of tidal currents, which appear to be amplified through the local bathymetry. The site may furthermore be influenced by bottom currents induced by internal waves and tides, as well as through tropical cyclones. Of these mechanisms, tidal currents appear to be the most important for the generation of bedforms, as they are the most persistent, unlike the internal waves and tides whose influence weakens during the winter along with the local stratification and tropical cyclones which may only occur in the summer and are relatively isolated events by comparison. Internal waves and tides or tropical cyclones may of course nevertheless play a role, as the observed sediment waves are not regular and show many defects along their crests, possibly hinting at non-uniform flow orientations.

For the development of the sediment waves observed at SWF-B tidal currents can however most likely be ruled out, as predicted by the sediment threshold exceedence model of Porter-Smith et al. (2004). The potential impact of internal waves or tides is difficult to estimate without local current measurements or modelling data, since the shelf break where internal waves are generated in the area of the NRA platform (Van Gastel 2010) is much less pronounced seaward of SWF-B, probably leading to a differing, possibly weaker local internal wave climate. It is also interesting to note that in the vicinity of the NRA platform, where the occurrence and impact of internal waves on the seafloor have been documented (Van Gastel et al. 2009; Van Gastel 2010) no large scale sediment waves

could be observed on the data. This indicates that internal waves and tides alone can not be responsible for the development of the observed bedforms. As is the case for SWF-A, tropical cyclones occurring during the summer may very well also induce the necessary bottom currents in the region of SWF-B. Alternatively the sediment waves could also be interpreted as mudwaves that have formed from the poorly sorted sediments trapped by a relative depression in the seafloor. The latter option would explain the localized occurrence of the bedforms, while also requiring flows of lower intensity for their development. Given that little indications for strong currents at this site could be found in the literature, bottom currents capable of re-suspending and transporting finer grained sediments are reported to be ubiquitous on the shelf (Jones 1973; James et al. 2004). This interpretation could be corroborated by the reported mud content of the local sediment. Based on the crest orientation of the sediment waves, along-slope oriented currents including a possible shelfal extension of the LC, but also potential along-slope currents induced by tropical cyclones or internal waves could be relevant in this scenario.

Given the common occurrence of sediment waves on the shelf demonstrated by other studies (Jones 1973; James et al. 2004; Jones et al. 2009; Nichol and Brooke 2011; Belde et al. 2015), it is remarkable that only two fields of sediment waves could be observed within the large area of shelf imaged by the Carnarvon MegaSurvey. The resolution of the 3D seismic reflection data is certainly important in this respect, because despite their comparatively large size, the sediment waves are also quite close to the limit of features that may be detected on medium-resolution seismic data, hiding smaller bedforms. It may also be possible that in some areas of the data bedforms become masked by seismic artefacts where the seafloor reflection is less distinct, usually in shallower water depths. Keeping this in mind, the observed sediment waves are most likely not the only bedforms, but nevertheless the largest to have formed on the studied section of shelf. Bedforms with similar characteristics, e.g. sediment waves or dunes, have also been observed southwest of the study area on the Australian west coast and further northeast along the Australian NWS (James et al. 2004; Jones et al. 2009; Nichol and Brooke 2011; Belde et al. 2015). Southwest of the study area, on the Australian west coast off Point Cloates, barchan sandwaves with crest heights of 3-4 m and a spacing of approximately 140 m were described in a water depth between 150-185 m (Nichol and Brooke 2011).

These were attributed to the LC, possibly augmented by the Ningaloo current (Nichol and Brooke 2011). Northeast of the study area, along the NWS, sandwaves with crest heights between 4-12 m in water depths around 70 m were documented and interpreted as deposits most likely formed by internal waves (James et al. 2004). Near the Rowley Shoals, sandwaves with heights of up to 9.2 m were documented in water depths of 95-120 m which were primarily associated with tidal currents (Jones et al. 2009). Further northeast in the Browse Basin sediment waves with crest heights of up to 10 m in water depths between 250-1000 m were observed and attributed to the influence of internal waves or tides due to the large water depths (Belde et al. 2015). This conveys the general impression that on the Australian west coast the LC is regarded as the most important factor for the development of large-scale bedforms, whereas on the central NWS tides or internal waves and tides, depending on the water depth, are favoured in this respect.

4.7 Conclusions

The isolated occurrence of only two large scale sediment wave fields within the extensive study area indicates that specific conditions in respect to the interplay of topography, sediment grain size and local current regime are necessary for their development. The sediment waves observed at SWF-A have most likely formed due to the diversion of tidal flows around the Barrow and Montebello islands leading to increased bottom current strengths in the area. During the summer additional bottom currents may also be induced by internal waves and tropical cyclones. The sediment waves observed at SWF-B have formed within a shallow seafloor depression, in a region characterised by poorly sorted sediment dominantly consisting of carbonate sand and mud. These sediment waves were likely formed by bottom currents induced by tropical cyclones or less energetic along-slope oriented currents.

The sediment at SWF-A is dominated by ooids, peloids and other stranded carbonate grains that formed in shallow water during the initial sea-level rise after the last glacial low stand. These grains are now incorporated into sand waves that have formed during the Holocene sea-level highstand in water depths greater than the fair weather wave

base. The fact that the sedimentary bedforms are out of equilibrium with their component carbonate grains might be a common phenomenon on high energy, ocean facing carbonate ramps and has to be taken into account when interpreting the fossil record.

4.8 Acknowledgements

We thank Petroleum Geo-Services (PGS) and Geoscience Australia for access to the seismic reflection data. IHS is gratefully acknowledged for providing the KINGDOM software under an Academic User License Agreement. Schlumberger is acknowledged for providing the software Petrel. Conny Lutter is particularly thanked for her help in acquiring scientific literature. This study is a spin-off of project RE 2697/3-1 funded by the Deutsche Forschungsgemeinschaft (DFG). J. Belde was funded by DFG project BA 2136/4-1.

Chapter 5

Comprehensive summary of conclusions

For the analysis of structures on the modern seafloor and in the shallow subsurface performed in preparation of this thesis, the use of 2D and 3D seismic-reflection data proved ideal. This type of data allowed for large study areas while also providing ample resolution, allowing a detailed study of the shelf/slope-environment. An important aspect, as one of the most central roles in the development of the bedforms and reef-rimmed carbonate platforms analyzed appears to be played by the antecedent topography, which in turn is strongly associated with the local tectonic regime. A further control is placed on the local sedimentological environment by the regime of oceanic currents, as evidenced by the prominent switch to drift sedimentation around 6 Ma.

One of the most spectacular results of the research presented was the documentation of numerous reef-rimmed carbonate platforms in the subsurface of the Browse Basin on an extensive dataset consisting of 2D and 3D seismic-reflection surveys supported by borehole data. Through data gained from microfossil analysis and Sr-dating of sidewall cores a chronostratigraphic framework was constructed, placing the oldest documented carbonate platform into the Oligocene (34.03 – 27.8 Ma). This structure can be interpreted either as a reef-rimmed platform or a giant bryozoan reef-mound complex located on the topsets of a heterozoan ramp. After this period, an interval followed in which no further reef development could be observed until around 17.54 – 16.38 Ma, when continuous reef development in the area began. In the Miocene, between 15.1 – 9.83 Ma, a major NE-SW oriented reef-rimmed platform belt showing remarkably little variation along its length

developed, extending over 500 km across the Browse Basin. This platform belt was superseded around 11.1 – 9.83 Ma by numerous isolated reefs. The youngest of these reefs may have persisted until ca. 6.14 – 4.08 Ma in the northernmost study area (Torosa) but widespread reef development in general ceased around 6.14 Ma in the study area, coinciding with the onset of current-driven drift sedimentation. The relationship of modern reefs such as the North Scott Reef and the Seringapatam Reef to the studied reef systems remains unclear.

The documented reef-rimmed carbonate platforms show significant lateral differences in their distribution and architecture between the north (Torosa) and the south (Barcoo subbasin) of the study area. While the platforms in the north are thick and massive, with rather stationary seaward terminations, the platforms in the south are generally thinner and more widely distributed across the shelf. After 15 Ma the reef-rimmed carbonate platforms also exhibit an internal northward thickening trend, most likely indicating the onset of a downward bending of the northern part of the Browse Basin. Using the observed reefs as palaeo-waterdepth indicators, subsidence rates for the south (64 $\frac{m}{Ma}$) and the north (125 $\frac{m}{Ma}$) of the study area can be calculated. The lower subsidence rates in the south may have more often resulted in periods of inhibiting conditions, forcing frequent reef migration and resulting in thinner, more widespread reef development. The higher rates of subsidence in the north in contrast likely damped the influence of eustatic variations, resulting in thicker, comparatively fixed reef systems. Miocene reef development in the study area appeared to be strongly controlled by the antecedent topography, as evidenced by the preferential reef development on the topsets of underlying clinoforms and the restriction imposed on progradation by the slope angles of the underlying systems.

Another key result of the research in the Browse Basin demonstrated the possibility to map various large-scale modern bedforms such as sediment waves, furrows and elongate sediment ridges on 3D seismic reflection data, both on the modern seafloor and down to 500 ms TWT into the sedimentary record. The locations of the observed sediment wave fields can generally be associated with the occurrence of morphological irregularities on the seafloor, namely submarine terrace escarpments, fault scarps, incised channels and mass wasting deposits. The extent, orientation, morphology and seismic signature of the sediment waves vary accordingly, as these areas of pronounced relief appear to provide

shelter for sediments in a regime apparently dominated by sediment erosion and transport, as indicated by the furrows and sediment ridges occupying the plane portions of the shelf. It is most likely that the observed large-scale bedforms have formed under present-day environmental conditions in their current locations. The observed sediment waves were most likely formed by bottom flows induced by the activity of internal waves, as these appear the most probable mechanism capable of moving sand sized sediments in the comparatively large water depths, a grain size approximation inferred from the crest height and spacing of the bedforms. The orientation of internal waves in the greater study area also agrees with the crest orientations of the sediment waves. Due to the similarity between the modern and buried sediment wave fields in respect to their morphology and orientation, it is likely that analogous processes have persisted in the study area since the post-Messinian, an approximate time-frame established by the oldest buried sediment waves observed.

Finally, the research on sediment waves on the modern seafloor of the northern Carnarvon Basin showed that on a comparatively large study area, only two sediment wave fields could be observed, much fewer than in the Browse Basin. This indicates that the interplay of topography, sediment grain size and local currents in the northern Carnarvon Basin is not as favourable for the development of large scale sediment waves. Of the observed sediment wave fields, SWF-A most likely formed as a result of tidal flows that are diverted by the Barrow and Montebello islands, inducing increased bottom currents in the area. Additional bottom currents in the area may also be induced by internal waves and tropical cyclones during the summer. SWF-B, in contrast, developed on a shallow seafloor depression, most likely through bottom currents induced by tropical cyclones if the sediment waves are composed of coarser grains, or alternatively by less energetic along-slope currents for finer grains. The local sediment composition at SWF-A consists mainly of ooids, peloids and other relict carbonate particles deposited in a shallow-water environment after the last glacial low-stand, whereas the observed bedforms developed in water depths below the fair weather wave-base during the Holocene sea-level high-stand. As the sedimentary bedforms are clearly out of equilibrium with their component carbonate particles, this example serves to demonstrate pitfalls when interpreting the origin of bedforms in the fossil record of high-energy ocean facing carbonate ramps.

Chapter 6

Outlook

The work on reef rimmed carbonate platforms in the Browse Basin presented could be expanded or continued in the following manner: a major improvement could be made by acquiring and incorporating more age information on the interval in which the carbonate platforms are observed. This interval was only sampled and studied in comparatively few of the wells in the study area, a circumstance that is most likely owed to the technical and financial considerations involved in drilling operations in the associated water depths. With more microfossil and Sr-age information, the chronostratigraphic framework could be further refined and, if the respective data sites are well placed, made more robust. A better age determination of the phases of reef development would allow a more precise delineation of the different reef generations and reconstruction of their palaeo-environment. Given the availability of age information in the respective areas it would also be possible to expand the study area further north along the NWS (BR98 survey) and also further landward (Northern Browse and Firetail surveys). In both areas, multiple carbonate platforms are visible on the seismic data but as of yet could not be integrated meaningfully into the present work. A more detailed knowledge of the timing of local tectonics (BFZ, Buffon fault?) would help to refine the rates of subsidence calculated for the area and aid in better understanding the antecedent topography during the various intervals of reef development. Additional controls on reef development such as the possible influence of changing oceanic currents (i.e. change of the Indonesian Throughflow by closure of the SE Asian Gateway) on water temperatures, salinity and nutrients during the respective time interval also require further investigation.

The understanding of the depositional environment in both, the Browse and Carnarvon Basins could be further improved by gathering additional field data. Precise grab samples would help to better characterise the local sediment, giving a clearer picture of the flow velocities necessary for sediment entrainment and transport. Near-seafloor current-meter measurements at the individual sediment wave fields could record the actual current velocities and directions, as well as possible seasonal variations. This would greatly help in understanding the local current regime and aid in differentiating and identifying the individual mechanisms influencing it. High-resolution seismic reflection 2D and 3D surveys could provide further information on the geometry and internal bedding of the sediment waves. More details on their geometry would allow precise slope-angle determination and a better description of the symmetry of the sediment waves, which could be used as indicators for the mode of sediment transport across the bedforms; this would ultimately enable an analysis of the flow direction across the bedforms, indicating if it was/is primarily unidirectional, or if a reverse flow is present.

Bibliography

Aghsaee, P., L. Boegman, and K. G. Lamb (2010). Breaking of shoaling internal solitary waves. *Journal of Fluid Mechanics 659*, 289–317.

AGSO Browse Basin Project Team (1997). *Browse Basin High Resolution Study, Interpretation Report*, Volume Record 1997/38. Australian Geological Survey Organisation.

Apel, J. R. (2002). Oceanic internal waves and solitons. In C. R. Jackson and J. R. Apel (Eds.), *An Atlas of Internal Solitary Waves*, pp. 1–40. Global Ocean Associates Prepared for Office of Naval Research - Code 322 PO.

Apthorpe, M. (1988). Cainozoic depositional history of the North West Shelf. In P. G. Purcell and R. R. Purcell (Eds.), *The North West Shelf, Australia*, pp. 55–84. Perth: Petroleum Exploration Society of Australia Symposium.

Audley-Charles, M. G. (2004). Ocean trench blocked and obliterated by Banda forearc collision with Australian proximal continental slope. *Tectonophysics 389*, 65–79.

Bachtel, S. L., H. W. Posamentier, and T. P. Gerber (2011). Seismic geomorphology and stratigraphic evolution of a Tertiary-aged isolated carbonate platform system, Browse Basin, North West Shelf of Australia - Part II. In L. J. Wood, T. T. Simo, and N. C. Rosen (Eds.), *Seismic imaging of depositional and geomorphic systems: 30th annual GSSEPM Foundation Bob F. Perkins research conference 2010; Houston, Texas, USA, 5-8 December 2010*, pp. 115–135. Red Hook, NY: Curran.

Back, S., C. Höcker, M. B. Brundiers, and P. A. Kukla (2006). Three-dimensional-seismic coherency signature of Niger Delta growth faults: integrating sedimentology and tectonics. *Basin Research 18*(3), 323–337.

Baines, P. G. (1981). Satellite observations of internal waves on the Australian North-west Shelf. *Australian Journal of Marine and Freshwater Research 32*(3), 457–463.

Baines, P. G. (1982). On internal tide generation models. *Deep-Sea Research Part A. Oceanographic Research Papers 29*(3A), 307–338.

Baker, C., A. Potter, M. Tran, and A. D. Heap (2008). *Geomorphology and Sedimentology of the Northwest Marine Region of Australia: Geoscience Australia, Record 2008/07*. Canberra: Geoscience Australia.

Belde, J., S. Back, and L. Reuning (2015). Three-dimensional seismic analysis of sediment waves and related geomorphological features on a carbonate shelf exposed to large amplitude internal waves, Browse Basin region, Australia. *Sedimentology 62*(1), 87–109.

Bernardel, G. (2005). Report on Ashmore Platform seeps and signatures focussed seismic interpretation study. *Geoscience Australia, unpublished*.

Betzler, C., S. Lindhorst, T. Lüdmann, J. Reijmer, G. Eberli, J. Möbius, C. Hübscher, and M95 Shipboard Scientific Party (2013). Re-evaluation of sedimentation patterns at Bahamian carbonate slopes.

Bourgault, D., D. E. Kelley, and P. S. Galbraith (2008). Turbulence and boluses on an internal beach. *Journal of Marine Research 66*(5), 563–588.

Bourget, J., R. B. Ainsworth, G. Backé, and M. Keep (2012). Tectonic evolution of the northern Bonaparte Basin: impact on continental shelf architecture and sediment distribution during the Pleistocene. *Australian Journal of Earth Sciences 59*(6), 877–897.

Bourget, J., R. B. Ainsworth, and S. Thompson (2014). Seismic stratigraphy and geomorphology of a tide or wave dominated shelf-edge delta (NW Australia): Process-based classification from 3D seismic attributes and implications for the prediction of deep-water sands. *Marine and Petroleum Geology 57*, 359–384.

Brink, K. H., F. Bahr, and R. K. Shearman (2007). Alongshore currents and mesoscale variability near the shelf edge off northwestern Australia. *Journal of Geophysical Research 112*(C5).

Cacchione, D. A., L. F. Pratson, and A. S. Ogston (2002). The shaping of continental slopes by internal tides. *Science 296*(5568), 724–727.

Cane, M. and P. Molnar (2001). Closing of the Indonesian seaway as a precursor to east African aridification around 3$\pm$4 million years ago. *Nature 411*, 157–162.

Cathro, D. L., J. A. Austin, and G. D. Moss (2003). Progradation along a deeply submerged Oligocene-Miocene heterozoan carbonate shelf: How sensitive are clinoforms to sea level variations? *AAPG Bulletin 87*(10), 1547–1574.

Chaproniere, G. C. H., S. Shafik, E. M. Truswell, M. K. MacPhail, and A. D. Partridge (1996). Cainozoic (Chart 12). In G. C. Young and J. R. Laurie (Eds.), *An Australian Phanerozoic Timescale*, pp. 175–186. Melbourne: Oxford University Press.

Collins, L. B. (2011). Geological setting, marine geomorphology, sediments and oceanic shoals growth history of the Kimberley region. *Journal of the Royal Society of Western Australia 94*(2), 89–105.

Condie, S. and J. Andrewartha (2008). Circulation and connectivity on the Australian north west shelf. *Continental Shelf Research 28*(14), 1724–1739.

Condie, S., J. Andrewartha, J. Mansbridge, and J. Waring (2006). *Modelling Circulation and Connectivity on Australia's North West Shelf: Technical Report No. 6, North West Shelf Joint Environmental Management Study*. CSIRO and Department of Environment.

Correa, T. B., G. P. Eberli, M. Grasmueck, J. K. Reed, and A. M. Correa (2012). Genesis and morphology of cold-water coral ridges in a unidirectional current regime. *Marine Geology 326-328*, 14–27.

Craig, P. D. (1988). A numerical model study of internal tides on the Australian northwest shelf. *Journal of Marine Research 46*(1), 59–76.

CSIRO (2004). Indonesian Throughflow: CSIRO Marine Research Fact Sheets, No. 64.

Czarnota, K., M. J. Hoggard, N. White, and J. Winterbourne (2013). Spatial and temporal patterns of Cenozoic dynamic topography around Australia. *Geochemistry, Geophysics, Geosystems 14*(3), 634–658.

Davidson, F. J. M. and P. E. Holloway (2003). A study of tropical cyclone influence on the generation of internal tides. *Journal of Geophysical Research 108*(C3).

DiCaprio, L., R. D. Müller, and M. Gurnis (2010). A dynamic process for drowning carbonate reefs on the northeastern Australian margin. *Geology 38*(1), 11–14.

Dix, G. R. (1989). High-energy, inner shelf carbonate facies along a tide-dominated non-rimmed margin, northwestern Australia. *Marine Geology 89*(3-4), 347–362.

Dix, G. R., N. P. James, T. K. Kyser, Y. Bone, and L. B. Collins (2005). Genesis and dispersal of carbonate mud relative to late Quaternary sea-level change along a distally-steepened carbonate ramp (northwestern shelf, Western Australia). *Journal of Sedimentary Research 75*(4), 665–678.

Dunlap, D. B., L. J. Wood, and L. G. Moscardelli (2013). Seismic geomorphology of early North Atlantic sediment waves, offshore northwest Africa. *Interpretation 1*(1), SA75–SA91.

Etheridge, M. A. and G. W. O'Brien (1994). Structural and tectonic evolution of the Western Australian margin basin system. *Petroleum Exploration Society of Australia Journal 22*, 45–64.

Flood, R. D. (1981). Distribution, morphology, and origin of sedimentary furrows in cohesive sediments, Southampton Water. *Sedimentology 28*(4), 511–529.

Flood, R. D. (1983). Classification of sedimentary furrows and a model for furrow initiation and evolution. *Geological Society of America Bulletin 94*(5), 630–639.

Folk, R. L. (1965). *Petrology of sedimentary rocks*. Austin, Texas: Hemphill's.

Frakes, L. A. (1999). Evolution of Australian environments. In A. Orchard (Ed.), *Flora of Australia*, Volume Vol. 1, pp. 163–203. Melbourne and Australia: CSIRO Publishing.

Frakes, L. A., J.-L. Probst, and W. Ludwig (1994). Latitudinal distribution of paleotemperature on land and sea from early Cretaceous to middle Miocene. *Comptes Rendus de L'Acadèmie des Science Paris Series 2*, 1209–1218.

Gallagher, S. J., M. W. Wallace, P. W. Hoiles, and J. M. Southwood (2014). Seismic and stratigraphic evidence for reef expansion and onset of aridity on the Northwest Shelf of Australia during the Pleistocene. *Marine and Petroleum Geology 57*, 470–481.

Gallagher, S. J., M. W. Wallace, C. L. Li, B. Kinna, J. T. Bye, K. Akimoto, and M. Torii (2009). Neogene history of the West Pacific Warm Pool, Kuroshio and Leeuwin currents. *Paleoceanography 24*(1).

Gerkema, T., F.-P. A. Lam, and L. R. Maas (2004). Internal tides in the Bay of Biscay: conversion rates and seasonal effects. *Deep Sea Research Part II: Topical Studies in Oceanography 51*(25-26), 2995–3008.

Godfrey, J. S. and K. R. Ridgway (1985). The large-scale environment of the poleward-flowing Leeuwin Current, Western Australia: Longshore steric height gradients, wind stresses and geostrophic flow. *Journal of Physical Oceanography 15*(5), 481–495.

Godfrey, S. (2001). Indonesian Throughflow and Leeuwin Current. In J. H. Steele, S. A. Thorpe, and K. K. Turekian (Eds.), *Encyclopedia of Ocean Sciences*, pp. 1309–1313. Elsevier.

Goktas, P., J. A. Austin, C. S. Fulthorpe, and S. J. Gallagher (2016). Morphologies and depositional/erosional controls on evolution of Pliocene-Pleistocene carbonate platforms: Northern Carnarvon Basin, Northwest Shelf of Australia. *Continental Shelf Research 124*, 63–82.

Gordon, A., J. Sprintall, H. Van Aken, D. Susanto, S. Wijffels, R. Molcard, A. Ffield, W. Pranowo, and S. Wirasantosa (2010). The Indonesian Throughflow during 2004-2006 as observed by the INSTANT program. *Dynamics of Atmospheres and Oceans 50*(2), 115–128.

Gordon, A. L. (2005). Oceanography of the Indonesian Seas and their throughflow. *Oceanography 18*(4), 14–27.

Gordon, A. L. and R. A. Fine (1996). Pathways of water between the Pacific and Indian oceans in the Indonesian seas. *Nature 379*(6561), 146–149.

Gorter, J. D., J. P. Rexilius, S. L. Powell, and S. W. Bayford (2002). Late early to mid Miocene patch reefs, Ashmore Platform, Timor Sea - evidence from 2D and 3D seismic surveys and petroleum exploration wells. In M. Keep and S. J. Moss (Eds.), *The Sedimentary Basins of Western Australia 3*, pp. 355–376. Perth: Petroleum Exploration Society of Australia Symposium.

Gourlan, A. T., L. Meynadier, and C. J. Allègre (2008). Tectonically driven changes in the Indian Ocean circulation over the last 25 Ma: Neodymium isotope evidence. *Earth and Planetary Science Letters 267*(1-2), 353–364.

Gradstein, F., J. Ogg, G. M. Schmitz, and G. M. Ogg (Eds.) (2012). *The Geologic Time Scale 2012*. Oxford, UK: Elsevier.

Grasmueck, M., G. P. Eberli, D. A. Viggiano, T. Correa, G. Rathwell, and J. Luo (2006). Autonomous underwater vehicle (AUV) mapping reveals coral mound distribution, morphology, and oceanography in deep water of the Straits of Florida. *Geophysical Research Letters 33*(23).

Hall, R. (2002). Cenozoic geological and plate tectonic evolution of SE Asia and the SW Pacific: computer-based reconstructions, model and animations. *Journal of Asian Earth Sciences 20*, 353–431.

Hall, R. (2009). Southeast Asia's changing palaeogeography. *Blumea - Biodiversity, Evolution and Biogeography of Plants 54*(1), 148–161.

Hall, R. (2011). Australia-SE Asia collision: plate tectonics and crustal flow. *Geological Society, London, Special Publications 355*(1), 75–109.

Hardenbol, J., J. Thierry, M. B. Farley, T. Jacquin, P.-C. de Graciansky, and P. R. Vail (1998). Mesozoic and Cenozoic sequence chronostratigraphic framework of European basins. In P.-C. Graciansky, J. Hardenbol, T. Jacquin, and P. R. Vail (Eds.), *Mesozoic-Cenozoic Sequence Stratigraphy of European Basins*, Volume 60, pp. 3–13. Tulsa: SEPM Special Publication.

Harris, P. T. (1995). Marine geology and sedimentology of the Australian continental shelf. In L. P. Zann and P. Kailola (Eds.), *The State of the Marine Environment. Report for Australia. Technical Annex 1: The Marine Environment*, pp. 11–23. Canberra: Department of the Environment, Sport and Territories.

Harris, P. T., R. Smith, O. Andersen, R. Coleman, and D. Greenslade (2000). *GEOMAT - Modelling of Continental Shelf Sediment Mobility in Support of Australia's Regional Marine Planning Process*. AGSO Record 2000/41. Australian Geological Survey Organisation.

Harrowfield, M., J. Cunneen, M. Keep, and W. Crowe (2003). Early-stage orogenesis in the Timor Sea region, NW Australia. *Journal of the Geological Society 160*(6), 991–1001.

Heap, A. D. and P. T. Harris (2008). Geomorphology of the Australian margin and adjacent seafloor. *Australian Journal of Earth Sciences 55*(4), 555–585.

Hearn, C. J. and P. E. Holloway (1990). A three-dimensional barotropic model of the response of the Australian North West Shelf to tropical cyclones. *Journal of Physical Oceanography 20*, 60–80.

Heine, C., R. D. Müller, B. Steinberger, and L. DiCaprio (2010). Integrating deep Earth dynamics in paleogeographic reconstructions of Australia. *Tectonophysics 483*(1-2), 135–150.

Holloway, P. E. (1983a). Internal tides on the Australian North-west Shelf: A preliminary investigation. *Journal of Physical Oceanography 13*(8), 1357–1370.

Holloway, P. E. (1983b). Tides on the Australian North West Shelf. *Australian Journal of Marine and Freshwater Research 34*, 213–230.

Holloway, P. E. (1984). On the semidiurnal internal tide at a shelf-break region on the Australian North West Shelf. *Journal of Physical Oceanography 14*(11), 1787–1799.

Holloway, P. E. (1985). A comparison of semidiurnal internal tides from different bathymetric locations on the Australian North West Shelf. *Journal of Physical Oceanography 15*, 240–251.

Holloway, P. E. (1987). Internal hydraulic jumps and solitons at a shelf break region on the Australian North West Shelf. *Journal of Geophysical Research 92*(C5), 5405–5416.

Holloway, P. E. (1994). Observations of internal tide propagation on the Australian North West Shelf. *Journal of Physical Oceanography 24*, 1706–1716.

Holloway, P. E. (1995). Leeuwin Current observations on the Australian North West Shelf, May-June 1993. *Deep Sea Research Part I: Oceanographic Research Papers 42*(3), 285–305.

Holloway, P. E. (2001). A regional model of the semidiurnal internal tide on the Australian North West Shelf. *Journal of Geophysical Research 106*(C9), 19625–19638.

Holloway, P. E., E. Pelinovsky, T. Talipova, and B. Barnes (1997). A nonlinear model of internal tide transformation on the Australian North West Shelf. *Journal of Physical Oceanography 27*, 871–896.

Jackson, C. R., J. C. B. da Silva, and G. Jeans (2012). The generation of nonlinear internal waves. *Oceanography 25*(2), 108–123.

James, N. P., Y. Bone, T. K. Kyser, G. R. Dix, and L. B. Collins (2004). The importance of changing oceanography in controlling late Quaternary carbonate sedimentation on a high-energy, tropical, oceanic ramp: north-western Australia. *Sedimentology 51*(6), 1179–1205.

Jenkins, C. J. (2000). Generation of seafloor sediment griddings for the UTAS-AGSO shelf sediment mobility project: University of Sydney Ocean Science Institute Report v. 89. pp. 1–12.

Jones, A. T., J. M. Kennard, G. A. Logan, E. Grosjean, and J. Marshall (2009). Fluid expulsion features associated with sand waves on Australia's central North West Shelf. *Geo-Marine Letters 29*(4), 233–248.

Jones, H. A. (1971). Late cenozoic sedimentary forms on the northwest Australian continental shelf. *Marine Geology 10*(4), M20–M26.

Jones, H. A. (1973). *Marine Geology of the Northwest Australian Shelf*, Volume 136 of *Geology and Geophysics Bulletin*. Canberra: Bureau of Mineral Resources.

Karas, C., D. Nürnberg, R. Tiedemann, and D. Garbe-Schönberg (2011). Pliocene Indonesian Throughflow and Leeuwin Current dynamics: Implications for Indian Ocean polar heat flux. *Paleoceanography 26*(2).

Katsumata, K. (2006). Tidal stirring and mixing on the Australian North West Shelf. *Marine and Freshwater Research 57*(3), 243–254.

Keep, M., A. Bishop, and I. Longley (2000). Neogene wrench reactivation of the Barcoo Sub-basin, northwest Australia: implications for Neogene tectonics of the northern Australian margin. *Petroleum Geoscience 6*, 211–220.

Keep, M. and D. W. Haig (2010). Deformation and exhumation in Timor: Distinct stages of a young orogeny. *Tectonophysics 483*(1-2), 93–111.

Keep, M. and M. Harrowfield (2008). Elastic flexure and distributed deformation along Australia's North West Shelf: Neogene tectonics of the Bonaparte and Browse Basins. *Geological Society, London, Special Publications 306*(1), 185–200.

Keep, M., M. Harrowfield, and W. Crowe (2007). The Neogene tectonic history of the North West Shelf, Australia. *Exploration Geophysics 38*(3), 151–174.

Kemp, D. B., P. M. Sadler, and G. Della Porta (2014). Climatic and eustatic signals in a global compilation of shallow marine carbonate accumulation rates. *Sedimentology 61*(5), 1286–1297.

Kennard, J. M., I. Deighton, D. Ryan, D. S. Edwards, and C. J. Boreham (2004). Subsidence and thermal history modelling: New insights into hydrocarbon expulsionfrom multiple petroleum systems in the Browse Basin. In G. Ellis, P. Baillie, and T. Munson (Eds.), *Timor Sea Petroleum Geoscience*, pp. 411–435. Northern Territory Geological Survey.

Kennett, J. P., G. Keller, and M. S. Srinivasan (1985). Miocene planktonic foraminiferal biogeography and paleoceanographic development of the lndo-pacific region. In J. P. Kennett (Ed.), *The Miocene Ocean: Paleoceanography and Biogeography*, Volume 163, pp. 197–236. Geol. Soc. Am. Mem.

Klymak, J. M. and J. N. Moum (2003). Internal solitary waves of elevation advancing on a shoaling shelf. *Geophysical Research Letters 30*(20).

Kreemer, C., W. E. Holt, S. Goes, and R. Govers (2000). Active deformation in eastern Indonesia and the Philippines from GPS and seismicity data. *Journal of Geophysical Research 105*(B1), 663–680.

Kuhnt, W., M. Blümel, R. Boch, K. T. Dewi, F. da Costa Monteiro, A. Dürkop, T. Hanebuth, U. Heidemann, A. Holbourne, Z. Jian, S. van der Kaars, H. Kawamura, H. Kawohl, D. Nürnberg, B. Opdyke, A. Petersen, M. Regenberg, Y. Rosenthal, C. Rühlemann, A. Sadekov, B. Salomon, J. Tian, J. Xu, and R. Zuraida (2006). Cruise report sonne-185 "Variability of the Indonesian Throughflow and Australasian climate history of the last 150 000 years (VITAL)".

Kuhnt, W., A. Holbourn, R. Hall, M. Zuvela, and R. Kaese (2004). Neogene history of the Indonesian Throughflow. *Geophysical Monograph 149*, 299–320.

Kurup, N. V., S. Shi, Z. Shi, W. Miao, and L. Jiang (2011). Study of nonlinear internal waves and impact on offshore drilling units. In *ASME 2011 30th International Conference on Ocean, Offshore and Arctic Engineering*, Volume Volume 1: Offshore Technology; Polar and Arctic Sciences and Technology, pp. 831–840. Rotterdam and The Netherlands.

Langhi, L., N. B. Ciftci, and G. D. Borel (2011). Impact of lithospheric flexure on the evolution of shallow faults in the Timor foreland system. *Marine Geology 284*(1-4), 40–54.

Lesshafft, L., B. Hall, E. Meiburg, and B. Kneller (2011). Deep-water sediment wave formation: linear stability analysis of coupled flow/bed interaction. *Journal of Fluid Mechanics 680*, 435–458.

Lim, K., G. N. Ivey, and R. I. Nokes (2008). The generation of internal waves by tidal flow over continental shelf/slope topography. *Environmental Fluid Mechanics 8*(5-6), 511–526.

Lourensz, R. S. (1981). *Tropical cyclones in the Australian region, July 1909 to June 1980* (Revised edition). Canberra: Australian Govt. Pub. Service.

Lowe, D. R. (1982). Sediment gravity flows: II Depositional models with special reference to the deposits of high-density turbidity currents. *Journal of Sedimentary Research 52*(1), 279–297.

Malinverno, A., W. B. F. Ryan, G. Auffret, and G. Pautot (1988). Sonar images of the path of recent failure events on the continental margin off Nice, France. *Special Papers of the Geological Society of America 229*, 59–79.

McArthur, J. M., R. J. Howarth, and G. A. Shields (2012). Strontium isotope stratigraphy. In F. Gradstein, J. Ogg, G. M. Schmitz, and G. M. Ogg (Eds.), *The Geologic Time Scale 2012*, pp. 127–144. Oxford, UK: Elsevier.

McGowran, B., G. R. Holdgate, Q. Li, and S. J. Gallagher (2004). Cenozoic stratigraphic succession in southeastern Australia. *Australian Journal of Earth Sciences 51*(4), 459–496.

McNeill, D. F. (2005). Accumulation rates from well-dated late Neogene carbonate platforms and margins. *Sedimentary Geology 175*(1-4), 73–87.

Molcard, R., M. Fieux, and A. G. Ilahude (1996). The Indo-pacific throughflow in the Timor Passage. *Journal of Geophysical Research: Oceans 101*(C5), 12411–12420.

Moss, G. D., D. L. Cathro, and J. A. Austin (2004). Sequence biostratigraphy of prograding clinoforms, northern Carnarvon Basin, Western Australia: a proxy for variations in Oligocene to Pliocene global sea level? *PALAIOS 19*, 206–226.

Müller, R. D., D. Mihut, and S. Baldwin (1998). A new kinematic model for the formation and evolution of the Northwest and West Australian margin. In P. G. Purcell and R. R. Purcell (Eds.), *The Sedimentary Basins of Western Australia 2*, pp. 55–72. Perth: Petroleum Exploration Society of Australia Symposium.

Munk, W. H., G. R. Miller, F. E. Snodgrass, and N. F. Barber (1963). Directional recording of swell from distant storms. *Philosophical Transactions of the Royal Society of London. Series A, Mathematical and Physical Sciences 255*(1062), 505–584.

Nash, J. D., E. L. Shroyer, S. M. Kelly, M. E. Inall, T. F. Duda, M. D. Levine, N. L. Jones, and R. C. Musgrave (2012). Are any coastal internal tides predictable? *Oceanography 25*(2), 80–95.

Nichol, S. L. and B. P. Brooke (2011). Shelf habitat distribution as a legacy of late Quaternary marine transgressions: A case study from a tropical carbonate province. *Continental Shelf Research 31*(17), 1845–1857.

Pattiaratchi, C. (2006). Surface and sub-surface circulation and water masses off Western Australia. *Bulletin of the Australian Meteorological and Oceanographic Society 19*, 95–104.

Pomar, L., M. Morsilli, P. Hallock, and B. Bádenas (2012). Internal waves, an under-explored source of turbulence events in the sedimentary record. *Earth-Science Reviews 111*(1-2), 56–81.

Pomar, L., M. Morsilli, P. Hallock, B. Bádenas, and D. Bourgault (2013). Reply to Shanmugam, G., comment on "Internal waves, an underexplored source of turbulence events in the sedimentary record" by Pomar et al. [earth-sci. rev., 111 (2012), 56-81]. *Earth-Science Reviews 116*, 206–210.

Porter-Smith, R., P. T. Harris, O. B. Andersen, R. Coleman, D. Greenslade, and C. J. Jenkins (2004). Classification of the Australian continental shelf based on predicted sediment threshold exceedance from tidal currents and swell waves. *Marine Geology 211*(1-2), 1–20.

Power, M. (2008). Miocene carbonate reef complexes in the Browse Basin and the implication for drilling operations. *APPEA Journal 48*, 115–132.

Rayson, M. D., G. N. Ivey, N. L. Jones, M. J. Meuleners, and G. W. Wake (2011). Internal tide dynamics in a topographically complex region: Browse Basin, Australian North West Shelf. *Journal of Geophysical Research 116*(C1).

Rayson, M. D., N. L. Jones, and G. N. Ivey (2012). Temporal variability of the standing internal tide in the Browse Basin, Western Australia. *Journal of Geophysical Research 117*(C6).

Reeder, D. B., B. B. Ma, and Y. J. Yang (2011). Very large subaqueous sand dunes on the upper continental slope in the South China Sea generated by episodic, shoaling deep-water internal solitary waves. *Marine Geology 279*(1-4), 12–18.

Reuning, L., S. Back, M. Hirsch, H. Schulz, P. Kukla, and J. Grötsch (2009). Seismic expression of sedimentary processes on a carbonate shelf and slope system, Browse Basin, Australia – Part I – non-tropical carbonates, Eocene to lower Miocene.

Romine, K. K. and J. Durrant (1996). *Carnarvon Cretaceous-Tertiary tie report*. Australian Geological Survey. Record 1996/36.

Romine, K. K., J. M. Durrant, D. L. Cathro, and G. Bernardel (1997). Petroleum play element predication for the Cretaceous-Tertiary basin phase, northern Carnarvon Basin. *APPEA Journal 37*, 315–339.

Rosleff-Soerensen, B., L. Reuning, S. Back, and P. Kukla (2012). Seismic geomorphology and growth architecture of a Miocene barrier reef, Browse Basin, NW-Australia. *Marine and Petroleum Geology 29*(1), 233–254.

Rosleff-Soerensen, B., L. Reuning, S. Back, and P. Kukla (2016). The response of a basin-scale Miocene barrier reef system to long-term, strong subsidence on a passive continental margin, Barcoo Sub-basin, Australian North West Shelf. *Basin Research 28*(1), 103–123.

Ryan, G. J., G. Bernardel, J. M. Kennard, A. T. Jones, G. A. Logan, and N. Rollet (2009). A precursor extensive Miocene reef system to the Rowley Shoals reefs, WA: evidence for structural control of reef growth or natural hydrocarbon seepage? *APPEA Journal 49*, 337–363.

Santala, M. (2011). Wheatstone reef wave transformation studies. In *Offshore Technology Conference*.

Saqab, M. M. and J. Bourget (2015a). Controls on the distribution and growth of isolated carbonate build-ups in the Timor Sea (NW Australia) during the Quaternary. *Marine and Petroleum Geology 62*, 123–143.

Saqab, M. M. and J. Bourget (2015b). Structural style in a young flexure-induced oblique extensional system, north-western Bonaparte Basin, Australia. *Journal of Structural Geology 77*, 239–259.

Schiller, A. (2011). Ocean circulation on the North Australian Shelf. *Continental Shelf Research 31*(10), 1087–1095.

Scotti, A. and J. Pineda (2004). Observation of very large and steep internal waves of elevation near the Massachusetts coast. *Geophysical Research Letters 31*(22).

Shanmugam, G. (2013a). Comment on "Internal waves, an under-explored source of turbulence events in the sedimentary record" by L. Pomar, M. Morsilli, P. Hallock, and B. Bádenas [earth-sci. rev., 111 (2012), 56–81]. *Earth-Science Reviews 116*, 195–205.

Shanmugam, G. (2013b). Modern internal waves and internal tides along oceanic pycnoclines: Challenges and implications for ancient deep-marine baroclinic sands. *American Association of Petroleum Geologists Bulletin 97*(5), 799–843.

Sharples, A. G. W. D., M. Huuse, C. Hollis, J. M. Totterdell, and P. D. Taylor (2014). Giant middle Eocene bryozoan reef mounds in the Great Australian Bight. *Geology 42*, 683–686.

Shepard, F. P., N. F. Marshall, P. A. McLoughlin, and G. G. Sullivan (1979). *Currents in Submarine Canyons and Other Seavalleys*. AAPG Studies in Geology No. 8. Tulsa, Oklahoma and U.S.A.: The American Association of Petroleum Geologists.

Simpson, J. E. (1982). Gravity currents in the laboratory, atmosphere, and ocean. *Annual Review of Fluid Mechanics 14*, 213–234.

Smith, R. L., A. Huyer, J. S. Godfrey, and J. A. Church (1991). The Leeuwin Current off Western Australia, 1986-1987. *Journal of Physical Oceanography 21*, 323–345.

Southard, J. B. and D. A. Cacchione (1972). Experiments on bottom sediment movement by breaking internal waves. In D. J. P. Swift, D. B. Duane, and O. H. Pilkey (Eds.), *Shelf sediment transport: process and pattern*, pp. 83–97. Stroudsburg, Pa. and U.S.A.: Dowden, Hutchinson and Ross.

Srinivasan, M. S. and D. K. Sinha (1998). Early Pliocene closing of the Indonesian Seaway: evidence from north-east Indian Ocean and tropical Pacific deep sea cores. *Journal of Asian Earth Sciences 16*, 29–44.

Stephenson, A. and S. Cadman (1994). Browse Basin, Northwest Australia: the evolution, palaeogeography and petroleum potential of a passive continental margin. *Palaeogeography, Palaeoclimatology, Palaeoecology 111*(3-4), 337–366.

Stow, D. A. V., F. J. Hernández-Molina, E. Llave, M. Sayago-Gil, V. Díaz del Rio, and A. Branson (2009). Bedform-velocity matrix: The estimation of bottom current velocity from bedform observations. *Geology 37*(4), 327–330.

Struckmeyer, H. I. M., J. E. Blevin, J. Sayers, J. M. Totterdell, K. Baxter, and D. L. Cathro (1998). Structural evolution of the Browse Basin, North West Shelf: New concepts from deep-seismic data. In P. G. Purcell and R. R. Purcell (Eds.), *The Sedimentary Basins of Western Australia 2*, Volume 2, pp. 345–366. Perth: Petroleum Exploration Society of Australia Symposium.

Swift, D. J. P. and J. A. Thorne (1991). Sedimentation on continental margins, I: A general model for shelf sedimentation. In D. J. P. Swift, G. F. Oertel, R. W. Tillman, and J. A. Thorne (Eds.), *Shelf Sand and Sandstone Bodies: Geometry, Facies and Sequence Stratigraphy*, pp. 3–31. Wiley.

Thomson, R. E. (1981). *Oceanography of the British Columbia Coast*. Can. Spec. Publ. Fish. Aquat. Sci. 56.

Thorpe, S. A. (1992). Thermal fronts caused by internal gravity waves reflecting from a slope. *Journal of Physical Oceanography 22*(1), 105–108.

Thorpe, S. A. (1999). The generation of alongslope currents by breaking internal waves. *Journal of Physical Oceanography 29*(1), 29–38.

Trincardi, F., G. Verdicchio, and S. Miserocchi (2007). Seafloor evidence for the interaction between cascading and along-slope bottom water masses. *Journal of Geophysical Research 112*(F3).

Turner, J. S. (1998). Stratification and circulation produced by heating and evaporation on a shelf. *Journal of Marine Research 56*(4), 885–904.

Van der Boon, C. M. (2011). *Numerical modelling of internal waves in the Browse Basin*. Msc thesis, TU Delft, Delft.

Van Gastel, P. (2010). *Internal wave dynamics on the Australian North West Shelf, PhD-thesis*. Ph. D. thesis, University of Western Australia.

Van Gastel, P., G. N. Ivey, M. J. Meuleners, J. P. Antenucci, and O. Fringer (2009). The variability of the large-amplitude internal wave field on the Australian North West Shelf. *Continental Shelf Research 29*(11-12), 1373–1383.

van Hinsbergen, D. J. J., L. V. de Groot, S. J. van Schaik, W. Spakman, P. K. Bijl, A. Sluijs, C. G. Langereis, and H. Brinkhuis (2015). A paleolatitude calculator for paleoclimate studies. *PLoS ONE 10*(6).

Veevers, J. J. and D. Cotterill (1978). Western margin of Australia: Evolution of a rifted arch system. *Geological Society of America Bulletin 89*(3), 337–355.

Venayagamoorthy, S. K. and O. B. Fringer (2007). On the formation and propagation of nonlinear internal boluses across a shelf break. *Journal of Fluid Mechanics 577*, 137–159.

Viana, A., J.-C. Faugères, and D. A. V. Stow (1998). Bottom-current-controlled sand deposits - a review of modern shallow- to deep-water environments. *Sedimentary Geology 115*(1-4), 53–80.

Vranes, K., A. L. Gordon, and A. Ffield (2002). The heat transport of the Indonesian Throughflow and implications for the Indian Ocean heat budget. *Deep Sea Research Part II: Topical Studies in Oceanography 49*(7-8), 1391–1410.

WCR Caswell-1 (1978). Well completion report.

Wilson, M. E. J. (2008). Global and regional influences on equatorial shallow-marine carbonates during the Cenozoic. *Palaeogeography, Palaeoclimatology, Palaeoecology 265*(3-4), 262–274.

Wilson, M. E. J. (2015). Oligo-Miocene variability in carbonate producers and platforms of the Coral Triangle biodiversity hotspot: habitat mosaics and marine biodiversity. *PALAIOS 30*(1), 150–168.

Wolanski, E. and E. Deleersnijder (1998). Island-generated internal waves at Scott Reef, Western Australia. *Continental Shelf Research 18*(13), 1649–1666.

Wynn, R. B., D. G. Masson, D. A. V. Stow, and P. P. E. Weaver (2000). Turbidity current sediment waves on the submarine slopes of the western Canary Islands. *Marine Geology 163*(1-4), 185–198.

Wynn, R. B., D. J. W. Piper, and M. J. R. Gee (2002). Generation and migration of coarse-grained sediment waves in turbidity current channels and channel-lobe transition zones. *Marine Geology 192*(1-3), 59–78.

Wynn, R. B. and D. A. V. Stow (2002). Classification and characterisation of deep-water sediment waves. *Marine Geology 192*(1-3), 7–22.

Wynn, R. B., P. P. Weaver, G. Ercilla, D. A. V. Stow, and D. G. Masson (2000). Sedimentary processes in the Selvage sediment-wave field, NE Atlantic: new insights into the formation of sediment waves by turbidity currents. *Sedimentology 47*(6), 1181–1197.

Zikanov, O. and D. N. Slinn (2001). Along-slope current generation by obliquely incident internal waves. *Journal of Fluid Mechanics 445*, 235–261.

Zinke, J., A. Rountrey, M. Feng, S.-P. Xie, D. Dissard, K. Rankenburg, J. M. Lough, and M. T. McCulloch (2014). Corals record long-term Leeuwin Current variability including Ningaloo Nino/NSina since 1795. *Nature communications 5*, 3607.

List of Figures

List of Tables

Acknowledgements

First of all I would like to thank my supervisors Stefan Back and Lars Reuning. Without their experience, advice, comments and time for discussions, writing this thesis would not have been possible.

I would also like to thank Conny Lutter for her tremendous help in acquiring the necessary scientific literature.

Many thanks also go to PGS and Geoscience Australia for providing the seismic reflection data surveys and to the Department of Mines and Petroleum (DMP) of Western Australia for providing well data and reports through the database WAPIMS.

IHS is gratefully acknowledged for providing the KINGDOM software under an Academic User License Agreement. Schlumberger is acknowledged for providing the software Petrel. The Gocad research group and Paradigm are gratefully acknowledged for providing the software Gocad.

Last but not least I would like to thank my family and friends for their support.